



16th DELTA User Meeting

&

Annual Report 2020

**Dortmund
30. November 2020**

Edited by C. Sternemann, R. Wagner,
D. Lützenkirchen-Hecht (2020)

Preface

Dear readers, dear colleagues,

this DELTA annual report is now the 16th, and it is actually the first going to be released without a user's meeting. Shortly after the restart of DELTA in January 2020, the COVID-19 pandemic struck Germany, and as a consequence many universities and research centers had to shut down all their activities in March, among those the TU Dortmund, the Universities of Siegen and Wuppertal, and others who substantially contribute to the operation of the DELTA storage ring and the closely related research activities. As a consequence, DELTA was not running for almost four months, and the restart in July almost fell into the start of summer shutdown foreseen for installation of the new 7-T superconducting wiggler (SCW). Anyhow, several research projects were successfully conducted in the first part of the year. The DELTA machine group took enormous efforts in order to install, cool down and condition the wiggler, since specialists from the Budker Institute of Nuclear Physics in Novosibirsk were not allowed to travel to Germany. The wiggler was subsequently successfully commissioned by the DELTA machine group at settings for user operation for SCW field values of 3.5 T and 4 T and tested up to a beam current of 130 mA. The second COVID-19 caused shutdown again terminated operation of DELTA in November, so that in total only 9 weeks of user operation and 7 machine-dedicated weeks were conducted in 2020 up to the end of November.

Having all those difficulties in mind, we have to deeply appreciate all the contributions included in this annual report, with in total 12 reports on instrumentation, 5 on soft X-ray spectroscopy, 18 on hard X-ray scattering and 4 on hard X-ray spectroscopy. These reports give a short compilation of all the activities carried out both at the different beamlines and the DELTA machine. During these periods, synchrotron radiation was provided reliably and the smooth operation of DELTA was ensured.

Despite the current difficulties, this annual report includes a broad spectrum of different case studies, of both fundamental and applied science and from various disciplines. We have to thank the involved technicians, engineers, scientists and researchers for their individual commitment in view of the problems caused by the pandemic. The manifold support by the local government and the diverse funding agencies is deeply appreciated, as well as we like to thank the universities and research institutions, in particular the TU Dortmund for their efforts. We gratefully acknowledge all these different contributions.

Contents:

| | |
|--|-----------|
| <u>Instrumentation</u> | 1 |
| Operation of the DELTA storage ring in 2020 S. Khan | 3 |
| Machine Learning applied to electron orbit control D. Schirmer | 5 |
| Machine Learning applied to automated tunes control D. Schirmer | 7 |
| Calculation of the transverse emittance of electron bunches at the photocathode of an RF gun cavity D. Krieg, S. Khan | 9 |
| Preparations for a precise measurement of the electron energy at DELTA C. Mai, A. Held, D. Kamberg, S. Khan | 11 |
| Progress on survey and alignment of the DELTA magnets and vacuum chambers G. Schmidt, B. Büsing, T. Dybiona, S. Khan, B. Sawadski, T. Schulte-Eickhoff | 13 |
| Installation and Conditioning of the 7-T Superconducting Wiggler at DELTA G. Schmidt, A. Althaus, B. Büsing, J. Friedl, G. Dahlmann, T. Dybiona, S. Khan, M. Paulus, H. P. Ruhl, B. Sawadski, D. Schirmer, T. Schulte-Eickhoff, C. Sternemann, M. Tolan | 15 |
| Impact of the new superconducting wiggler on the DELTA storage ring optics B. Büsing, S. Kötter, D. Schirmer | 17 |
| DELTA radiofrequency systems P. Hartmann, V. Kniss, A. Leinweber and the DELTA team | 19 |
| Commissioning of new orbit correction software at DELTA S. Köster | 21 |
| Observation of edge radiation at DELTA S. Khan, B. Büsing, A. Held, D. Krieg, C. Mai | 23 |
| Status of the beamline BL2 M. Kowalski, M. Paulus, E. Schneider, T. Witt, C. Sternemann, M. Tolan | 25 |

| | |
|---|----|
| <u>Soft X-ray spectroscopy</u> | 27 |
| Structural analysis of TiN nanoparticle reinforced CrN thin films W. Tillmann, D. Kokalj, D. Stangier, L. Hagen, L. Kesper, U. Berges, C. Westphal, C. Sternemann, M. Paulus | 29 |
| Examination of thin boron layers on a Si(100) surface - PureB by means of x-ray photoelectron spectroscopy A. Burkowitz, M. Schmitz, L. Kesper, U. Berges, S. Dreiner, D. Weier, L.K. Nanver, C. Westphal | 33 |
| Influence of sputtered carbon on the development of amorphous phases in CrAlCN DC/HiPIMS PVD Coatings W. Tillmann, D. Stangier, D. Kokalj, L. Hagen, P. Roese, K. Shamout, M. Schmitz, L. Kesper, A. Burkowitz, U. Berges, C. Westphal | 35 |
| Investigation of germanene phases on Ag(111) by means of XPS and XPD L. Kesper, M. Schmitz, J.A. Hochhaus, M.G.H. Schulte, U. Berges, C. Westphal | 39 |
| Chemical investigation a of graphene/cobalt/platinum multilayer system on silicon carbide P. Weinert, R. Hönig, L. Kesper, U. Berges, C. Westphal | 43 |
| <u>X-ray scattering</u> | 45 |
| Influence of Nitrogen content on the oxidation resistance of PECVD Ti-Si-B-C-N nanocomposite coatings A. Nienhaus, H. Paschke, C. Sternemann, M. Paulus | 47 |
| Influence of the deposition technology on the crystalline structure of TiAlN PVD coatings W. Tillmann, D. Stangier, D. Grisales, D. Kokalj, L. Hagen, J. Latarius, C. Sternemann, M. Paulus | 51 |
| X-ray diffraction study on cold sprayed Babbitt coatings W. Tillmann, M. Paulus, L. Hagen, D. Kokalj, D. Stangier, M. Abdulgader | 55 |
| Structural analysis of LBM 316L substrate PVD CrAlN coating composites W. Tillmann, L. Hagen, D. Stangier, D. Kokalj, N. F. Lopes Dias, D. Kensy | 59 |
| Temperature stability and decomposition of the hydrogen storage material NaBH ₄ R. Sakrowski, M. Szafarska, M. Elbers, G. Sourkouni, C. Sternemann, L. Wegewitz, M. Tolan, W. Maus-Friedrichs | 63 |
| Using reflectivity data to gain insights into microbiologically influenced corrosion of metal reducing bacteria (MRB) on stainless steel surfaces N. Wurzler, J.D. Schütter, R. Wagner, D. Lützenkirchen-Hecht, O. Ozcan | 65 |
| The surface structure of medical implants E. Schneider, M. Paulus, D. Stangier, K.-H. Bauer, M. Tolan | 69 |
| Ions at hydrophobic interfaces – the effect of pH E. Darscht, M. Paulus, S. Dogan, G. Surmeier, M. Moron, C. Sternemann, M. Tolan | 71 |
| Gas adsorption on hydrophobic surfaces near the critical point M. Moron, N. Thiering, J. Nase, M. Paulus, M. Tolan | 73 |
| Vapor phase deposition of metal-organic frameworks thin films A.J. Cruz, R. Ameloot, V. Rubio-Giminez, N. Wauteraerts | 75 |

| | |
|--|-----|
| Phase transition of cobalt valence tautomers tracked via X-ray powder diffraction at beamline BL9 F. Otte, K. Lehninger, C. Albers, R. Sakrowski, S. Jannuzzi, F. Alves Lima, C. Sternemann, M. Tolan | 79 |
| Studying the mechanics of metal-organic frameworks with high-pressure powder X-ray diffraction P. Kolodzeiski, L. Frenzel-Beyme, R. Pallach, J. Song, S. Henke | 81 |
| Microfluidic-SAXS study on kinetics and mechanism of Aescin induced DMPC vesicle decomposition into nano-disks T.J. Stank | 85 |
| Quaternary solid solutions of type $A^{\prime}xA^{\prime\prime}_{2-x}PdC_2$ ($A^{\prime}, A^{\prime\prime}$: Na-Cs) M. Krüger, U. Ruschewitz | 89 |
| Temperature dependent x-ray diffraction study of ionic liquids and their polymerized counterparts M. Elbers, C. Sternemann, P. Münzner, L. Friedrich, M. Paulus, J. Bolle, M. Tolan, C. Gainaru | 91 |
| The effect of osmolytes and polymers on the lamellar to cubic transition dynamics of monoolein in excess water G. Surmeier, M. Paulus, E. Schneider, M. Kowalski, M. Tolan, J. Nase | 93 |
| Analysis of linear alcohols from methanol to 1-nonanol J. Bolle, M. Požar, C. Sternemann, A. Perera | 97 |
| Charge carrier transport induced by x-ray radiation - role of the semiconductor (part 2) H. Makowska, O. Yildiz, W. Pisula, T. Marszalek | 99 |
| | |
| <u>Hard X-ray spectroscopy</u> | 101 |
| EXAFS investigations of nitrogen-treated niobium foils P. Rothweiler, R. Wagner, J. Klaes, B. Bornmann, D. Lützenkirchen-Hecht | 103 |
| EXAFS investigations of ZnO nanoparticles A. Šarić, F. Eckelt, M. Vrankić, D. Lützenkirchen-Hecht, R. Wagner | 105 |
| EXAFS investigations of electrodeposited Co-hydroxide layers L. Voss, R. Wagner, R. Frahm, D. Lützenkirchen-Hecht | 107 |
| EXAFS experiments on cobalt-doped barium aluminate M. Vrankić, A. Šarić, S. Bosnar, D. Lützenkirchen-Hecht, R. Wagner | 109 |
| | |
| <u>Notes</u> | 111 |

Instrumentation

Operation of the DELTA Storage Ring in 2020

S. Khan

Zentrum für Synchrotronstrahlung (DELTA), Technische Universität Dortmund

Normal operation with satisfactory uptime, beam lifetime, and stability of the DELTA storage ring came to an end in March 2020 with the advent of the COVID-19 pandemic. Restart of the machine in July went rather smoothly, considering the long downtime of almost 4 months. Another 8-week shutdown in September/October was caused by the installation of a new superconducting wiggler. Thereafter, operation was again suspended due to the increased number of COVID-19 cases, and at the time of writing (Nov 19), it is not clear when operation will be resumed. Until now, 9 weeks of user operation and 7 weeks of machine studies were undertaken in 2020.

During the pandemic-related shutdown, presence of personnel was kept to the minimum required to receive deliveries and to check for hazards in the DELTA building. An automated daily e-mail communicating vacuum pressure and other vital parameters proved to be very useful. Storage ring operation was resumed under strict observance of a hygiene concept which was approved in May by the university management.

Within the given restrictions, the machine group continued to pursue ongoing projects such as the installation of a new superconducting wiggler. Under normal circumstances, an expert team from the Budker Institute of Nuclear Physics (BINP) in Novosibirsk would perform the mechanical survey, lift the wiggler into the storage ring, test the cryostat and cool it down to 2.5 K, and finally bring the magnet up to 7 T. Since this visit was not possible, DELTA personnel had to performed these tasks in addition to warming up and removing the old wiggler and preparing the infrastructure for the new device (cables, cooling water, mechanical installations, computer control, liquid nitrogen/helium etc.). Close contact with the BINP experts via e-mail and online meetings were extremely useful and helped to solve a number of technical issues.

Another ongoing project is the installation of a CO₂ laser and a high-purity germanium detector to perform Compton backscattering for precision measurements of the beam energy which is the key to other beam dynamics parameters. An air-conditioned hutch was extended and newly arranged for this purpose. The laser system was delivered but pandemic-related travel restrictions presently preclude its commissioning by the manufacturer.

For the EEHG project, the undulator chambers were delivered, new dipole chambers were designed and procurement is ongoing. The design of chicane magnets and laser beamlines, as well as further beam dynamics simulations are underway. Other activities include work on radiofrequency components, survey and alignment of magnets and vacuum chambers, improved diagnostics and control of machine parameters (partly using artificial intelligence methods) as well as a large amount of less conspicuous work regarding electricity and electronics, mechanical construction, cooling water, cold gases, control system, etc.

As can be seen from the contributions to the Annual Report 2020, an impressive amount of work was performed by the users and the machine group of DELTA despite the restrictive situation.

Machine Learning Applied to Electron Orbit Control

D. Schirmer

Zentrum für Synchrotronstrahlung (DELTA), Technische Universität Dortmund

Machine learning (ML) methods were investigated for controlling and optimizing subsystems of the 1.5-GeV storage ring DELTA [1]. In first versions, ML techniques were successfully implemented to monitor and correct the electron orbit in separated transverse planes [2]. Recently, the method has been extended to the x,y -coupled storage ring. For this purpose, the neural network topology was significantly extended. Now, the neural network consists of 272 (108 input/108 hidden/56 output) neurons and about 18.000 connections (see Fig. 1 left).

Network training was performed with approximately 2600 data sets of real beam position and steerer strength measurements taking the x,y -orbit coupling into account (see Fig. 1 right). The network was trained with 80% of the data (blue curve) while a validation was performed with 20% "unseen" data sets (green curve). A "Scaled Conjugate Gradient" method was used for training the network [3].

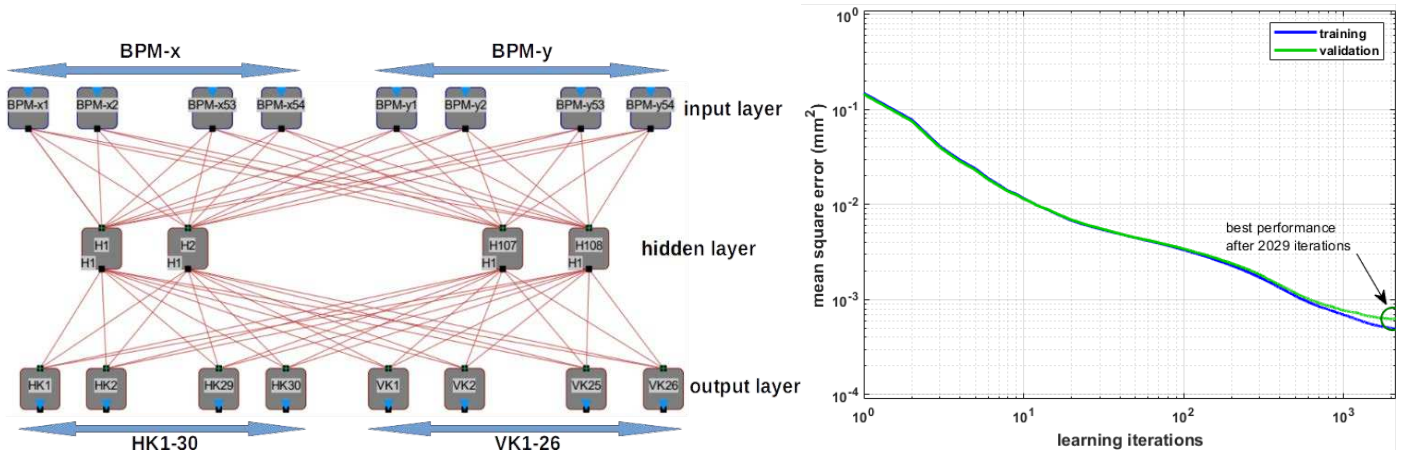


Figure 1: Left: Sketch of a fully connected feed-forward neural network to correct the particle trajectory at the DELTA storage ring. The input layer consists of measured beam positions at 54 BPMs (beam position monitors). It is linked to the output values for 56 corrector magnets (HK1-30, VK1-26) via a "hidden layer". The correction takes both transverse coordinates (x, y) and their coupling into account. Right: Training with experimental BPM data (blue) and validation of the neural network with an additional data set (green).

In addition, individual weight factors of the beam position measurement can be considered. Thus, orbit corrections can be applied to any desired reference orbit. The performance of the correction was compared to conventional methods [4,5]. It turned out that both algorithms are able to compensate a variety of orbit distortions (a-j) without beam losses (see Fig. 2). Even deviations which have not been trained during supervised learning (e-j) were compensated. In both cases, the residual weighted orbit error converged to comparable values (less than 3 mm) but the ML-based version requires on average significantly fewer correction steps.

Next, the migration of all ML algorithms to a dedicated deep-learning GPU-based server, which enables much faster adaptive training including "on the fly" data acquisition, is planned. Another goal is the integration of a storage ring simulation model [6]. This would enable offline-generation of additional extensive training data sets without time-consuming measurements during machine operation.

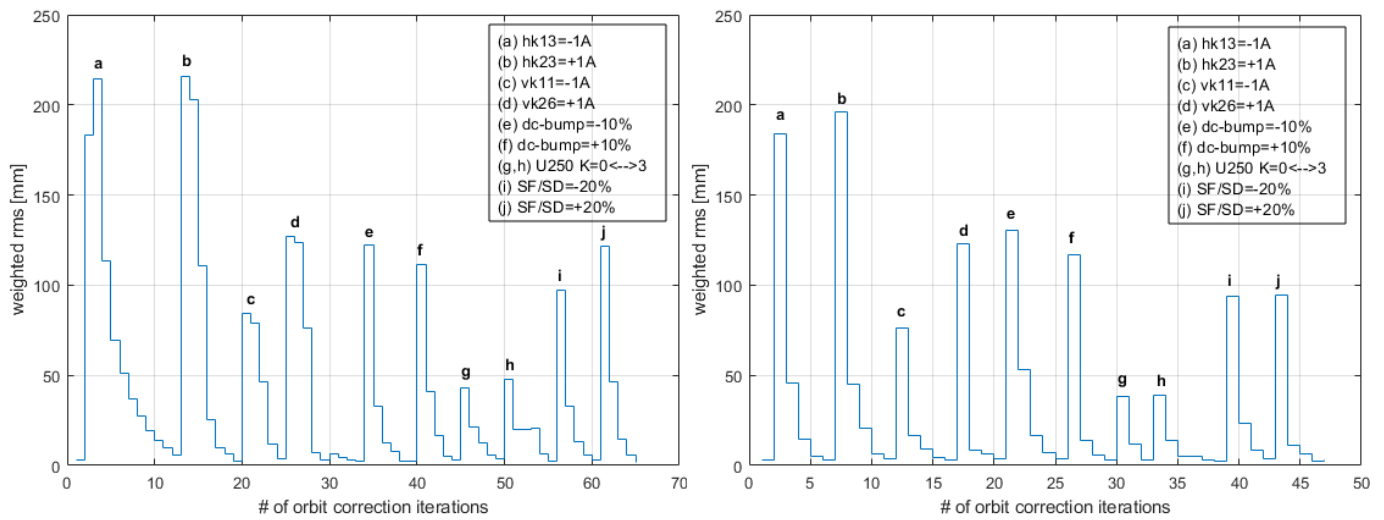


Figure 2: Stepwise correction of different scenarios of orbit deviations (a-j) with conventional orbit correction (left) and with a trained neural network (right). In the latter case, comparable final values of the mean measured deviation are achieved in significantly fewer correction steps.

References:

- [1] D. Schirmer, “Intelligent Controls for the Electron Storage Ring DELTA”, Proc. IPAC’18, Vancouver, Canada, p. 4855.
- [2] D. Schirmer, “Orbit Correction with Machine Learning Techniques at the Synchrotron Light Source DELTA”, Proc. of ICALEPCS 2019, New York, USA, p. 1426.
- [3] M. F. Moller, “A scaled conjugate gradient algorithm for fast supervised learning”, Neural Networks, Vol. 6, 1993, p. 525.
- [4] S. Kötter, A. Glassl, B. D. Isbarn, D. Rohde, M. Sommer, and T. Weis, “Evaluation of an Interior Point Method Specialized in Solving Constrained Convex Optimization Problems for Orbit Correction at the Electron Storage Ring at DELTA”, Proc. IPAC’18, Vancouver, Canada, p. 3507.
- [5] S. Kötter, B. Riemann, and T. Weis, “Status of the Development of a BE-Model-Based Program for Orbit Correction at the Electron Storage Ring DELTA”, Proc. IPAC’17, Copenhagen, Denmark, p. 673.
- [6] D. Schirmer and A. Althaus, “Integration of a Model Server into the Control System of the Synchrotron Light Source DELTA”, Proc. of ICALEPCS 2019, New York, USA, p. 1421.

Machine Learning Applied to Automated Tunes Control

D. Schirmer

Zentrum für Synchrotronstrahlung (DELTA), Technische Universität Dortmund

Machine learning (ML) algorithms are finding more and more use cases in the domain of accelerator controls. This also includes monitoring the storage ring betatron tunes. Due to thermal orbit movements and magnetic current-dependent field changes, the tunes may vary during machine operation. Therefore, automatic tunes correction is an important task, especially for the DELTA storage ring, as otherwise sudden beam losses can occur.

For this purpose, conventional, shallow (non-deep), feed-forward neural networks (NNs) were investigated (Fig. 1 left). The NNs were trained with experimental machine data as well as with simulated data based on a lattice model of the storage ring [1]. As an example, Fig. 1 (right) presents the corresponding results for 3000 tune calculations in two cases, the superconducting asymmetric wiggler (SAW) switched on and off. Thereby, the current set values of quadrupole families exclusively in the storage ring arcs were randomly changed and subsequently the associated tunes were determined (measured or simulated).

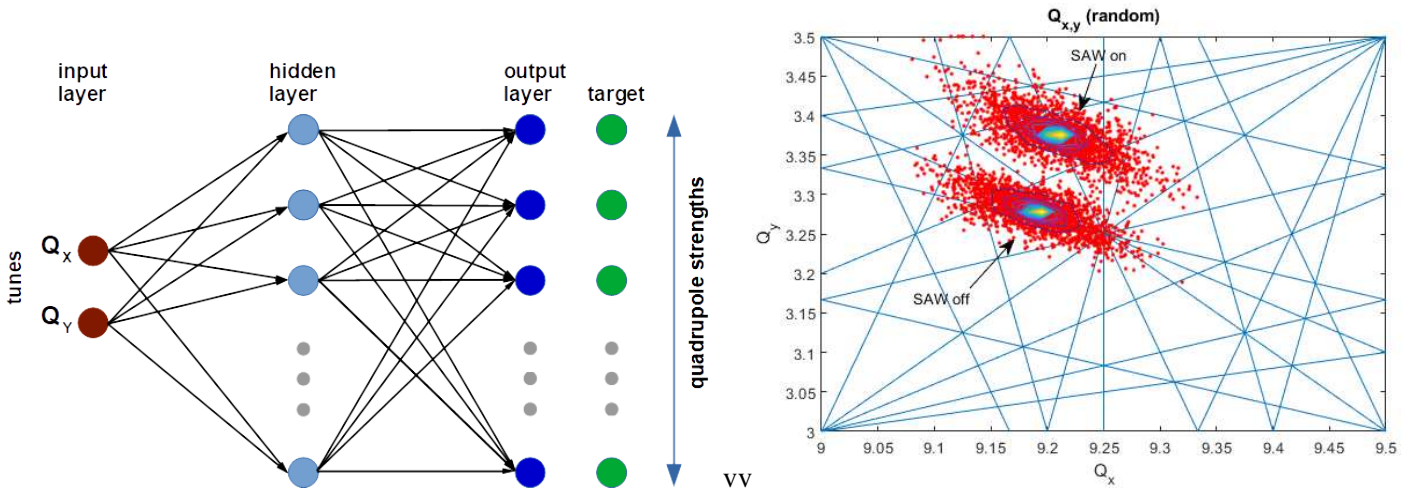


Figure 1: **Left:** Sketch of a fully connected 3-layered feed-forward neural network to be trained for automated tune control at the DELTA storage ring. **Right:** Distribution of 3000 random tunes generated by randomly varied quadrupole strength settings ($\pm 1\%$). The simulations were performed with the superconducting asymmetric wiggler (SAW) switched on and off. The tune is vertically shifted due to the edge focusing effect of the SAW.

With both data sources (experimental and simulation data), comparable tune correction accuracies were achieved, both, in real machine operation (Fig. 2, top and bottom right) and for the simulated storage ring model (Fig. 2, top and bottom left). In contrast to PID methods [2], the trained NNs are able to approach the desired target tunes in fewer steps. However, as long as the DELTA quadrupole power supplies lack the feature to drive synchronously, an iterative procedure for the NN-based tune control loop must necessarily be applied (see all subplots in Fig. 2). For a more detailed description see [3].

In principle, the same ML method can also be transferred to other accelerator optimization tasks. For example, data sets created by varying the sextupole strengths and measuring corresponding chromaticity changes can be used to train NNs which are subsequently applied to match desired storage ring chromaticities - an important parameter for stable storage ring operation with high electron beam currents. In the same manner, the method could also be used to adjust the coupling of the horizontal and vertical beta function and thereby the local transverse beam sizes. Here, for training data acquisition, one would have to vary the strengths of skew quadrupoles and determine the corresponding coupling change [4].

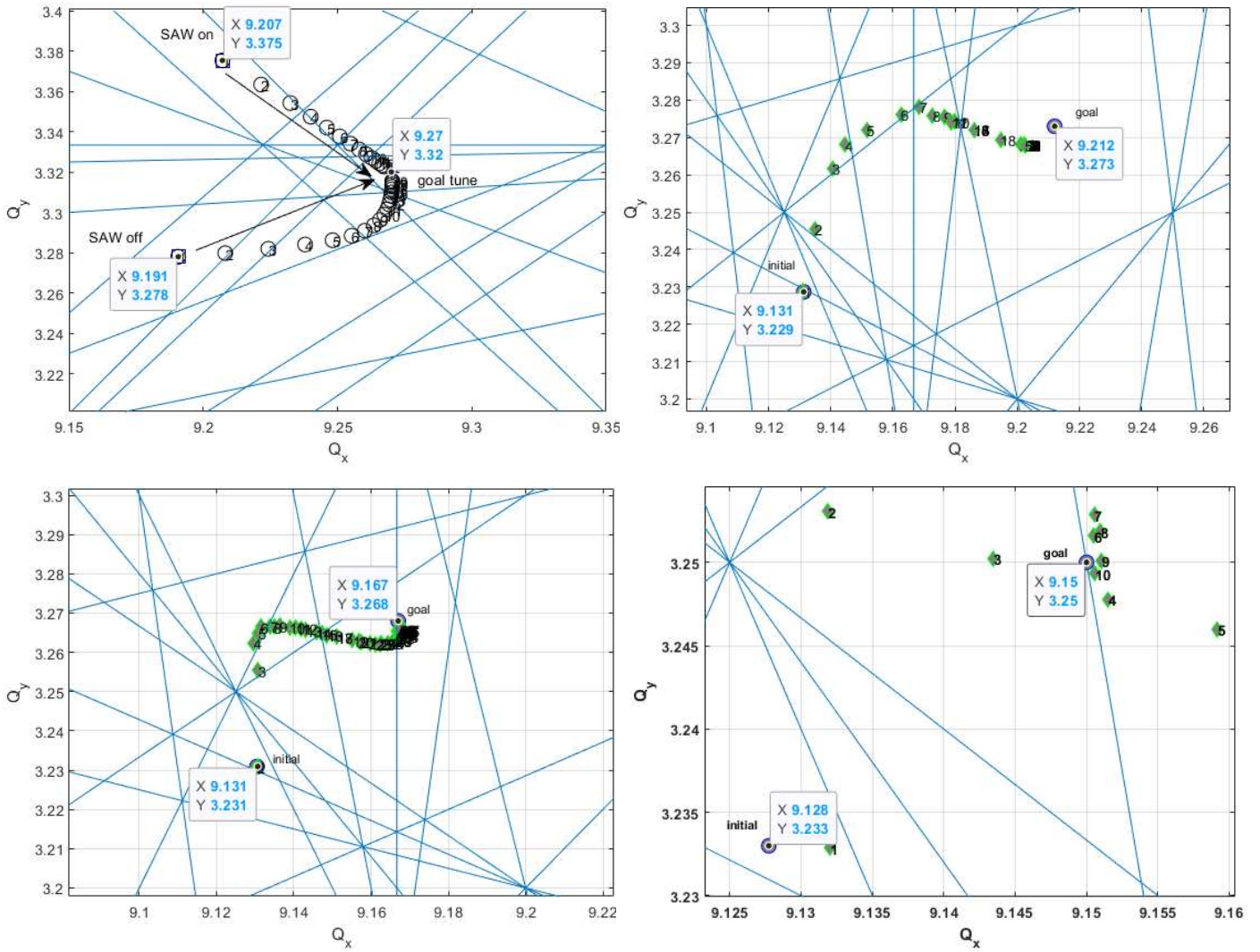


Figure 2: **Left top:** Example for the verification of a NN which was trained by real machine data and applied to the simulated accelerator model with SAW switched on and off. **Right top:** Example for the validation of a NN trained by simulation data and applied to the real machine with SAW switched on. **Left bottom:** Example application of a NN trained with real machine data and applied to the storage ring model. **Right bottom:** Use case of a NN trained by measured machine data and applied to real machine operation. In all examples, the NNs can approach the desired goal tunes in iterative steps [3].

References:

- [1] D. Schirmer and A. Althaus, “Integration of a Model Server into the Control System of the Synchrotron Light Source DELTA”, Proc. of ICALEPCS 2019, New York, USA, p. 1421.
- [2] P. Hartmann, et al., “Kicker Based tune Measurement for DELTA”, in Proc. DIPAC’07, Venice, Italy, p. 277.
- [3] D. Schirmer, “Machine Learning Applied to Automated Tunes Control at the 1.5 GeV Synchrotron Light Source DELTA”, DELTA Internal Report (2020), to be published.
- [4] S. C. Leemann, “Applying Machine Learning to Stabilize the Source Size in the ALS Storage Ring”, presented at IPAC’20, Caen, France (2020).

Calculation of the Transverse Emittance of Electron Bunches at the Photocathode of an RF Gun Cavity

D. Krieg, S. Khan

Zentrum für Synchrotronstrahlung (DELTA), Technische Universität Dortmund

Introduction

The choice of a radiofrequency (RF) gun cavity for ultrafast electron diffraction is presently investigated. The transverse beam emittance is a measure of the beam quality and thus decisive for the quality of a diffraction image. As a first step, the emittance at the emission of the electrons from the photocathode at time $t = 0$ is determined.

Intrinsic emittance ϵ_{int}

The intrinsic or thermal emittance [1, 2]

$$\epsilon_{\text{int}} = a \cdot \sqrt{\frac{\hbar\omega - \phi_0 + \sqrt{e^3 E_{\text{acc}} / (4\pi\epsilon_0)}}{3m_e c^2}} \quad (1)$$

is caused by the transverse size a of the electron bunch at the cathode (and thus the transverse laser size) and the initial momentum of the electrons, induced by the energy difference of the photon energy $\hbar\omega$ and the cathode material work function ϕ_0 , reduced by the electric field at the time of emission $E_{\text{acc}} = E_{\text{cath}} \sin \varphi_0$ with the maximum electric field E_{cath} and the RF gun phase φ_0 . Fig. 1 shows ϵ_{int} as a function of φ_0 and E_{cath} , assuming a copper cathode with a work function of $\phi_0 = 4.31$ eV [3] and a laser wavelength of 266 nm (3rd harmonic of a Ti:Sapphire laser).

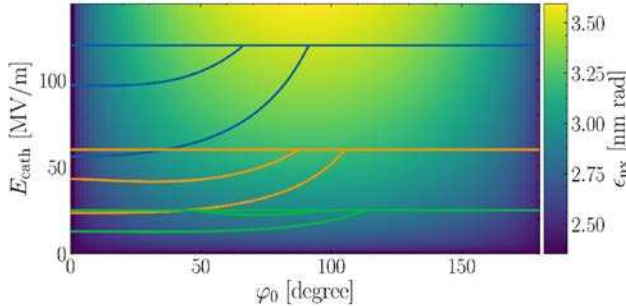


Figure 1: Intrinsic emittance color-coded as a function of φ_0 and E_{cath} . For three cavity designs, the $(\varphi_0, E_{\text{cath}})$ -combinations resulting in an electron energy between 3 and 5 MeV are marked by colored lines.

Space-charge-induced emittance ϵ_{SPC}

The space-charge-induced emittance ϵ_{SPC} mainly has an effect at the cathode since space charge forces are strongly suppressed with increasing Lorentz factor γ and can be calculated via [1, 2]

$$\epsilon_{\text{SPC}} = Q \underbrace{\frac{m_e c^3 \pi}{2I_0 e}}_{\text{constant term } C} \underbrace{\frac{1}{E_{\text{cath}} \sin \varphi_0}}_{\text{gun term } G} \underbrace{\frac{\mu(A)}{L}}_{\text{bunch term } B} \quad (2)$$

with the electron bunch charge Q , the bunch aspect ratio $A = a/L$ (a being the transverse and L the longitudinal size), the so-called space charge factor μ , and other constants summarized in the term C . Fig. 2 shows the reciprocal gun term G^{-1} as a function of φ_0 and E_{cath} , the bunch term B as a function of a and L for a gaussian and cylindrically shaped electron bunch.

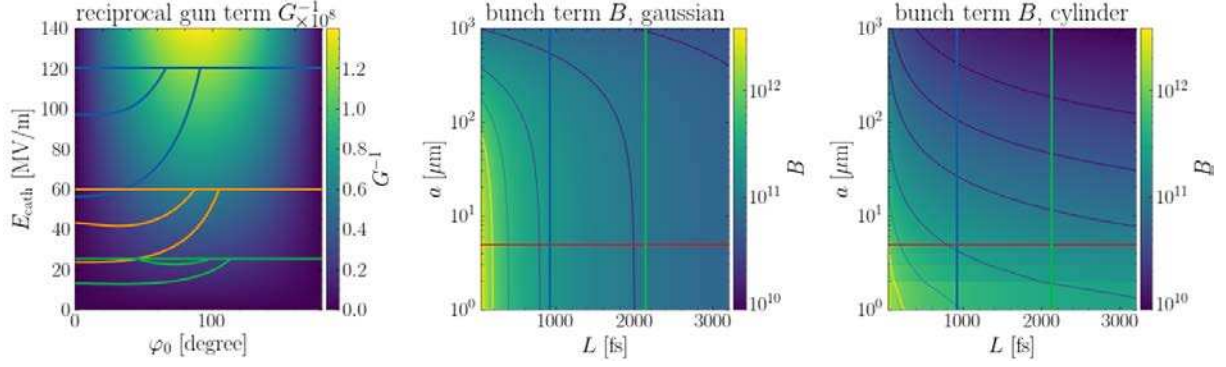


Figure 2: Reciprocal gun term G^{-1} as a function of φ_0 and E_{cath} (left) bunch shape term B as a function of a and L for a gaussian and a cylindrical electron bunch (center and right).

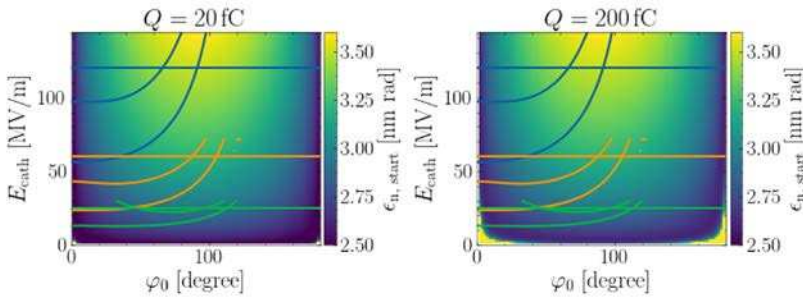


Figure 3: Transverse emittance at the cathode calculated as a function of initial gun phase and electric field at the cathode for two bunch charges, 20 fC and 200 fC. The emittance was minimized by variation of the transverse and longitudinal electron bunch size.

Transverse emittance at cathode

As can be seen in Eq. (2) and Fig. 2, the bunch shape factor B decreases with increasing a . On the other hand, the intrinsic emittance scales as $\epsilon_{\text{int}} \propto a$. Figure 3 shows the transverse

emittance at the cathode, calculated as $\epsilon = \sqrt{\epsilon_{\text{int}}^2 + \epsilon_{\text{SPC}}^2}$ [2], as a function of φ_0 and E_{cath} . The emittance is minimized for each φ_0 and E_{cath} by variation of a and L with $5 \mu\text{m} \leq a \leq 1 \text{mm}$ and $40 \text{fs} \leq c \cdot L \leq 3000 \text{fs}$, assuming a cylindrical electron bunch. The variation of the electron bunch sizes at the cathode is acceptable because subsequent transverse and longitudinal compression is done using a solenoid and a bunching cavity, respectively. As can be seen, the transverse emittance at the cathode is dominated by the intrinsic emittance. For the bunch changes used here, it is minimal for the smallest transverse size a and the largest bunch length L .

Outlook

The transverse emittance at the cathode was determined as a first step. The final emittance results from adding RF-induced effects and transverse focusing from solenoids.

References

- [1] T. Rao and D. H. Dowell, "An Engineering Guide to Photoinjectors", arXiv: 1403.7539 (2014).
- [2] D. H. Dowell, „Sources of Emittance in RF Photocathode Injectors: Intrinsic emittance, space charge forces due to non-uniformities, RF and solenoid effects”, arXiv: 1610.01242 (2016).
- [3] D. Palmer. "A Review of Metallic Photocathode Research", SLAC-TN-05-080 (2005).

Preparations for a Precise Measurement of the Electron Energy at DELTA

C. Mai, A. Held, D. Kamberg, S. Khan

Zentrum für Synchrotronstrahlung (DELTA), Technische Universität Dortmund

Overview

The electron energy is one of the fundamental parameters of a storage ring. However, a determination of the energy by just measuring the magnetic field of a bending magnets and the beam curvature is not very precise. The typical accuracy of hall-probe based magnetic-field measurements is on the order of 10^{-3} [1]. Two methods with a substantially improved accuracy are gamma spectroscopy of Compton-backscattered photons [2,3] and resonant depolarization of the electron beam [4]. Resonant depolarization measurements can only be repeated after a polarization time of several minutes. Currently, a setup to measure the electron energy by a scattering experiment is designed and implemented at DELTA.

Compton-Backscattering of Laser Photons

The scattering of a photon and a relativistic electron is described by the Thomson cross-section [4]. A head-on collision leads to a maximum energy

$$E' = \frac{4E\gamma^2}{\left(1 + \frac{4\gamma E}{m_e c^2}\right)}$$

of the scattered photon with initial photon energy E . Here, γ is the Lorentz factor, m_e is the electron mass and c is the speed of light. The scattered photons primarily move collinear with the electron beam. The emission of continuous-wave CO₂ lasers can be stabilized to provide a nearly perfect monochromatic beam. Laser emission from only few laser lines is possible, and hence, the initial photon energy is known with high precision. Given that the electron energy is in the GeV range, a 10.6- μm photon from a CO₂ laser with a photon energy of 117 meV is energy shifted to the MeV range. This energy can be measured with a high-purity germanium (HPGe) detector to deduce the Lorentz factor and the electron energy.

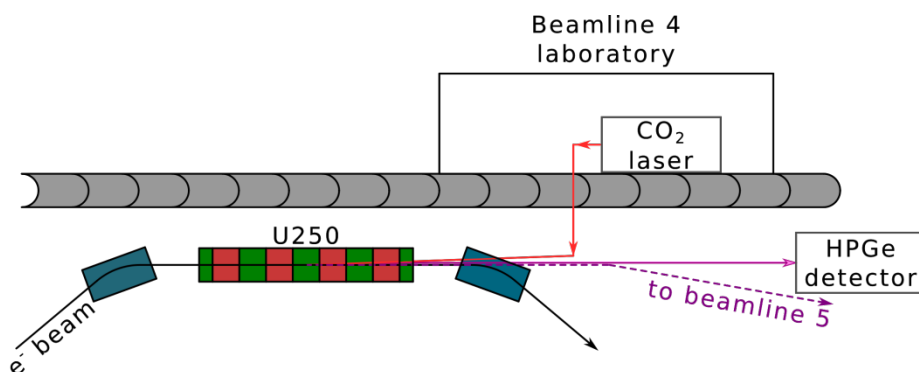


Figure 1: Sketch of the setup for the Compton backscattering experiment (not to scale). The beamline 4 laboratory was extended to house a new CO₂ laser. The interaction region of electrons and laser photons is the straight section of the undulator U250 and the scattered photons primarily follow the electron direction. A new high-purity germanium (HPGe) detector is used to measure the energy of the scattered photons.

Setup at DELTA

A sketch of the setup which will be implemented at DELTA is shown in Fig. 1. In order to provide an air-conditioned environment for the operation of a CO₂ laser, the hutch of beamline 4 was extended. It now houses one optical table for diagnostics of VUV radiation [5] and a second optical table to hold the new CO₂ laser. Currently, an HPGe detector is commissioned for the detection of gamma radiation from electron-photon scattering. A mechanical survey was carried out to determine the optimum detector position. The CO₂ laser has been delivered and will be commissioned soon. It has an average power of 50 W and uses a grating controlled by a feedback loop to stabilize the wavelength.

Outlook

A precise energy measurement allows to determine the momentum compaction factor of the storage ring which is the key to other beam dynamics parameters. A study of the energy spread of the electron beam is possible if systematic errors from alignment, detector collimation and the geometry of the setup are understood. In conjunction with the short-pulse facility of DELTA, where an ultrashort laser pulse is used to modulate the electron energy, the scattering experiment possibly provides an independent detection mechanism for the energy modulation.

References

- [1] A.W. Chao, "Handbook of Accelerator Physics", World Scientific, 1999.
- [2] G. Ulm, "Radiometry with Synchrotron Radiation", *Metrologia* 40, S101 (2003).
- [3] R. Klein, et al., "Measurement of the BESSY II electron beam energy by Compton-backscattering of laser photons", *Nucl. Instrum. Methods A* 486, p. 545 (2002).
- [4] M. Peskin, D. Schroeder, *An Introduction To Quantum Field Theory*, CRC Press, 1995.
- [5] A. Meyer auf der Heide, *The DELTA Short-Pulse Source: Upgrade Plans from CHG to EEHG*, Proc. of the IPAC 2019, Melbourne, Australia, p. 1457.

Progress on Survey and Alignment of the DELTA Magnets and Vacuum Chambers

G. Schmidt, B. Büsing, T. Dybiona, S. Khan, B. Sawadski, T. Schulte-Eickhoff

Zentrum für Synchrotronstrahlung (DELTA), Technische Universität Dortmund

Overview

The performance of a storage ring regarding beam lifetime, stability and injection efficiency depends on the alignment of all components. If the stored beam passes through the center of the quadrupole and sextupole magnets, nonlinearities are minimized, the model of the magnetic optics is more accurate and the machine is easier to operate. During the last three years, all quadrupole magnets and vacuum chambers of the storage ring were realigned horizontally [1, 2]. The storage ring has now stabilized on a good beam lifetime, high orbit stability, reproducibility of magnet settings, improved injection efficiency and on a low radiation level in the DELTA hall. The alignment of dipole magnets has started beginning of this year. Most recently, the superconducting asymmetric wiggler was aligned to its target position.

Alignment of dipole magnets

The DELTA dipole magnets have a large radial displacement and some longitudinal variations in their position. Kicks due to a longitudinal displacement of the dipoles must be compensated by nearby steerers. To reduce the steerer strengths, the longitudinal dipole position must be adjusted.

The radial displacement is less critical for the orbit but due to edge focusing, there is an influence on the beta beat of the storage ring. The radial adjustment of the dipole was possible without visible effect on the closed orbit of the electron beam.

Longitudinal position offsets of the dipoles is shown in Fig. 1. The alignment was performed in several steps with electron beam operation in between. This allowed to adapt the steerer strengths in DELTA to the new dipole positions and to keep the electron beam operation possible. The dipoles in the vicinity of the RF cavities (around $s = 0$ m) are not yet realigned.

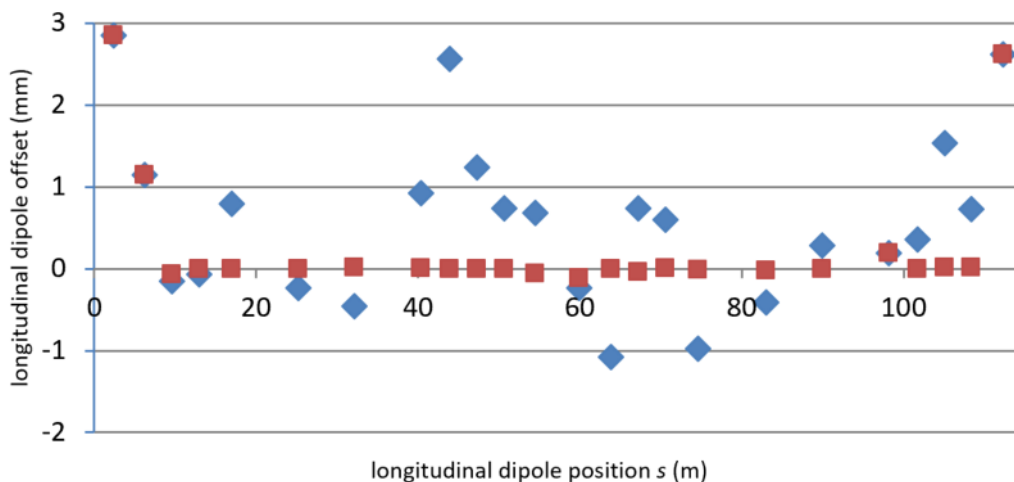


Figure 1: Longitudinal displacement of dipole magnets before (blue) and after (red) adjustment. The measurement accuracy is better than ± 0.3 mm.

Alignment of the superconducting asymmetric wiggler

In preparation of the installation of the new superconducting wiggler, the old superconducting asymmetric wiggler (SAW) was realigned towards the target position. No problems regarding the operation of the storage ring and the wiggler beamlines occurred.

Outlook

The final goal of the alignment program to align the storage ring magnets will be reached soon. The insertion devices are adjusted close to their target positions. Additional effort will be needed to survey and align the vacuum chambers. Due to production deviations of the vacuum chambers, their alignment will be difficult and individual decisions must be made how to place the chambers inside the aligned magnet structure.

As a future project, further improvement of the injection efficiency and thus reduced injection time can be expected from realigning the magnets of the booster synchrotron.

References

- [1] G. Schmidt et al., *Survey and Alignment of the DELTA Magnets and Vacuum Chamber*, DELTA Annual Report 2018.
- [2] G. Schmidt et al., *Survey and Alignment of the DELTA Magnets and Vacuum Chamber*, DELTA Annual Report 2019.

Installation and Conditioning of the 7-T Superconducting Wiggler at DELTA

G. Schmidt, A. Althaus, B. Büsing, J. Friedl, G. Dahlmann, T. Dybiona, S. Khan, M. Paulus,
H. P. Ruhl, B. Sawadski, D. Schirmer, T. Schulte-Eickhoff, C. Sternemann, M. Tolan

Zentrum für Synchrotronstrahlung (DELTA), Technische Universität Dortmund

Overview

A 7-T Superconducting Wiggler (SCW) was built and delivered to DELTA by the Budker Institute of Nuclear Physics (BINP) [1] in Novosibirsk, Russia. The SCW replaces the old Superconducting Asymmetric Wiggler (SAW) allowing for higher photon energy and intensity. Since procurement and manufacturing of a new and optimized outlet chamber takes more time, a concept was developed to install the SCW with special vacuum fittings which adapt the existing vacuum chamber in shape and length to the new SCW parameters.

Since the intended SCW installation and commissioning by a team from BINP was unfeasible due to the prevailing COVID-19 pandemic, this task was performed by DELTA personnel with remote instructions from BINP.

Due to the high heat load of the SCW compared to the old SAW, the beam current or magnetic field of the SCW must be limited to not overheat the existing outlet vacuum chamber and beam stoppers of the beamlines 8, 9, and 10. A newly designed outlet chamber, which is being manufactured, together with improvements of the beamlines will allow to reach the design values of 7 T at 130 mA beam current end of 2021.

Preparation of the installation

In preparatory work, the old SAW was realigned towards the SCW's target position. The previous horizontal misalignment of the SAW was of the order of 3 mm. After alignment, beam operation was possible without problems and the SAW beamlines were able to operate as before. A survey of the adjacent beam position monitors allowed to keep the electron beam position constant after the installation of the SCW.

Installation of the SCW

An installation period of 8 weeks in September and October 2020 was required to remove the old SAW with its infrastructure and to install all components of the new SCW into the storage ring of DELTA. The period included the warming-up of the old wiggler (2 weeks) before opening the vacuum system, the cool down time and field conditioning of the new SCW.

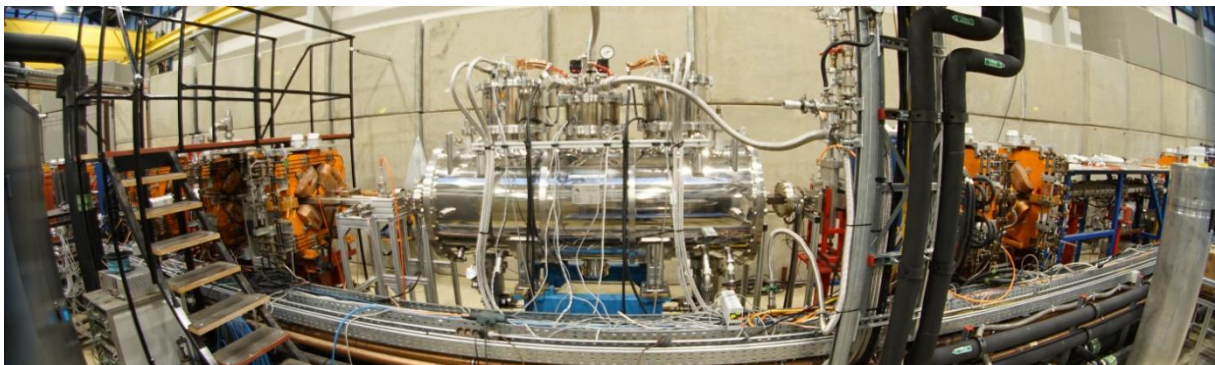


Figure 1: New SCW installed into the DELTA storage ring.

All vacuum components were baked out before installation in the storage ring. All work on vacuum chambers was done under a constant flow of dry nitrogen to avoid water contamination of the vacuum system. The installation area of the vacuum components was kept under a tent with constant nitrogen flow. This enabled a very short recovery time of the vacuum pressure with electron beam.

Cool-down procedure and field conditioning

Cooling down to 2.5 K was performed with only minor problems. Since a valve of the helium transfer line was not closing properly, frozen air blocked part of the cryostat, but increasing the temperature to 100 K removed the nitrogen and oxygen ice. The second attempt to cool down to 2.5 K was then successful and the SCW was ready for field conditioning. When the wiggler was delivered and assembled at DELTA in 2018, it had been preconditioned to 7.2 T after 7 quenches [2]. After installation in the ring, the design field of 7 T was reached without further quench.

Beam operation with the new SCW

During beam operation, the magnetic field of the SCW was increased in steps of 0.5 T at beam currents around 10 mA. Vertical and horizontal orbit shifts as well as a vertical tune shift were observed. Both were expected and smoothly compensated by the orbit correction system. The SCW-induced tune shift was corrected with the quadrupoles around the bending magnets in the east and west sectors of DELTA.

The orbit shift could be compensated up to an SCW field of 5.5 T. Above this value, the wiggler-induced vertical kick could not be balanced by the standard steerers. A dedicated vertical steerer has been designed and will be built during November 2020 to compensate the kick directly downstream of the SCW.

Settings for user operation for SCW field values of 3.5 T and 4 T were established and tested up to a beam current of 130 mA. The injection efficiency with these settings remained on the same level as with the old SAW. With small beam current and without orbit correction, the SCW could be operated at the design field of 7 T. Injection was possible but with reduced efficiency. Operation with higher beam current can be expected after the installation of the dedicated vertical steerer.

Outlook

The new outlet vacuum chamber with increased vacuum pumping speed, optimized cooling and enlarged vertical aperture together with dedicated vertical steerers and improved cooling of critical beamline components will allow storage ring operation up to the design values of 130 mA beam current and 7 T field of the SCW. The delivery of the outlet chamber is foreseen for the end of 2021.

References

[1] <http://www.inp.nsk.su/>.

[2] Vitaliy Shkaruba, Nikolay Mezentsev, "Site Acceptance Test of Superconducting Wiggler for DELTA in period July 23 - August 16 2018", private communication.

Impact of the New Superconducting Wiggler on the DELTA Storage Ring Optics

B. Büsing, S. Kötter, D. Schirmer

Center for Synchrotron Radiation (DELTA), TU Dortmund, 44227 Dortmund, Germany

A preliminary analysis to evaluate the impact of the new superconducting wiggler (SCW) [1] on the optics of the storage ring has been made. For this purpose, the results of an optics simulation were compared to measured beta function values and tune shifts for different SCW field strengths.

The optics simulation is based on the DELTA model file del008 updated with a SCW model and measurement-based quadrupole strengths. The latter were determined from quadrupole currents via the conversion tool i2k [2] and correspond to the quadrupole strengths used during the beta-function and tune measurements. The simulation is executed using the code elegant [3].

The beta function was measured in two ways. Firstly, two orbit responses were recorded for SCW magnetic flux densities of 0 T and 4 T and then decomposed into beta function values at all beam position monitors by fitting the bilinear-exponential model with dispersion (BE+d model) [4]. Secondly, the average beta function in most quadrupoles was determined from the tune shifts following applications of gradient errors at each quadrupole for the same SCW settings. Figure 1 displays a comparison of the vertical beta function values from the optics model and the results of both measurement methods. Overall, the optics model corresponds well to the measurement results if the SCW is turned off. For a SCW setting of 4 T, the correspondence decreases in the region of s from 20 m to 40 m and directly before and after the SCW at around 75 m and 85 m.

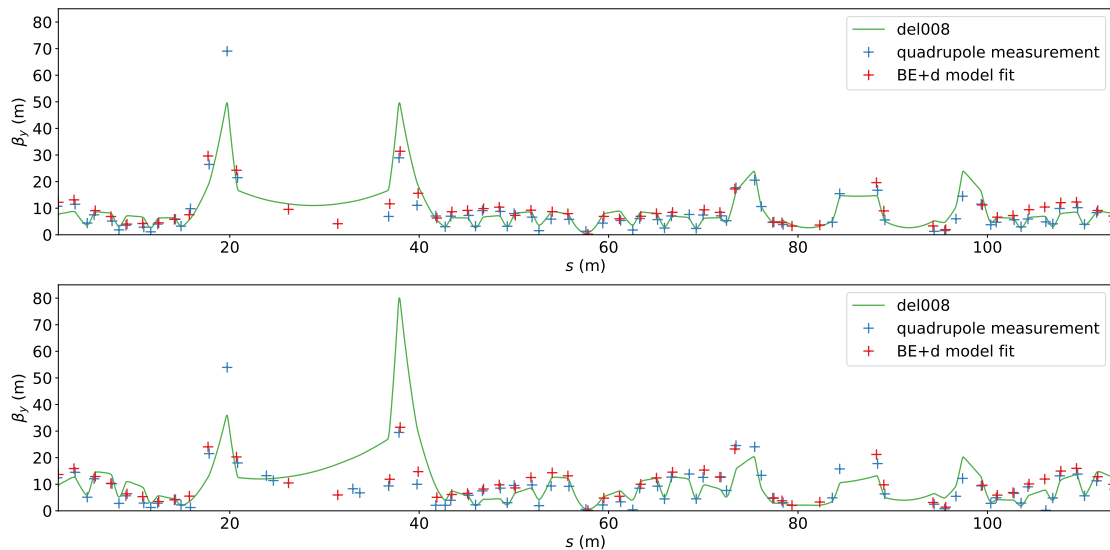


Figure 1: Vertical beta function for SCW settings of 0 T (top) and 4 T (bottom).

Vertical tunes were measured using the kicker-based tune measurement of the storage ring for SCW settings ranging from 0 T to 3.5 T [5] and compared to the optics simulation and a theoretical model [6]. The tune shift for each setting is calculated by subtracting

the tune for 0 T. The results are displayed in Figure 2. Simulation and theoretical model correspond well. The measurements diverge from simulation and theoretical model for magnetic flux densities larger than 2 T.

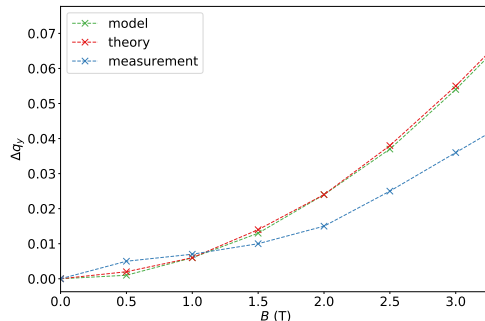


Figure 2: SCW-induced vertical tune shift.

In summary, first attempts at understanding the impact of the newly installed SCW on vertical focusing were made by comparing beta-function and tune measurements to an optics model. The beta-function results of the optics simulation in the arcs of the storage ring correspond well to the measurements. The simulated tune shift matches measurements below SCW settings of 2 T.

References

- [1] N. A. Mezentsev, A. Bragin, S. Khan, *et al.*, “Superconducting 7 Tesla wiggler for delta synchrotron radiation source”, in *Proc. RUPAC’18*, paper THPSC05, Protvino, Russia, October 2018.
- [2] M. Grewe, “Orbitkorrektur am Speicherring DELTA”, dissertation, TU Dortmund University, January 2005.
- [3] M. Borland, “Elegant: A flexible SDDS-compliant code for accelerator simulation”, in *Proc. IPAC’00*, paper LS-287, Darmstadt, Germany, October 2000.
- [4] B. Riemann, “The bilinear-exponential closed-orbit model and its application to storage ring beam diagnostics”, dissertation, TU Dortmund University, April 2016.
- [5] P. Hartmann, J. Fürsch, R. Wagner, T. Weis, and K. Wille, “Kicker based tune measurement for DELTA”, in *Proc. DIPAC’07*, paper WEPB21, Venice, Italy, May 2007.
- [6] N. Markus, R. P. Walker, and M. Poole, “SRS behaviour with a superconducting 5-Tesla wiggler insertion”, *Transactions on Nuclear Science*, vol. 30, pp. 3127–3129, Sep. 1983.

DELTA Radiofrequency Systems

P. Hartmann, V. Kniss, A. Leinweber and the DELTA team

Zentrum für Synchrotronstrahlung (DELTA), Technische Universität Dortmund

The klystron of the linear accelerator is in operation since many years. As a preventive measure, it will be replaced in the Christmas shutdown end of 2020. The radiofrequency (RF) system of the booster synchrotron comprising a solid-state amplifier has given no trouble in 2020.

As in the two years before, the RF group had its focus on the RF system of the storage ring. After the digital low-level RF system (DLLRF) was repaired by the manufacturer in November 2019, no more issues were encountered regarding this device. Two-cavity operation has become the standard operational mode of the storage ring. Since the DLLRF is on the critical path for the operation of the storage ring, a spare had been ordered which was delivered in August.

A second EU-type resonator powered by a solid-state amplifier had been installed in 2019. During the rare accelerator study weeks in 2020, several measurements were made in order to characterize the new RF system.

The accelerating voltage inside the cavity is measured by an ADC inside the DLLRF from a signal of the cavity probe. The calibration of this measurement is important. It has thus been verified using a beam-based method: The cavity voltage U_C , the loss voltage per revolution U_{rev} and the synchrotron frequency f_S are related by the nonlinear dependence

$$U_C = \sqrt{\left(\frac{2\pi E}{f_{rev}^2 \alpha h e}\right)^2 f_S^4 + U_{rev}^2} .$$

A factor $k = 2.076 \text{ kV}^2/\text{Hz}^4$ is calculated from the known beam energy E and the momentum compaction factor α . A fit to the measured synchrotron frequency at different cavity voltages (see Fig. 1) determines k to be $2.086 \pm 0.011 \text{ kV}^2/\text{Hz}^4$ with the superconducting asymmetric wiggler (SAW) switched on and $2.086 \pm 0.006 \text{ kV}^2/\text{Hz}^4$ with SAW off (energy loss from dipole magnets only).

The offset at $f_S = 0$ depends on the beam current I . Extrapolated to $I = 0$, the resulting loss voltage is $U_{rev} = 150 \text{ kV}$ with and 128 kV without SAW. Measurements (see Fig. 2) yield $U_{rev} = (149.4 \pm 2.3) \text{ kV}$ and $(128.7 \pm 0.2) \text{ kV}$, respectively, in excellent agreement with the synchrotron frequency measurements.

Another very instructive measurement is the comparison of the phase noise on the outputs of the power amplifiers. Phase noise is transferred directly to the electron beam in the storage ring. The green curve in Fig. 3 shows the input to the klystron as well as to the solid-state amplifier (SSA) while the blue and red curves show their output. At certain frequencies, the phase-noise levels generated by the klystron turn out to be several orders of magnitude higher than those generated by the SSA. As consequence, it is intended to replace the klystron by an SSA in the long run.

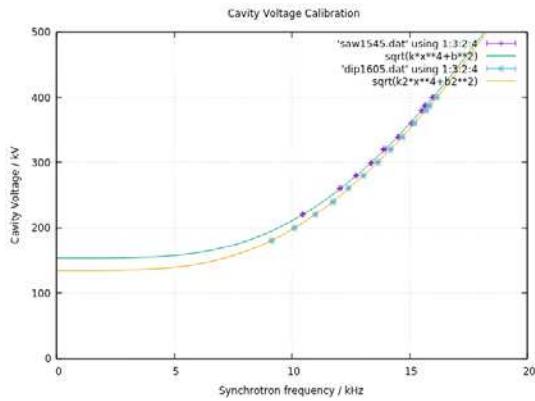


Figure 2: Cavity voltage vs. synchrotron frequency.

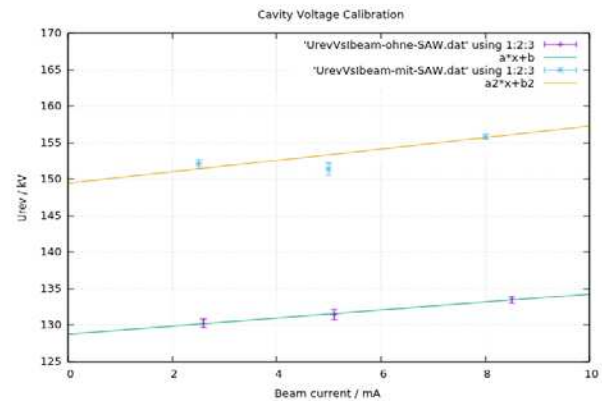


Figure 3: Single-turn loss vs. beam current.

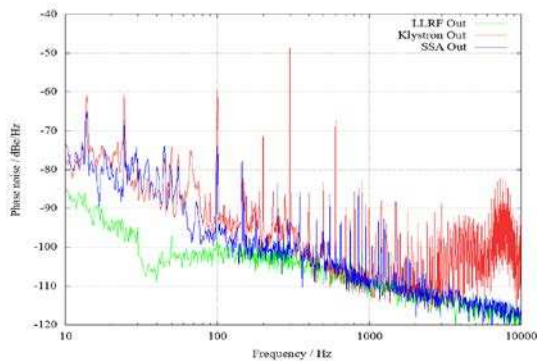


Figure 1: Phase noise vs. frequency.

In the past, phase modulation of the RF frequency with the second harmonic of the synchrotron frequency had increased the beam lifetime in user operation by up to two hours. Its re-implementation using the DLLRF in two-cavity mode turned out to be tricky. The synchrotron frequency increases from 15.6 MHz to 23.4 MHz in two-cavity mode. Due to the FWHM bandwidth of the cavity of about 40 kHz, a significantly increased modulation amplitude is thus required. Furthermore, both cavities with their different power amplifiers have to be modulated synchronously. The new phase modulation scheme uses a hardware trigger to synchronize both cavities. First measurements in two-cavity mode show a somewhat lower lifetime increase of 1.5 hours compared to the previous single-cavity operation, and further studies are required.

Commissioning of New Orbit Correction Software at DELTA

S. Kötter

Center for Synchrotron Radiation (DELTA), TU Dortmund, 44227 Dortmund, Germany

A new software for the slow orbit feedback of the storage ring at DELTA is in the final stages of commissioning [1]. It is set to replace the old program in operation since 2005 [2]. The new software features minimized steerer currents and allows to place limits on orbit deviations. After being tested throughout the first half of 2020, it was introduced to user operation in August.

The performance of the new and old software was assessed by monitoring their ability to correct the orbit drift introduced by the superconducting asymmetric wiggler (SAW) in February. Both programs used the same weights and reference orbit. Histograms of the deviation of the orbit from the reference orbit are given for the horizontal plane of the beam position monitors (BPMs) 42 and 44 in Figure 1. The correction quality in these BPMs determines the orbit in the undulator U55 and hence influences radiation intensity available at beamline 11. The smaller standard deviations achieved by the new software assert its ability to maintain a better orbit correction during SAW operation than the old software.

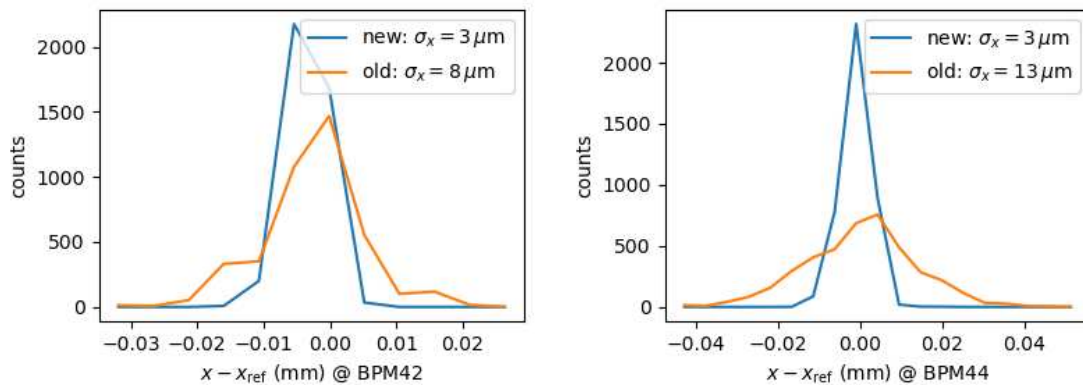


Figure 1: Horizontal deviation of the orbit from the reference orbit at BPM42 (left) and BPM44 (right).

References

- [1] S. Kötter, A. Glassl, B. Isbarn, D. Rohde, M. Sommer, and T. Weis, “Evaluation of an interior point method specialized in solving constrained convex optimization problems for orbit correction at the electron storage ring at DELTA”, in *Proc. IPAC’18*, paper THPAK114, Vancouver, Canada, May 2017.
- [2] M. Grewe, “Orbitkorrektur am Speicherring DELTA”, dissertation, TU Dortmund University, January 2005.

Observation of Edge Radiation at DELTA

S. Khan, B. Büsing, A. Held, D. Krieg, C. Mai

Zentrum für Synchrotronstrahlung (DELTA), Technische Universität Dortmund

Edge radiation (ER) is a type of synchrotron radiation which is usually given little attention. The theory behind ER is reviewed in [1]. The electron motion projected onto the axis of a straight section in a storage ring appears to be accelerated at the end of the preceding dipole magnet and decelerated at the beginning of the next dipole. This results in an intense interference pattern of concentric circles with radial polarization, which depends in detail on the distance between the dipoles, their bending radii, and the observed wavelength. Thus, the mere presence of two dipole edges acts like an insertion device. Among other possible applications, visible ER was proposed as a tool for transverse beam diagnostics [2,3], since the interference pattern is sensitive to the finite beam size.

First experiments to observe ER in the straight section of the undulator U250 at DELTA were undertaken early in 2020. In addition to the standard setup (Fig. 1a), ER was observed with a magnetic chicane at the U250 center (Fig. 1b) giving rise to a more complex interference pattern, as well as coherently emitted ER from laser-induced energy modulation and subsequent microbunching in the U250 (Fig. 1c) [4]. Preliminary results are presented below.

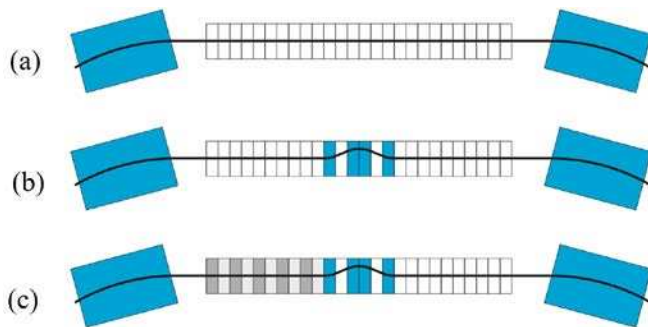


Figure 1: Straight section of the undulator U250 at DELTA with adjacent dipole magnets. ER was observed in three configurations with filled rectangles indicating active magnets:

(a) undulator off; (b) chicane magnets on; (c) upstream part of U250 and chicane magnets on.

In configurations (a,b) of Fig. 1, ER was first visually observed on a paper screen and images were taken with a digital camera – see Fig. 2. The interference fringes are clearly more pronounced as function of the vertical coordinate, an effect of the vertical emittance being smaller than the horizontal one. Interference with incoherent radiation from the dipole may further suppress the horizontal fringes. A quantitative understanding of the pattern will require more data and a numerical simulation of the emission process. Furthermore, the fringes change significantly, when a magnetic chicane introduced at the center of the straight section (configuration of Fig. 1b). The bottom row of Fig. 2 shows vertical fringes under variation of the chicane current.

The fiber end of a CCD spectrometer was moved vertically through the interference pattern showing the expected variation of the fringe separation with photon energy – see Fig. 3 (left).

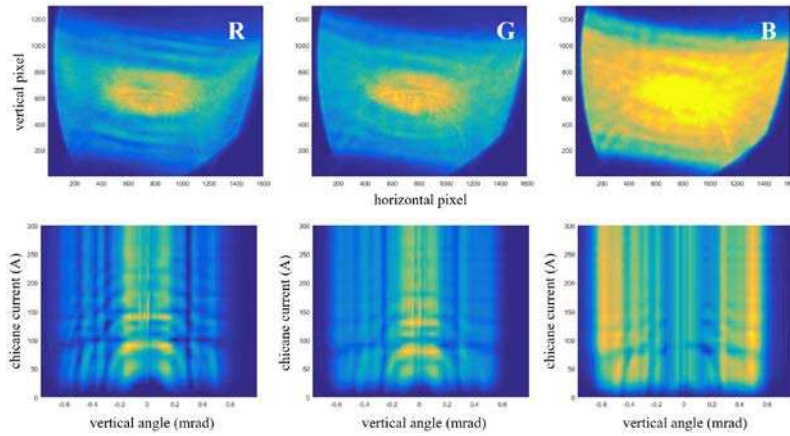


Figure 2: RGB color components of an image of ER on a paper screen taken with a digital camera. Top: Raw images. Bottom: Projected vertical fringes for different chicane magnet currents.

Interaction of femtosecond laser pulses in the upstream part of the U250 (Fig. 1 c) causes a periodic modulation of the electron energy with a periodicity of 800 nm, the laser wavelength. The chicane converts the energy modulation into microbunching giving rise to coherent emission at the laser wavelength and harmonics thereof [4]. Despite the downstream part of the U250 being off, intense radiation was observed depending on the longitudinal laser-electron overlap and on the chicane magnet current. The pattern recorded with a gated image-intensified CCD camera, as shown in Fig. 3 (right), suggests ER from the edges of the last chicane magnet and the subsequent dipole. To our knowledge, this is the first observation of coherently emitted ER (ChEER)* which may, for example, turn out to be a sensitive and inexpensive diagnostics method for electron bunches in free-electron lasers.

* in German: Kohärent emittierte Kantenstrahlung (KeKs)

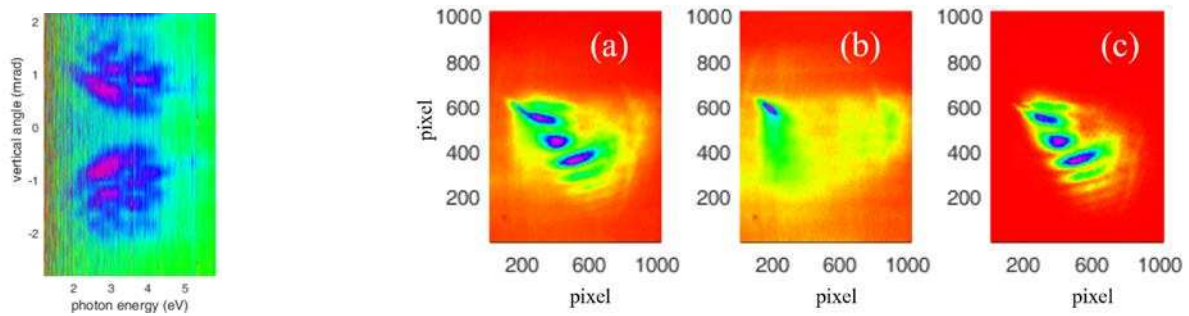


Figure 3: Left: Spectral and (vertical) angular distribution of ER. Right: ER with laser-electron interaction (a), ER without interaction (b), and background-subtracted image (c).

References

- [1] G. Geloni, “Theory of Edge Radiation”, DESY Report 08-118 (2008); Nucl. Instrum. Methods A 605, p. 409 (2009); Nucl. Instrum. Methods A 607, p. 470 (2009).
- [2] O. V. Chubar and E. S. Masunov, "Electron Beam Diagnostics by Means of Edge Radiation," Proc. of PAC'93, Washington, DC, USA, p. 2474 (1993).
- [3] N. Smolyakov et al., A. Hiraya and H. Yoshida, “Edge Radiation and Electron Beam Diagnostics”, Proc. of EPAC'98, Stockholm, Sweden, p. 1604 (1998).
- [4] S. Khan et al., “Generation of Ultrashort and Coherent Radiation Pulses at DELTA”, Synch. Rad. News 26:3, p. 25 (2013).

Status of the beamline BL2

Marvin Kowalski, Michael Paulus, Eric Schneider, Thorsten Witt, Christian Sternemann, Metin Tolan

Fakultät Physik/DELTA, TU Dortmund, 44221 Dortmund, Germany

The beamline BL2 uses radiation of a DELTA bending magnet with a critical photon energy of 2.1 keV. The polychromatic beam is hardened through an aluminum filter (0.2 mm) to eliminate the low energy part of the radiation. The beam then passes through a π -white beam slit system and is typically limited to a beam size of $0.5 \cdot 0.5 \text{ mm}^2$. The white beam can now be used for energy dispersive fluorescence spectroscopy or can be monochromatized by a Pd/B₄C multilayer monochromator with a bandwidth of 1.5%. The photon flux behind the monochromator is around $3 \cdot 10^9 \text{ photons}/(\text{s} \cdot 100 \text{ mA} \cdot \text{mm}^2)$ at photon energies between 10 and 15 keV.

The detectors accessible are a PILATUS 100k, a MAR345 image plate system and an Amptek X-123 spectrometer. High pressure equipment (up to 5 kbar) and temperature controlled cells (100 K -1200 K) are available as sample environments. Due to the low energy resolution of the monochromator, the beamline is particularly well suited for the investigation of disordered systems using small angle X-ray scattering (SAXS) and wide angle X-ray scattering (WAXS).

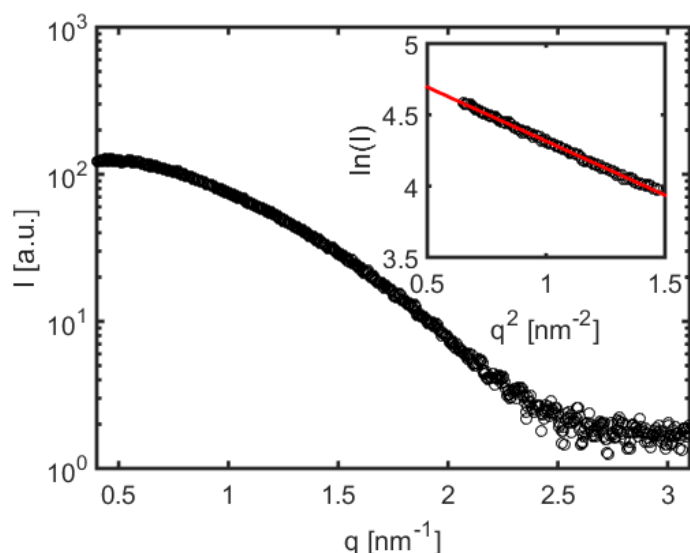


Figure 1: SAXS data of a 1wt% lysozyme solution. The inset shows the Guinier representation.

The control of the MAR345 detector was combined with the control of a fast shutter system using Python to automatically acquire SAXS spectra. Furthermore, a vacuum flight path with a length of 1100 mm and a diameter of 200 mm was constructed to suppress scattered radiation caused by the transmitted beam behind the sample. For a precise adjustment of the beamstop in front of the MAR345 detector, the detector inclusive beamstop were mounted on translation stages. The beamline control has been extended by a second Standa motor controller system, which now allows to address all motors (slit systems, monochromator stage, sample stage and detector stage) independently. First SAXS measurements were performed on lipid systems and lysozyme solutions under high hydrostatic pressures. Figure 1 shows an example of the SAXS signal of a 1wt% lysozyme solution recorded with the new setup. The measurement time was 60 s. Lysozyme from chicken egg white was obtained from Sigma-Aldrich and dissolved in 25 mM Bis-Tris buffer. In addition to the measurement with lysozyme a measurement with pure buffer was recorded, which was subtracted from the protein measurement in an unscaled manner. The inset of fig.1 shows the data in Guinier representation including a linear fit to the data yielding a radius of gyration of $1.51 \pm 0.2 \text{ nm}$. This radius agrees with literature values for lysozyme [1].

Acknowledgments: We acknowledge the DELTA machine group for providing synchrotron radiation and technical support.

[1] C. Krywka, C. Sternemann, M. Paulus, N. Javid, R. Winter, Ali Al-Sawalmih, Sangbong Yi, D. Raabe, M. Tolan, *The small-angle and wide-angle x-ray scattering setup at beamline BL9 of DELTA*, Journal of Synchrotron Radiation **14**, 244 (2007).

Soft X-ray Spectroscopy

Structural analysis of TiN nanoparticle reinforced CrN thin films

Wolfgang Tillmann¹, David Kokalj^{1*}, Dominic Stangier¹, Leif Hagen¹,
Lukas Kesper², Ulf Berges², Carsten Westphal², Christian Sternemann²,
Michael Paulus²

¹Institute of Materials Engineering, TU Dortmund University, Germany
44227 Dortmund, Leonhard-Euler-Straße 2

²Experimental Physics 1 / DELTA, TU Dortmund University, Germany
44227 Dortmund, Maria-Goeppert-Mayer-Straße 2

* corresponding author: david.kokalj@tu-dortmund.de

Nanocomposite thin films are composed of at least two phases and considered as coatings of the third generation (1 fort). The mechanical properties of nanocomposites, such as high hardness and at the same time good ductility, can be attributed to the high proportion of interfaces in the total volume [1]. The synthesis of nanocomposites is based on the spinodal decomposition in at least two phases [2]. In this respect, a sufficiently high separation temperature is required, which enables segregation into two phases on the basis of a controlled diffusion [3]. In addition to the thermodynamic driven processes, the choice of the coating material determines a potential nanocomposite formation. Basically, the formation of the nanocomposite structure is based on the insolubility of the two phases, which is only given if one of the three cases (different nitrogen affinity, miscibility gap, crystalline/amorphous structure) occurs [4]. Therefore, the possible material combinations in terms of technically relevant transition metal nitrides are restricted and a solid solution structure is preferred.

In this study, the two most industrially used thin films TiN and CrN were used to deposit artificial nc-TiN/nc-CrN nanocomposites. As stated in the literature, conventional sputtering of CrTiN thin films leads to the formation of (Cr,Ti)N solid solutions for Ti/(Cr+Ti) ratios of 0 % - 37 % and 54 % - 86 % [5-7]. The approach is based on the locally separated production of the two phases and the simultaneous deposition on the substrate. In that regard, TiN nanoparticles were synthesized using an atmospheric-pressure arc reactor, while the CrN thin film was deposited by means of dc magnetron sputtering. An aerodynamic lens system was used to transfer the nanoparticles into the PVD chamber and to compensate the pressure differences.

The phase analysis of the thin films and nanoparticles was performed at beamline 9 by means of 2D grazing incidence XRD (GI-XRD) using an image plate detector MAR345. For the experiments the photon energy was set to $E = 20$ keV and the incident angle to $\omega = 0.5^\circ$. The chemical binding of the samples was analyzed at beamline 11 by the use of X-ray photoelectron spectroscopy (XPS). Relating to this, high resolution XPS measurements were performed for the N 1s, Cr 3p and Ti 3p orbitals.

The results of the XRD measurements of the thin films and nanoparticles are shown in Figure 1. The reference CrN thin film can be assigned to polycrystalline structure of the cubic CrN pattern (JCPDS 65-2899). The structure of the TiN Nanoparticles matches to the polycrystalline cubic TiN reference (JCPDS 38-1420). The pattern of the CrTiN thin film deposited on the steel substrate (1.2343) is comparable to the CrN reference thin film and shows no reflections belonging to the nanoparticles, although crystalline nanoparticles are embedded in the CrN thin film as proven by STEM investigations [8]. Therefore, the absence of the TiN reflections is attributed to the low nanoparticle content. In addition to the 3 μm thick CrTiN thin film on the steel substrate, a 80 nm thick CrTiN coating was deposited on a TEM-grid. The (200) reflection of the coated TEM-grid shows an asymmetry. The corresponding cumulative peak fit, using a Pearson VII fit, is shown in Figure 1b) for the (200) and (220) reflections. Peak 1 and Peak 3 correspond to the TiN pattern, whereas Peak 2 and Peak 4 correspond to the CrN reference pattern. Accordingly, the two-phase nanocomposite structure consisting of the superposition of the CrN-PVD and TiN-nanoparticle reflections could be detected.

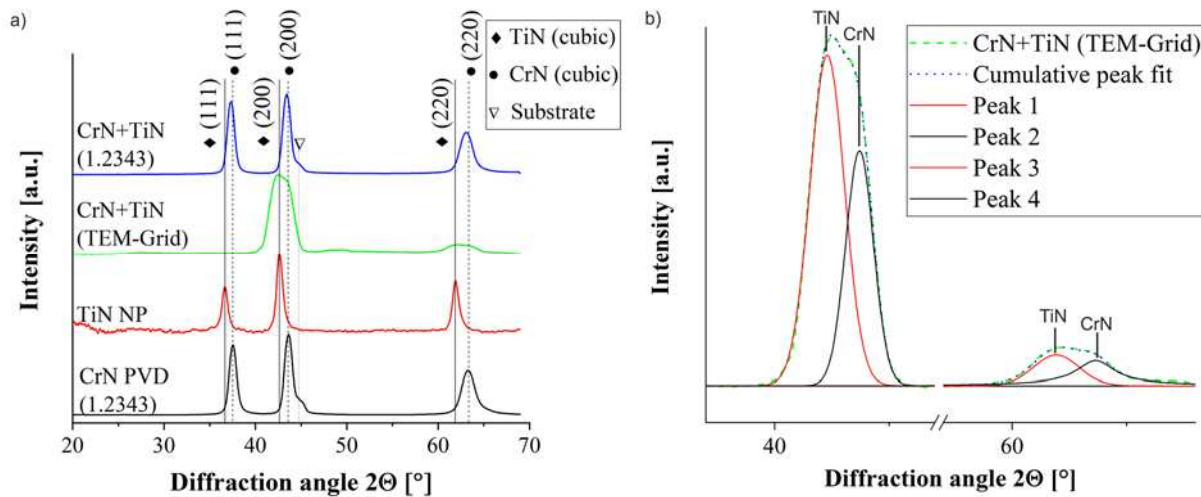


Figure 1: a) GI-XRD patterns of the reference CrN thin film, the TiN nanoparticles as well as the nanostructured CrTiN thin film and b) corresponding cumulative peak fit of the CrTiN thin film [8]

The 2D-patterns were used to calculate texture plots of the (111) and (200) reflections of the Cr(Ti)N thin films and the TiN nanoparticles (Figure 2). The reference CrN thin film reveals a maximum intensity of the (111) reflection at an azimuthal angle of approximately 90°, indicating an out-of-plane orientation. Compared to this thin film, the nanocomposite CrTiN thin film reveals no distinct peak. Accordingly, the incorporation of TiN nanoparticles causes a reduction of the texture. For the TiN nanoparticles themselves, no variation over the azimuthal angle of the (111) and (200) reflections are detected, excluding any texture. In case of the (200) reflections, no significant differences between the CrN and CrTiN thin film are to mention.

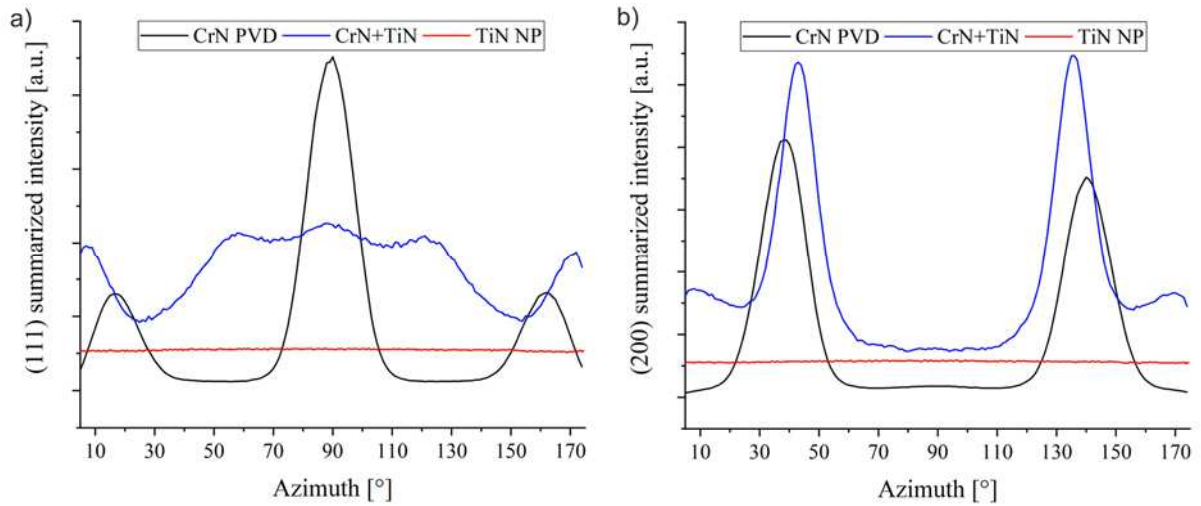


Figure 2: Texture plot of the a) (111) and b) (200) reflection of the thin films and nanoparticles [8]

To evaluate the embedment of the nanoparticles in the film, the chemical binding of the elements was analyzed by means of high-resolution XPS. As shown in the N 1s spectra, Ti-N bonds of the nanoparticles can be detected in the thin films. No direct bonds of Ti and Cr are observed, indicating the absence of mixed crystal formation of CrN and TiN, for example at the particle-thin film interface, occurred. Combined with the diffraction experiments, it is confirmed that the chosen approach of the decentralized phase formation enables the synthesis of a composite structure for conventionally mixable phases. However, the injection of the TiN nanoparticles leads to a change in the average component ratio of Cr (metal) and Cr-N (Figure 3a) based on the Cr 3p orbital. Regarding this, the fraction of Cr-N bonds increases with the TiN nanoparticle content. The increased proportion of Cr-N bonds in the nanoparticle containing thin films can be related to the fact that a small amount of the synthesis gas, consisting of an argon and nitrogen mixture, of the TiN nanoparticles is additionally introduced into the PVD chamber with the nanoparticles.

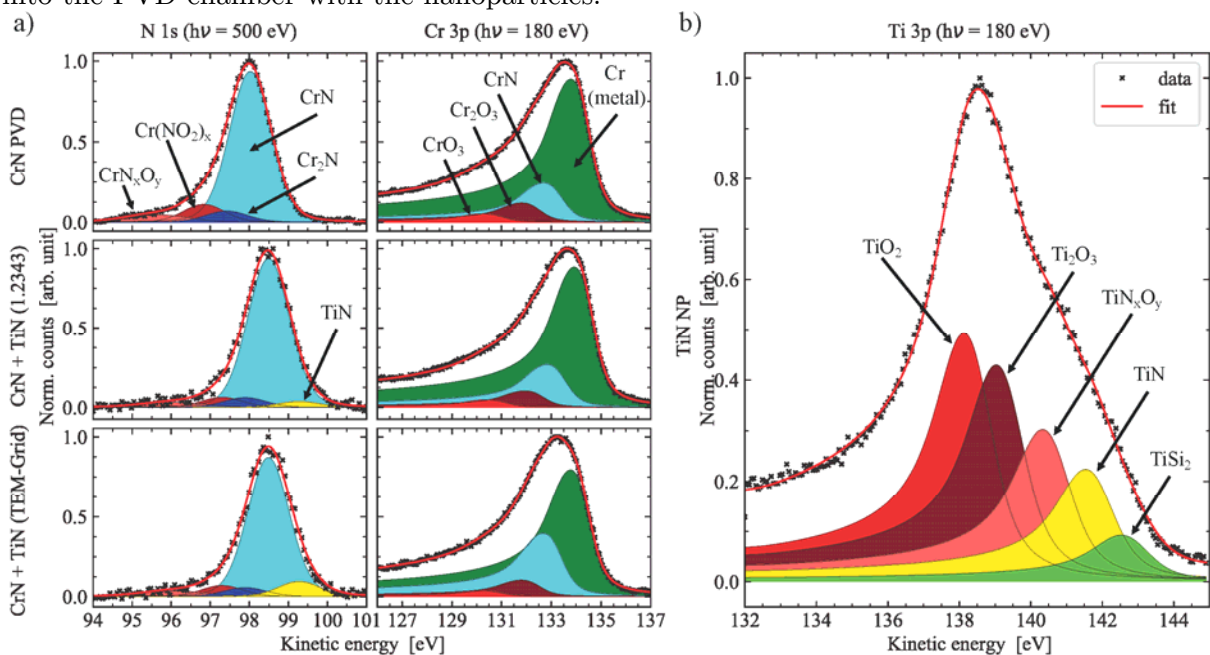


Figure 3: High-resolution XPS spectra of the a) N 1s and Cr 3p orbitals of the CrN and CrTiN thin films and b) Ti 3p orbital of the TiN nanoparticles [8]

Acknowledgements

The authors gratefully acknowledge the DELTA machine group for providing synchrotron radiation and their support at BL9 and BL11. In addition, the Deutsche Forschungsgemeinschaft (DFG, German Research Foundation) is acknowledged for the financial support within the project 382368006 (TI343/135-1, KR1723/20-1).

References

- [1] S.C. Tjong, H. Chen, Nanocrystalline materials and coatings, *Materials Science and Engineering: R: Reports* 45 (2004) 1–88. <https://doi.org/10.1016/j.mser.2004.07.001>.
- [2] K. Lukaszowicz, Review of Nanocomposite Thin Films and Coatings Deposited by PVD and CVD Technology, in: M. Rahman (Ed.), *Nanomaterials*, InTech, 2011.
- [3] R.F. Zhang, S. Veprek, On the spinodal nature of the phase segregation and formation of stable nanostructure in the Ti–Si–N system, *Materials Science and Engineering: A* 424 (2006) 128–137. <https://doi.org/10.1016/j.msea.2006.03.017>.
- [4] S. Reich, M. Schadewald, M. Bornemann, PVD-Nanocomposite-Beschichtungen für die Zerspanungs- und Umformtechnik, *Materialwissenschaft und Werkstofftechnik* 38 (2007) 108–111. <https://doi.org/10.1002/mawe.200600115>.
- [5] G.A. Zhang, P.X. Yan, P. Wang, Y.M. Chen, J.Y. Zhang, The structure and tribological behaviors of CrN and Cr–Ti–N coatings, *Appl Surf Sci.* 253 (2007) 7353–7359. <https://doi.org/10.1016/j.apsusc.2007.02.061>.
- [6] C. Paksunchai, S. Denchitcharoen, S. Chaiyakun, P. Limsuwan, Growth and Characterization of Nanostructured TiCrN Films Prepared by DC Magnetron Cosputtering, *Journal of Nanomaterials* 2014 (2014) 1–9. <https://doi.org/10.1155/2014/609482>.
- [7] W. Tillmann, D. Kokalj, D. Stangier, Q. Fu, F.E. Kruis, L. Kesper, U. Berges, C. Westphal, On the synthesis and structural evolution of artificial CrN/TiN nanocomposites, *Applied Surface Science* 535 (2021) 147736. <https://doi.org/10.1016/j.apsusc.2020.147736>.

Examination of thin boron layers on a Si(100) surface - PureB by means of x-ray photoelectron spectroscopy

A. Burkowitz^{1,2}, M. Schmitz^{1,2,*}, L. Kesper^{1,2}, U. Berges^{1,2}, S. Dreiner³, D. Weier³, L.K. Nanver⁴, and C. Westphal^{1,2}

¹ Experimentelle Physik I - Technische Universität Dortmund, Otto-Hahn-Str. 4a, D-44221 Dortmund

² DELTA - Technische Universität Dortmund, Maria-Goeppert-Mayer-Str. 2, D-44221 Dortmund

³ Fraunhofer-Institut für Mikroelektronische Schaltungen und Systeme IMS, Finkenstr. 61, D-47057 Duisburg

⁴ Universität Twente, Drienerlolaan 5, 7522 NB Enschede, Niederlande

* corresponding author: marie.schmitz@tu-dortmund.de

The system of thin boron layers on a silicon surface, known as PureB is of great technological interest. PureB detectors yield excellent results in the detection of ultraviolet light [1, 2] and low-energy electrons [2, 3]. The detection process requires rather small p-n-junctions in the range of 10 nm. Those systems can be realized by either doping silicon detectors with boron, or preparing a boron layer on top of the silicon substrate [4]. The latter show a sensitivity near theoretical calculations, a good robustness [1, 2, 5], and also an extreme low leakage current [6]. To understand the origin of their properties it is crucial to investigate the chemical structure of the PureB-layer. An excellent method for a surface- and interface sensitive chemical analysis is x-ray photoelectron spectroscopy. Using synchrotron radiation from beamline 11 of the Dortmund electron storage ring (DELTA) we investigated two different preparation methods of a PureB system. Initially a 3,3 nm thick boronlayer on a Si(100)-surface, prepared by chemical vapor deposition, is analyzed. As the samples are heated at temperatures of 400°C, 700°C, and 950°C during the preparation process a temperature dependent XPS measurement were conducted after each heating step. The XPS high-resolution spectra reveal, that the bonds of boron with oxygen, carbon, and nitrogen occur in the entire boron layer. This indicates, that most of the contamination was inserted into the system during fabrication. To improve the sample quality, while reducing foreign atoms, different methods of preparing and storing the samples are tested. The transport of the sample under a protective gas atmosphere and also sputtering of the surface does not yield a good improvement. Further a set of samples was prepared via physical vapor deposition under UHV-conditions in-house. One monolayer Boron was evaporated onto a Si(100)-surface. The XPS measurements revealed a reduced contamination at the surface. Furthermore XPS high-resolution spectra of the B 1s and the Si 2p orbital revealed covalent bonds between boron and silicon. [6]

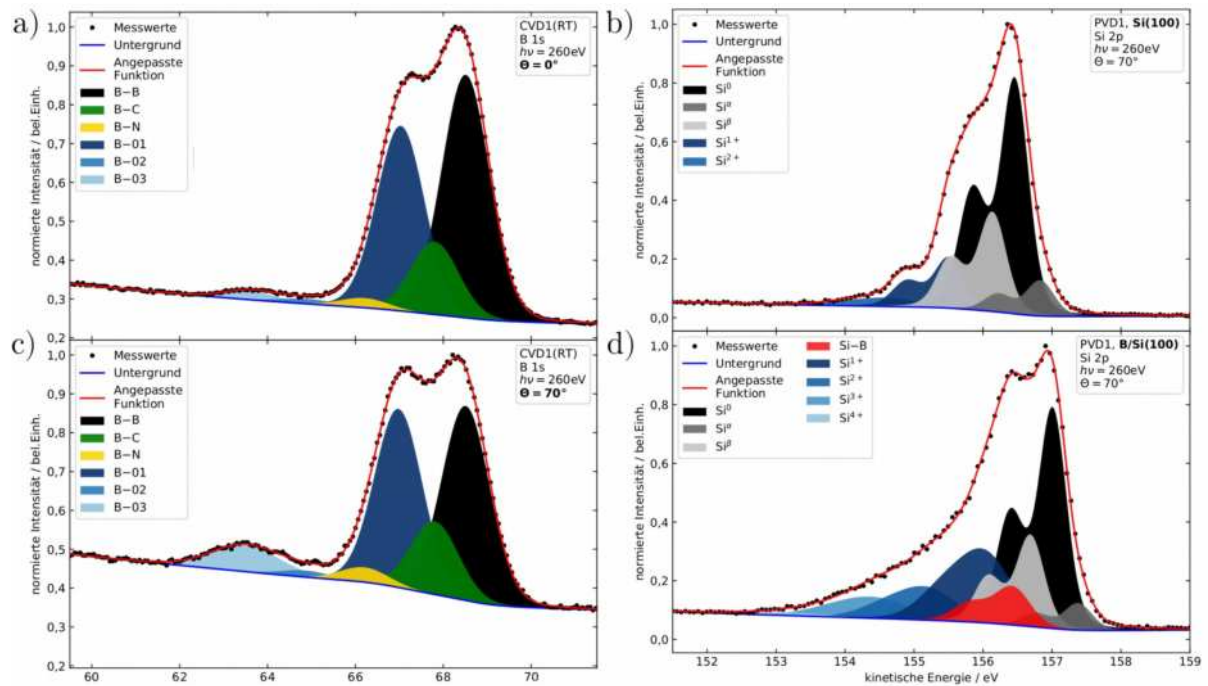


Figure 1: High-resolution XPS spectra of the B 1s and the Si 2p signal at a photon energy of $h\nu=260\text{eV}$. a) and c) display the B 1s spectra of the first PureB sample, fabricated via chemical vapor deposition, measured at an angle of $\Theta=0^\circ$ and at the surface sensitive angle of $\Theta=70^\circ$. The spectra in b) and d) show the growth of a Si-B component, b) before and d) after the deposition of B onto the Si(100) surface using physical vapor deposition.

References

- [1] L. K. Nanver *et al.*, IEEE Journal of Selected Topics in Quantum Electronics **20**, 306-316 (2014).
- [2] V. Mohammadi *et al.*, IEEE Electron Device Letters **34**, 1545-1547 (2013).
- [3] A. Sakic *et al.*, 2010 International Electron Devices Meeting, 31-4 (2010).
- [4] F. Sarubbi *et al.*, Journal of Electronic Materials **39**, 162-173 (2010).
- [5] L. Shi *et al.*, IEEE Transactions on Electron Devices **60**, 346-353 (2012).
- [6] A. Burkowitz, Master thesis, TU Dortmund University, 2020

Influence of Sputtered Carbon on the Development of Amorphous Phases in CrAlCN DC/HiPIMS PVD Coatings

Wolfgang Tillmann¹, Dominic Stangier^{1*}, David Kokalj¹, Leif Hagen¹,
Peter Roesse², Karim Shamout², Marie Schmitz², Lukas Kesper²,
Annika Burkowitz², Ulf Berges², Carsten Westphal²

¹Institute of Materials Engineering, TU Dortmund University, Germany
44227 Dortmund, Leonhard-Euler-Straße 2

²Experimental Physics 1 / DELTA, TU Dortmund University, Germany
44227 Dortmund, Maria-Goeppert-Mayer-Straße 2

* corresponding author: dominic.stangier@tu-dortmund.de

CrAlN coatings processed by physical vapor deposition (PVD) have been in the focus of research for many years due to their excellent mechanical and tribological properties to enhance the performance and service life of tools and components [1–5]. In addition to the benefits provided in the field of wear resistance and oxidation resistance [6–9] as well as the phase stability for high temperature applications [10,11] these coatings show high friction values sliding against steel counter-bodies leading to a limitation of possible application fields. Therefore, the tailoring of the tribological properties by doping and alloying additional elements to the ternary CrAlN system is of great interest and is part of ongoing research [12]. However, the promising approach of doping carbon in the CrAlN system to reduce the coefficient of friction for forming technology has so far only been partly investigated [13,14].

First results presented by Ahn et al. using a changed reactive gas atmosphere by methane and nitrogen reveal improved mechanical properties for the carbon-nitride coating systems [15]. The increased residual stresses, which were in direct correlation to the evolution of the hardness values and the shift of the interplanar distance of the (200) fcc CrAlN phase led to the assumption that the carbon was fully solved in the crystalline lattice. In contrast to these findings, subsequent investigations of the structural composition proved that besides the changes in the crystalline structure the coexistence of an amorphous phase consisting of C-C and C-N components were found [16]. Romero et al. confirmed the presence of the sp^2 hybridized amorphous carbon phase by Raman spectroscopy, whereas any information about the evolution and interaction of the nitrogen in the reactive gas atmosphere is presented [17]. Additionally, a strong influence of the formation of the crystalline Cr phases with carbon was reported, which is caused by the increasing target poisoning during the DC sputtering process. Furthermore, these findings are in good accordance with the strong amorphization of the

CrAlCN thin film, which was also reported by Shtansky et al. for ternary Cr based carbon-nitride coatings [18].

Summarizing the obtained results leads to the conclusion that, although doping of carbon is a highly promising approach for CrAlN systems due to the enhanced tribo-mechanical properties, it also might lead to negative interactions during the growth of thin films caused by the changed reactive atmosphere. For this reason, a new approach by doping CrAlN coatings by using graphite targets as carbon source is chosen. The presented results focus on the fundamental understanding of the evaluation of the amorphous phases by using high-resolution XPS measurements for CrAlCN coatings with varying carbon contents processed by different cathode powers.

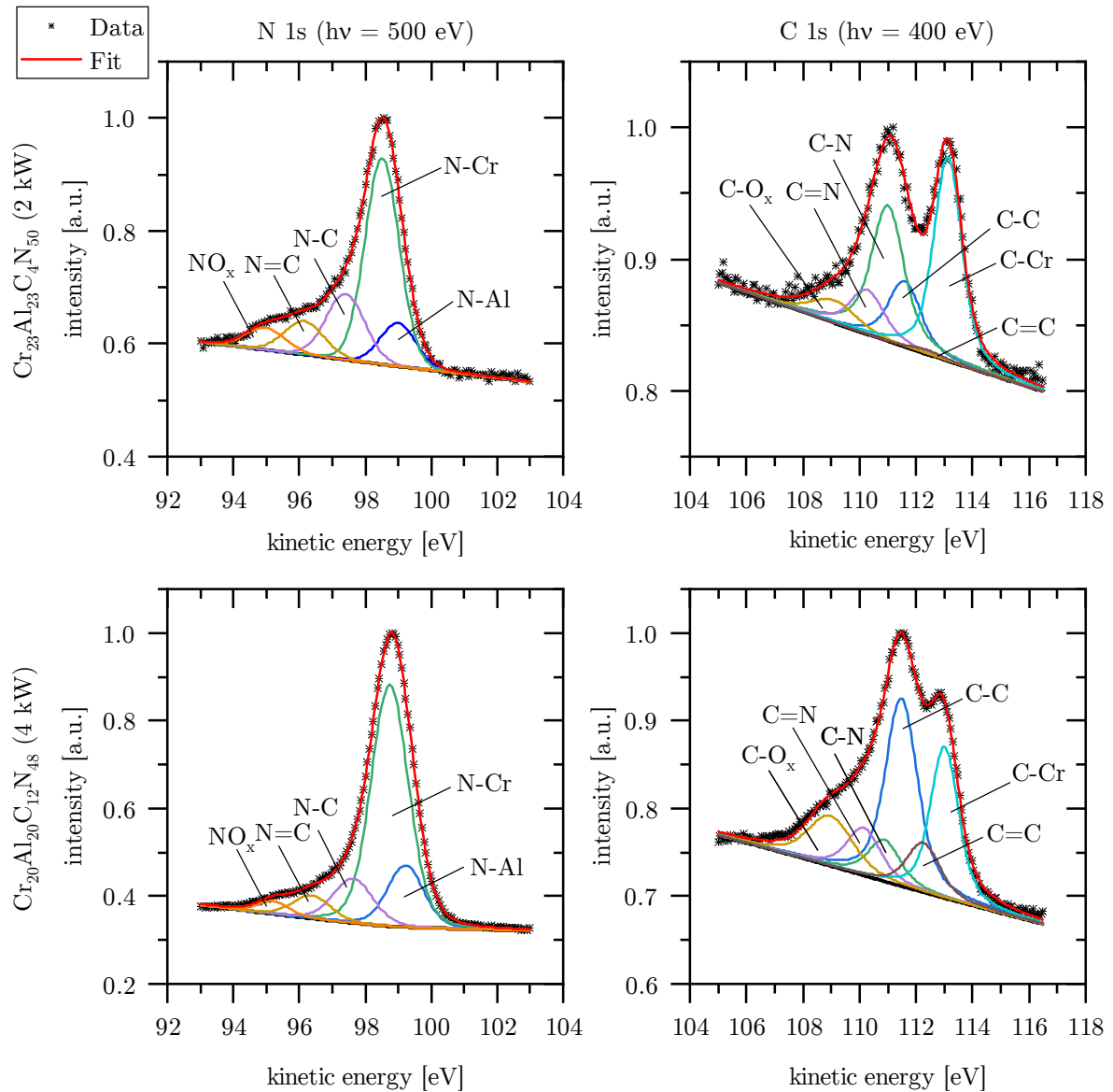


Figure 1: High-resolution XPS core-level spectra of the C 1s and N 1s orbitals for CrAlCN coatings at a polar angle $\Theta = 0^\circ$

As presented in Figure 1 the core-level spectra of the C 1s and N 1s orbital were analyzed with respect to their components to understand the formation of amorphous phases in dependency

of the carbon content for CrAlCN coatings. With respect to the investigation of the N 1s orbital the observed main components are presented by N-Al and N-Cr bondings, as it was already shown for CrAlN coatings [19]. However, even doping the ternary system with small amounts of carbon (4 at. %) the formation of a-CN phases consisting of single and double bonded components was observed. Increasing the cathode power up to 4 kW and increasing the amount of carbon up to 12 at. % no significant changes for the coordination of the nitrogen were found. These results are in good accordance with the findings made for the synthesis by reactive gases in a previous study of the authors [20] and Wang et al. for CrCN coatings [21]. Furthermore, the XPS results prove the presence of oxide components, which can be attributed to the diffusion of oxygen into the coating material. Consistent bonds were detected for the investigation of the C 1s peak. Due to the high affinity of chromium to carbon an additional component for Cr-C was found, which seems to be independent of the carbon content. Additionally, for the higher carbon content an increased formation of C=C bonds was found which is accompanied by a decrease of the C-C component. Therefore, one may propose that the higher carbon content leads to the formation of a carbon rich interlayer, which is an indicator for the formation of a nano-laminar structure of the coating.

To further increase the understanding about the phase formation of the CrAlCN coating system complementary methods such as Raman spectroscopy are required to proof the findings about the coordination and the induced structural changes. With respect to the composition x-ray diffraction will additionally be used to identify the crystalline phases as well as to determine the crystallite size. These analytical methods combined will answer the question whether a nano-laminar or a nanocomposite structure is formed in the CrAlCN system by sputtering carbon from graphite targets.

Acknowledgements

The authors gratefully acknowledge the financial support of the German Research Foundation (DFG) within the transregional collaborative research center TR73 “Manufacturing of complex functional components with variants by using a new sheet metal forming process – Sheet Bulk Metal Forming” project B5 (Application of nanostructured bionic thin layers to enhance the wear and friction behavior of forming tools by thin-walled sheet forming). Furthermore, we would like to thank the DELTA machine group at BL11 for providing synchrotron radiation and their support.

References

- [1] M. Kawate, A. Kimura, T. Suzuki, *Journal of Vacuum Science & Technology A: Vacuum, Surfaces, and Films* 20 (2002) 569–571.
- [2] M. Brizuela, A. Garcia-Luis, I. Braceras, J.I. Oñate, J.C. Sánchez-López, D. Martínez-Martínez, C. López-Cartes, A. Fernández, *Surface and Coatings Technology* 200 (2005) 192–197.
- [3] E. Spain, J.C. Avelar-Batista, M. Letch, J. Housden, B. Lerga, *Surface & Coatings Technology* 200 (2005) 1507–1513.

- [4] X.-Z. Ding, X.T. Zeng, *Surface & Coatings Technology* 200 (2005) 1372–1376.
- [5] N. Bagcivan, K. Bobzin, S. Theiß, *Thin Solid Films* 528 (2013) 180–186.
- [6] M. Kawate, A.K. Hashimoto, T. Suzuki, *Surface and Coatings Technology* 165 (2003) 163–167.
- [7] O. Banakh, P.E. Schmid, R. Sanjinés, F. Lévy, *Surface and Coatings Technology* 163–164 (2003) 57–61.
- [8] Y.C. Chim, X.Z. Ding, X.T. Zeng, S. Zhang, *Thin Solid Films* 517 (2009) 4845–4849.
- [9] J. Lin, B. Mishra, J.J. Moore, W.D. Sproul, *Surface and Coatings Technology* 202 (2008) 3272–3283.
- [10] P.H. Mayrhofer, H. Willmann, A.E. Reiter, *Surface & Coatings Technology* 202 (2008) 4935–4938.
- [11] E. Mohammadpour, Z.-T. Jiang, M. Altarawneh, Z. Xie, Z. Zhou, N. Mondinos, J. Kimpton, B.Z. Dlugogorski, *Thin Solid Films* 599 (2016) 98–103.
- [12] J.L. Endrino, V. Derflinger, *Surface & Coatings Technology* 200 (2005) 988–992.
- [13] W. Tillmann, D. Stangier, P. Schröder, *Surface & Coatings Technology* 308 (2016) 147–157.
- [14] M. Löffler, R. Schulte, D. Freiburg, D. Biermann, D. Stangier, W. Tillmann, M. Merklein, *International Journal of Material Forming* 12 (2019) 17–26.
- [15] S.K. Ahn, S.H. Kwon, K.H. Kim, *Journal of the Korean Physical Society* 54 (2009) 1212–1216.
- [16] S.-K. Ahn, S.-H. Kwon, K.-H. Kim, *Transactions of Nonferrous Metals Society of China* 21 (2011) 78–82.
- [17] E.C. Romero, M.G. Botero, W. Tillmann, F.B. Osorio, G.B. Gaitán, *Bulletin of Materials Science* 41:97 (2018).
- [18] D.V. Shtansky, P.V. Kiryukhantsev-Korneev, A.N. Sheveyko, B.N. Mavrin, C. Rojas, A. Fernandez, E.A. Levashov, *Surface & Coatings Technology* 203 (2009) 3595–3609.
- [19] H.C. Barshilia, N. Selvakumar, B. Deepthi, K.S. Rajam, *Surface & Coatings Technology* 201 (2006) 2193–2201.
- [20] W. Tillmann, D. Stangier, P. Roese, K. Shamout, U. Berges, C. Westphal, J. Debus, *Surface & Coatings Technology* 374 (2019) 774–783.
- [21] Q. Wang, F. Zhou, Z. Zhou, L.K.-Y. Li, J. Yan, *Surface and Coatings Technology* 265 (2015) 16–23.

Investigation of germanene phases on Ag(111) by means of XPS and XPD

L. Kesper^{1,2,*}, M. Schmitz^{1,2}, J. A. Hochhaus^{1,2}, M. G. H. Schulte^{1,2}, U. Berges^{1,2},
and C. Westphal^{1,2}

¹ Experimentelle Physik I - Technische Universität Dortmund, Otto-Hahn-Str. 4a, D-44221 Dortmund

² DELTA - Technische Universität Dortmund, Maria-Goeppert-Mayer-Str. 2, D-44221 Dortmund

* corresponding author: lukas.kesper@tu-dortmund.de

In 2004, first experimental synthesis of graphene as the first 2D-material gave the go-ahead for the quest for counterparts stepping down the carbon group. Two-dimensional materials often form a honeycomb structure, which makes them show extraordinary electronic properties [1]. Most of these characteristics differ significantly from their 3D relatives. For example, so-called two-dimensional Dirac-materials like germanene obtain an outstanding high mobility of charge carriers (massless Dirac fermions) resulting from their Dirac-like dispersion [2]. After the first synthesis of germanene on Au(111) in 2014 [3] various studies on the material properties and its application have been published. Germanene's high atomic number Z and its sp^3 -hybridization induce a strong spin-orbit coupling, as well as a great buckling [4]. This leads to the applicability of remarkable properties such as quantum spin hall effect (QSHE) or behaviour like topological insulators [5, 6]. Due to its tunable bandgap, similar to silicene, [7, 8] even the realization of silicene- and germanene-based field-effect transistors (FET) has been succeeded [9, 10]. Since the surface and interface structure of 2D-materials has major influence on the electronic properties of the material, we focus on the analysis of chemical and atomic structures at the interfaces, as well as the understanding of the electronic properties of materials depending on their structure. Here we report on a structural investigation of the evolution of two-dimensional germanium phases on Ag(111) using photoelectron spectroscopy (XPS) and photoelectron diffraction (XPD).

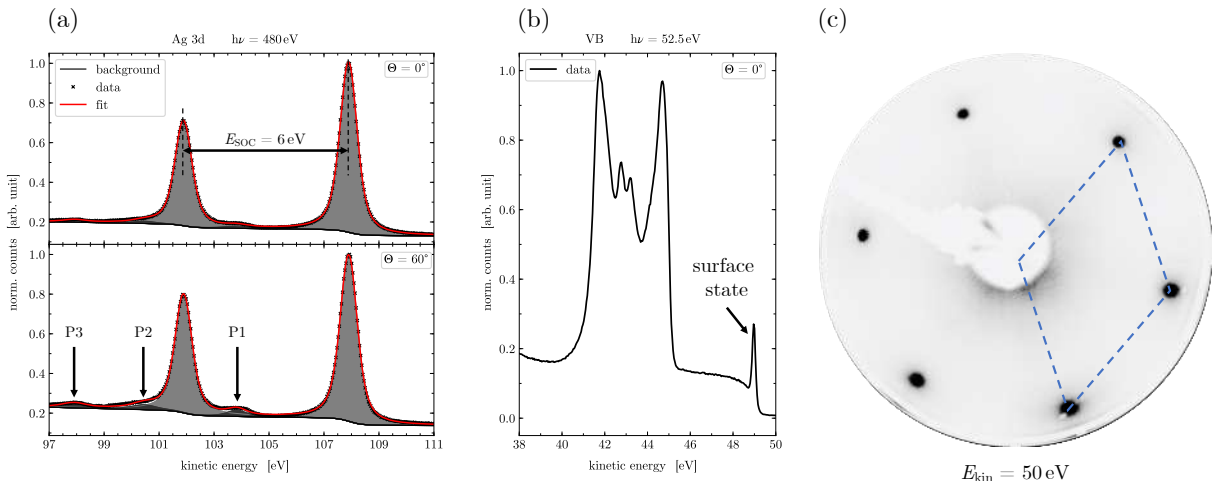


Figure 1: Evidence of clean and highly ordered Ag(111)-surface: (a) High resolved XPS spectra of Ag 3d signal and (b) the valence band signal and (c) additionally sharp LEED-spots of the (1×1) -reconstruction.

Firstly the surface of the Ag(111)-substrate is prepared by several cycles of Argon-ion sputtering with $E_{Ar^+} = 600$ eV and annealing to 720 K. All preparation and measurement steps are conducted in an ultra-high vacuum chamber at beamline 11 (BL11) at DELTA with a base pressure of $p = 6 \times 10^{-11}$ mbar. To check the cleanness and reconstruction of the surface LEED and XPS-measurements are performed, shown in figure 1. The sharp LEED-spots of the diffrac-

tion pattern, presented in figure 1(c), corresponds to the (1×1) -reconstruction of Ag(111), highlighted by the blue dashed line and indicate the successful preparation of the surface. Additionally, the XPS measurements performed at BL11 using synchrotron radiation generated by the undulator U55, do not reveal any chemical residues on the surface. XPS spectra in high energy resolution of the Ag 3d signal, shown in figure 1(a), are recorded under normal emission ($\Theta = 0$) and oblique emission ($\Theta = 60$), with higher surface sensitivity. Here features of surface plasmons P1, P2 and P3 can be identified [11]. Having a closer look at the valence band spectra, illustrated in figure 1(b), reveals the surface state signal of Ag(111) [12]. This is in addition to the surface plasmon feature the final proof for a perfectly cleaned and ordered surface.

Subsequently thin films of germanium with increasing thickness is deposited on the Ag(111) surface by PVD procedure, using an electron-beam evaporator. Figure 2(a) shows XPS survey spectra of two different layer thicknesses, which are estimated by quartz micro balance measurements as 0.2 ML and 1 ML, respectively. With a deposited amount of 0.2 ML the LEED pattern, shown in the upper part of figure 2(b) becomes visible. The superstructure, represented by the blue and red dashed line as markers for the unit cell of silver and germanium, is identified as $(\sqrt{3} \times \sqrt{3})R30$ -reconstruction. Increasing the film thickness to 1/3 ML reveals several satellite features surrounding the main spots of the $(\sqrt{3} \times \sqrt{3})R30$ -reconstruction, which leads to a more complex substructure matrix. In agreement to further studies an Ag_2Ge surface alloy can be observed[12–14], which will not be discussed in detail here. The analysis of high resolution spectra of the Ag 3d and the Ge 3d signal, given in figure 2(b) and (c), delivers no second components, representing interface bonds. Therefore, both spectra indicate no interaction between germanium and silver. The preliminary phase to the surface alloy seems to consist of physically absorbed germanium clusters. A coverage of around 1 ML corresponds to germanene, forming

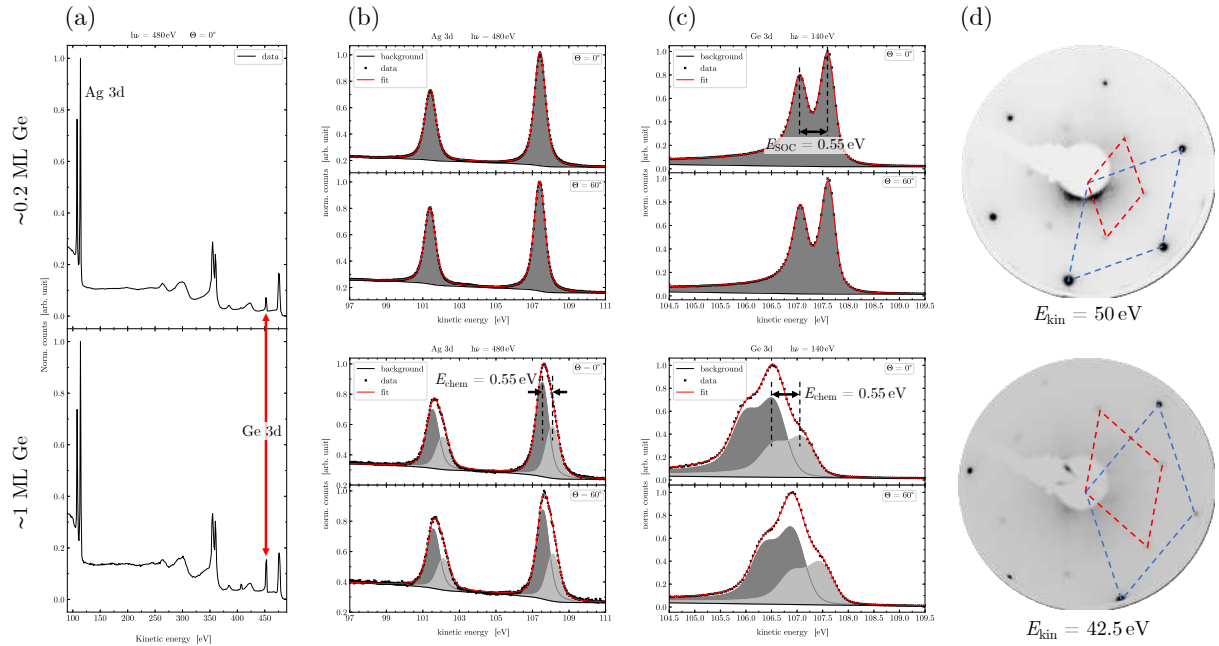


Figure 2: (a)-(c) display XPS spectra to determine the chemical composition and bonding structure of two different layer thicknesses of 0.2 ML (top) and 1 ML (bottom). (d) The LEED-pattern reveal, but slightly different superstructures for both systems similar.

a so-called quasi-freestanding phase [13]. The survey spectra in figure 2(a) confirm the raised layer thickness by increasing counts of the Ge 3d signal, as marked by the red arrow, inducing a phase transition as to conclude from the slightly but clear change of the superstructure. Additionally the high resolution XPS-spectra, displayed in (b) and (c) show a significant change in peak shape for higher coverages. A second component is added to each signal, representing

interface bondings between the silver substrate and germanium atoms.

For further investigation a greater number of different layer thicknesses are going to be scanned by XPS to determine the origin of the interface bonds. It might be either a feature from a mixed phase of the surface alloy and the quasi-freestanding phase or the evidence for a bonding between the quasi-freestanding germanene phase and the substrate. Additionally XPD-measurements will be performed to resolve the internal and interfacial structure of two-dimensional germanium. The milestone to clarify the disagreement in literature about the presence and the structure of freestanding germanene on Ag(111) needs to be reached.

References

- [1] A. Molle, J. Goldberger, M. Houssa, Y. Xu, S. C. Zhang, and D. Akinwande, *Nat. Mater.* **16**, 163 (2017).
- [2] T. O. Wehling, A. M. Black-Schaffer, and A. V. Balatsky, *Adv. Phys.* **63**, 1 (2014).
- [3] M. E. Dávila, L. Xian, S. Cahangirov, A. Rubio, and G. Le Lay, *New J. Phys.* **16**, 095002 (2014).
- [4] P. Vogt, *Beilstein J. Nanotechnol.* **9**, 2665 (2018).
- [5] C. C. Liu, W. Feng, and Y. Yao, *Phys. Rev. Lett.* **107**, 076802 (2011).
- [6] M. Ezawa, *J. Phys. Soc. Japan* **84**, 1 (2015).
- [7] Z. Ni, Q. Liu, K. Tang, J. Zheng, J. Zhou, R. Qin, Z. Gao, D. Yu, and J. Lu, *Nano Lett.* **12**, 113 (2012).
- [8] M. Ye, R. Quhe, J. Zheng, Z. Ni, Y. Wang, Y. Yuan, G. Tse, J. Shi, Z. Gao, and J. Lu, *Phys. E Low-Dimensional Syst. Nanostructures* **59**, 60 (2014).
- [9] L. Tao, E. Cinquanta, D. Chiappe, C. Grazianetti, M. Fanciulli, M. Dubey, A. Molle, and D. Akinwande, *Nat. Nanotechnol.* **10**, 227 (2015).
- [10] B. N. Madhushankar, A. Kaverzin, T. Giouis, G. Potsi, D. Gournis, P. Rudolf, G. R. Blake, C. H. Van Der Wal, and B. J. Van Wees, *2D Mater.* **4**, 021009 (2017).
- [11] J. Leiro, E. Minni, and E. Suoninen, *J. Phys. F Met. Phys.* **13**, 215 (1983).
- [12] H. Oughaddou, S. Sawaya, J. Goniakowski, B. Aufray, G. Le Lay, J. M. Gay, G. Tréglia, J. P. Bibérian, N. Barrett, C. Guillot, A. Mayne, and G. Dujardin, *Phys. Rev. B* **62**, 16653 (2000).
- [13] C. H. Lin, A. Huang, W. W. Pai, W. C. Chen, T. Y. Chen, T. R. Chang, R. Yukawa, C. M. Cheng, C. Y. Mou, I. Matsuda, T. C. Chiang, H. T. Jeng, and S. J. Tang, *Phys. Rev. Mater.* **2**, 1 (2018).
- [14] K. Zhang, R. Bernard, Y. Borenstein, H. Cruguel, and G. Prévot, *Phys. Rev. B* **102**, 125418 (2020).

Chemical investigation a of graphene/cobalt/platinum multilayer system on silicon carbide

P. Weinert^{1,2,*}, R. Hönig^{1,2}, L. Kesper^{1,2}, U. Berges^{1,2}, C. Westphal^{1,2}

¹ Experimentelle Physik I - Technische Universität Dortmund, Otto-Hahn-Str. 4a, D-44221 Dortmund

² DELTA - Technische Universität Dortmund, Maria-Goeppert-Mayer-Str. 2, D-44221 Dortmund

* corresponding author: philipp.weinert@tu-dortmund.de

Graphene is characterized by its outstanding mechanical, electronic, and magnetic properties. Consequently, it was found to be a promising candidate for electronic and spintronic devices, which can be realized by multilayer systems consisting of graphene and different metals. For example, a graphene-ferromagnet interfaces possess remarkable properties like induced magnetism in the graphene film, increased magnetic anisotropy in the ferromagnetic film, and chiral magnetism.

In this research the chemical bindings in a graphene/cobalt/platinum system on a silicon carbide (SiC) substrate are investigated by means of XPS. In advance, the system has been investigated by means of LEED and PEEM to determine the preparation parameters. Furthermore, its magnetic properties will be determined by means of X-PEEM and XMCD. Due to the magnetic exchange interaction at the interfaces, perpendicular magnetic anisotropy (PMA) exists in the Co film of both the G/Co and the Co/Pt system [1, 2]. For this reason, it is most likely that also the Co film in the combined G/Co/Pt system shows PMA. However, in a G/Co system on SiC no PMA was found [3]. This finding can be explained by the formation of cobalt silicides, which are strongly suspected to weaken the PMA. The added Pt layer between the Co and the SiC serves to prevent this formation. Moreover, the PMA in the Co layer will be strengthened by combining it with a heavy non-magnetic metal, such as Pt.

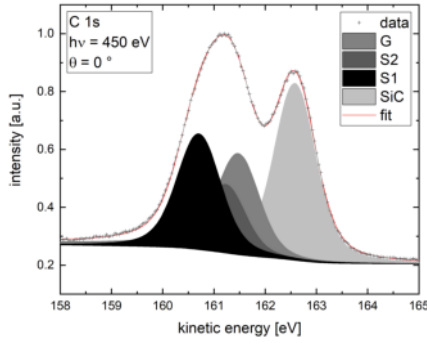
Sample preparation can be divided into three steps. After each step the sample was investigated by means of XPS.

First, the $(6\sqrt{3} \times 6\sqrt{3})R30^\circ$ surface reconstruction of SiC (buffer layer) has been grown homogeneously on SiC over large areas [4]. This surface serves as a precursor for monolayer graphene formation upon intercalation. Figure 1a shows the XPS spectra of the C1 s signal of the sample in this state. The preparation method causes small strips of monolayer graphene on top of the buffer layer at the step edges of the SiC. The corresponding component (G) is located between the buffer layer components (S1 and S2) and the substrate component (SiC) [5].

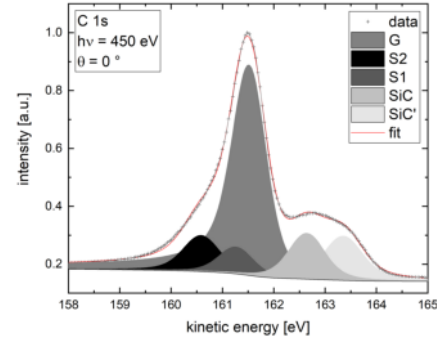
By intercalating Pt the bonds between the buffer layer and the SiC are released. This way the buffer layer becomes quasi free standing graphene [6]. Consequently, in the corresponding XPS spectrum, which is shown in figure 1b the buffer layer components shrunk, while the graphene component growth. That the buffer layer components did not vanish completely, indicates that a part of the buffer layer still is bonded to the substrate. These finding shows that the thickness of the Pt layer, which is 0.7 \AA was to low to saturate all bond of the substrate surface. In future investigations the amount of Pt will be increased slightly to fully release the buffer layer. Noteworthy, the corresponding Pt 4f signal, shown in figure 2 consists of four components. Three of them belong to Pt-Si compounds, which might indicate that the Pt saturate the free silicon bonds.

The last step of the preparation, the deposition and intercalation of Co should not cause any chemical changes, which is why none of the XPS spectra taken after this step has shown any change in shape. Especially no Co-Si components have formed. To prove the intercalation, ARXPS has been used. The corresponding results are shown in figure 3.

In summary, the desired prevention of Co-Si components has been achieved and the necessary thickness of the Pt layer has been determined. Future measurements will focus on the magnetic properties of the system and hopefully will show strong PMA in the Co layer.



(a) XPS spectrum of the carbon 1s signal of buffer layer and small amounts of monolayer graphene grown on silicon carbide.



(b) XPS spectrum of the carbon 1s signal of monolayer graphene on silicon carbide after the intercalation of 0.7 Å Pt. Small buffer layer components remain.

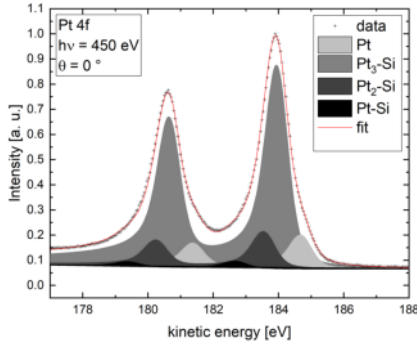


Figure 2: XPS spectrum of the platinum 4f signal of a Pt layer intercalated between G and SiC. Three silicide components are present, what indicates that the Pt saturate the free silicon bonds.

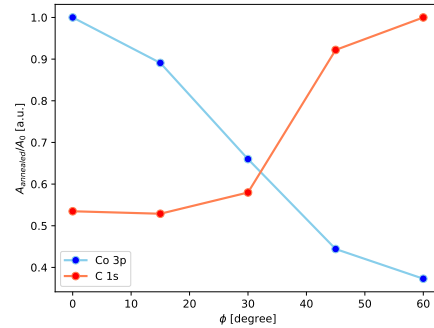


Figure 3: Ratios of the XPS intensities after and before annealing of Co and G as a function of polar angle. Their progression prove the Co interaction.

Acknowledgement

We would like to thank the DELTA-staff for their great support.

References

- [1] G. S. Grebenyuka et al., Phys. Solid State **61**, 7 (2019).
- [2] C. Xia et al., Carbon **79**, 1 (2014).
- [3] R. Hönig et al., Nanotechnology **30**, 2 (2019).
- [4] W. A. de Heer et al., Proc. Natl. Acad. Sci. USA **108**, 16900 (2011).
- [5] C. Riedl et al., J. Phys. D: Appl. Phys. **43**, 37 (2010).
- [6] S. Forti et al., Phys. Rev. B **84**, 125449 (2011).

X-ray Scattering

Influence of Nitrogen content on the oxidation resistance of PECVD Ti-Si-B-C-N nanocomposite coatings

Nienhaus, A.¹; Paschke, H.²; Sternemann, C.³; Paulus, M.³

IOT TU Braunschweig, 44145 Dortmund, Germany

Fraunhofer Institute for Surface Engineering and Thin Films IST, Dortmund 44145, Germany

Fakultät Physik/DELTA, Technische Universität Dortmund, 44221 Dortmund, Germany

In recent years, nanocomposite PVD (physical vapour deposition) and PECVD (Plasma-enhanced chemical vapor deposition) coatings were deposited on tools used in hot forging applications due to their promising properties concerning wear reduction. In addition to mechanical properties, e.g. high hardness values, low coefficient of friction, etc., the oxidation resistance is a key factor for surfaces in hot forming applications.

The nanocomposite structure consists of nanocrystalline (nc-) grains embedded in an amorphous (a-) matrix. The group of coatings containing some or all of the elements Ti, Si, B, C, and N has been studied by many authors over the years. The oxidation behavior has been analyzed by Chen et al. [CHE12] for Ti-B-C-N, Kiryukhantsev-Korneev et al. [KIR07] for Ti-B-N and Ti-Si-B-N, Mahato et al. [MAH16] for Ti-Si-B-C, and Pilloud et al. [PIL08] for Ti-Si-N. All these works used X-ray diffraction (XRD) after annealing in air atmosphere to detect oxide phases, e.g. TiO₂. The TiO₂ grains are bigger than Ti(C,N) grains, as it is noted by all the authors above. Pilloud et al. [PIL08] found, a TiO₂ grain size of 40 nm with short annealing durations (2 h, 700 °C), while Mahato et al. [MAH16] showed, that extensive annealing (100 h, 800 °C) leads to grain sizes of up to 1,000 nm. This leads to the conclusion, that annealing duration, annealing temperature, and coating material have an impact on oxidation behavior and can be characterized by grain size. The mentioned works focused on XRD measurements after annealing in air, while in this work, XRD is carried out in-situ at elevated temperatures at Beamline BL9 of the synchrotron light source DELTA (TU Dortmund, Dortmund, Germany [KRY06]). To evaluate the oxidation behavior, it was analyzed how the characteristic reflections of Ti(C,N) and TiO₂ were pronounced and the grain sizes were determined under use of the Scherrer equation. Five coating systems with N₂ flow rates of 0-667 sccm, leading to varying N₂ contents, were investigated and compared (see table 1).

Table 1: Chemical composition and grain sizes of Ti-Si-B-C-N coatings.

| N ₂ flow rate [sccm] | N [at.-%] | Grain size [nm] | | | Impurities [at.-%] | |
|---------------------------------|-----------|-----------------|-----------|------------------|--------------------|-----|
| | | TiC | TiN | TiO ₂ | O | Cl |
| 0 | 0 | 4.9 ± 0.1 | - | 21.4 ± 2.5 | 2.2 | 2.1 |
| 167 | 4.4 | | 6.1 ± 1.0 | 12.4 ± 2.4 | 1.4 | 2.3 |
| 333 | 8.7 | | 6.0 ± 0.5 | 19.2 ± 0.2 | 1.5 | 2.7 |
| 500 | 12.9 | | 5.4 ± 0.9 | | 1.8 | 3.0 |
| 667 | 14.6 | | 5.3 ± 1.1 | 8.3 ± 0.6 | 3.4 | 3.5 |

Results

Figure 1 shows the XRD data of the coatings at 875 °C in air atmosphere. It is notable, that, in all cases, the Ti(C,N) (2 0 0) reflection (42° in 2θ) is orders of magnitude larger than the TiO₂ reflections (see vertical lines in figure 1). This can be explained due to surface-near oxidation with an intact nanocomposite, oxygen free material underneath. The coating with 12.9 at.-% shows a strong Ti(C,N) reflection at 42° and hardly any TiO₂ reflections.

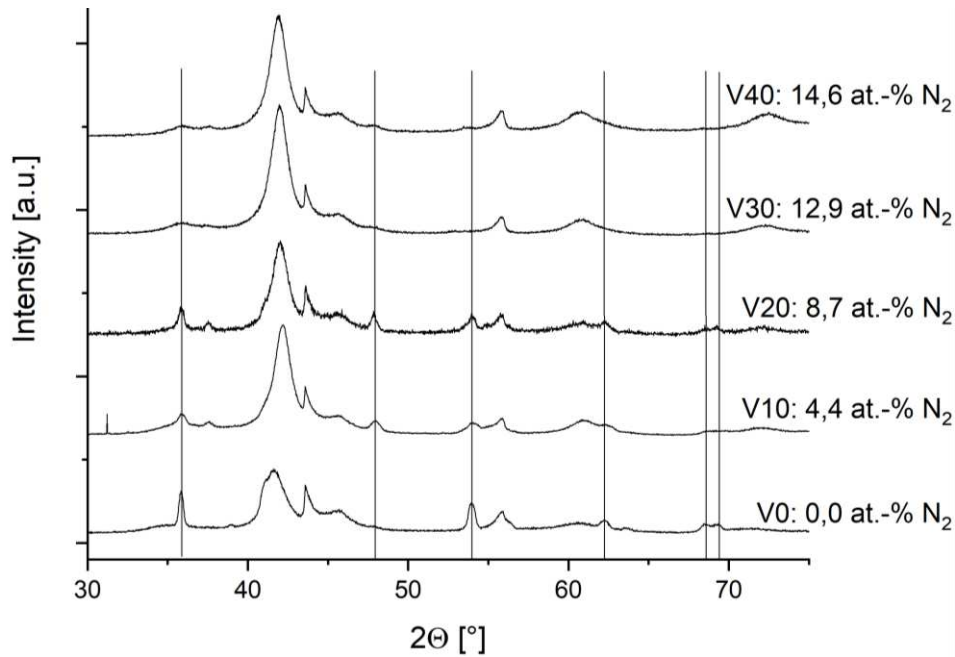


Figure 1: XRD results at 875 °C for Ti-Si-B-C-N coatings with varying N content. The vertical lines mark positions of characteristic reflexes of TiO_2 and the reflexes at 44°, 56°, and 61° 2θ result from experimental setup.

The as deposited grain sizes of nc-TiN and nc-TiC range between 4-7 nm in all coatings. These results comply with comparable XRD measurements in a different laboratory on similar coatings that were deposited in the same furnace, with grain sizes determined to 4-7 nm, too. The grain sizes of the same coatings at elevated temperatures are given in table 1. These grains are protected from oxidation by the a-matrix and are thermally stable, because no increase in grain size could be detected. This is not always given, because - depending on the deposition conditions - coatings with unstable nanocomposites with low thermal stability are possible. In that case, vacuum annealing of Ti-B-N above 800 °C leads to grain growth from 2-3 nm (as deposited) to 4, 7, and 9 nm with $T_a = 900$ °C, 1000 °C, and 1100 °C, respectively [MAY06]. The TiO_2 grain sizes show the oxidation resistance in dependence of the N content. While the grain size of the N-free system and the one with 8.7 at.-% are about 20 nm, it is 12 nm for 4.4 at.-%. The comparison with the 12.9 at.-% N coating shows a significant contrast to the coating systems with N < 10 at.-%. The TiO_2 reflexes were so small, that calculations of grain sizes would be unreasonable and accompanied by a large margin of error. The coating system with 14.6 at.-% N shows oxidation and the TiO_2 grain sizes were determined to 8 nm. On the one hand, this coating system has a similar nitrogen content as the one with 12.9 at.-%N, hinting on a high oxidation resistance, but on the other hand, the coating's impurities are significantly higher with O and Cl contents of 3.4 at.-% and 3.5 at.-% respectively, compared to 1.8 at.-% and 3.0 at.-%, respectively.

Conclusions

High-resolution in-situ XRD at BL9 of DELTA, TU Dortmund at elevated temperatures allows to investigate the structure of the sample systems, calculating the derivable grain sizes and compare the results with each other and other authors' work to find the influence of N content in Ti-Si-B-C-N nanocomposite coatings.

- Ti-Si-B-C-N coating's N content shows a considerable impact on oxidation resistance.
- The oxidation resistance primarily depends on the N content, and secondarily on O and Cl impurities due to the PECVD deposition process.
- Assuming low impurities (<2.5 at.-% O and < 3.5 at.-% Cl) a nitrogen content of >10 at.-% N seems to increase oxidation resistance remarkably.

- The grain growth within the nanocomposite coating during oxidation corresponds with the observations and hypotheses of other authors on comparable coating systems.

Acknowledgment

We kindly acknowledge the support of the DELTA machine group and the provided synchrotron radiation. Contribution of EPMA measurements for identification of the chemical composition and comparative XRD measurements by Ms. Steinberg and Dr. Schiffmann (Fraunhofer Institute for Surface Engineering and Thin Films IST) are also greatly appreciated.

Literature

- [CHE12] Chen, Xiangyang; Ma, Shengli; Xu, Kewei; Chu, Paul K. (2012): Oxidation behavior of Ti-B-C-N coatings deposited by reactive magnetron sputtering. In: *Vacuum* 86 (10), S. 1505–1512. DOI: 10.1016/j.vacuum.2012.03.001.
- [KIR07] Kiryukhantsev-Korneev, Ph.V.; Shtansky, D. V.; Petrzhik, M. I.; Levashov, E. A.; Mavrin, B. N. (2007): Thermal stability and oxidation resistance of Ti–B–N, Ti–Cr–B–N, Ti–Si–B–N and Ti–Al–Si–B–N films. In: *Surface and Coatings Technology* 201 (13), S. 6143–6147. DOI: 10.1016/j.surfcoat.2006.08.133.
- [MAH16] Mahato, P.; Singh, R. J.; Mishra, S. K. (2016): Nanocomposite Ti–Si–B–C hard coatings deposited by magnetron sputtering: Oxidation and mechanical behaviour with temperature and duration of oxidation. In: *Surface & Coatings Technology* (288), S. 230–240.
- [MAY06] Mayrhofer, P. H.; Mitterer, C.; Greene, J. E. (2006): Thermally induced self-hardening of nanocrystalline Ti-B-N thin films. In: *Journal of Applied Physics* (100).
- [PIL08] Pilloud, D.; Pierson, J. F.; Marco de Lucas, M. C.; Cavaleiro, A. (2008): Study of the structural changes induced by air oxidation in Ti–Si–N hard coatings. In: *Surface and Coatings Technology* 202 (11), S. 2413–2417. DOI: 10.1016/j.surfcoat.2007.09.017.
- [KRY06] Krywka, C; Paulus, M; Sternemann, C; Volmer, M; Remhof, A; Nowak, G; Nefedov, A; Pöter, B; Spiegel, M and Tolan (2006), M; The new diffractometer for surface x-ray diffraction at beamline BL9 of DELTA, *J. Synchrotron Rad.* 13, 8.

Influence of the Deposition Technology on the Crystalline Structure of TiAlN PVD Coatings

Wolfgang Tillmann¹, Dominic Stangier^{1*}, Diego Grisales¹, David Kokalj¹,
Leif Hagen¹, Jan Latarius², Christian Sternemann², Michael Paulus²

¹Institute of Materials Engineering, TU Dortmund University, Germany
44227 Dortmund, Leonhard-Euler-Straße 2

²Experimental Physics 1 / DELTA, TU Dortmund University, Germany
44227 Dortmund, Maria-Goeppert-Mayer-Straße 2

* corresponding author: dominic.stangier@tu-dortmund.de

The deposition of PVD coatings synthesized by high power impulse magnetron sputtering (HiPIMS) has recently gained enormous interest due to the possibilities of providing unique properties in terms of mechanical properties and crystalline growth of thin films [1],[2]. However, thin films deposited by this technology must be critically examined with regard to their residual stresses under mechanical and tribological loads to provide sufficient wear-resistance for production engineering processes [3],[4]. Due to the increased ionization rate of the sputtered material in terms of Ti^+ or Ti^{2+} high compressive residual stresses are induced in Ti-based nitride PVD coatings [5], which can have a negative effect on the adhesion of the substrate coating compound [6],[7]. In addition, the low deposition rates due to the pulsed capacitor discharge reduce the economic efficiency of these processes. To meet these challenges, hybrid coating processes consisting of a superposition of the short high-energetic pulses and DC cathode sputtering represent a promising approach to overcome these challenges [8]. This process combines a reduced deposition time with a high ionization rate due to the superposition of the HiPIMS pulses with the constant power of the DC source [9]. In this context, there can be found only little information about the crystalline structure and texturing of differently deposited TiAlN coatings. For this reason, the investigation of three different TiAlN coatings processed by DC, HiPIMS and a hybrid process (DC/HiPIMS) were deposited in the same coating device and were examined with respect to their crystalline structure. A more detailed description of the used substrate material, magnetron-sputtering device and thermo kinetic deposition parameters as well as the resulting mechanical properties are presented in detail in previous investigations of the authors [10].

The phase analysis of the 3 μm thick TiAlN coatings was conducted using a photon energy of $E = 20 \text{ keV}$ with a corresponding wavelength of $\lambda = 0.619921 \text{ \AA}$. The experiments were conducted using a low angle of incidence ($\omega = 1^\circ$) with an exposure time of 300 s in reflection mode to reduce the intensity of the substrate reflexes. To analyze the influence of the deposition technology on the orientation and the texture of thin films, the coatings were investigated by means of 2D grazing incidence XRD (GI-XRD) using an image plate detector MAR345. As reference Si powder was used and the evaluation of the patterns was conducted using fit2d calibrating the sample to detector distance and the center of the beam. The beam size was set to a height of 0.05 mm and a width of 1 mm.

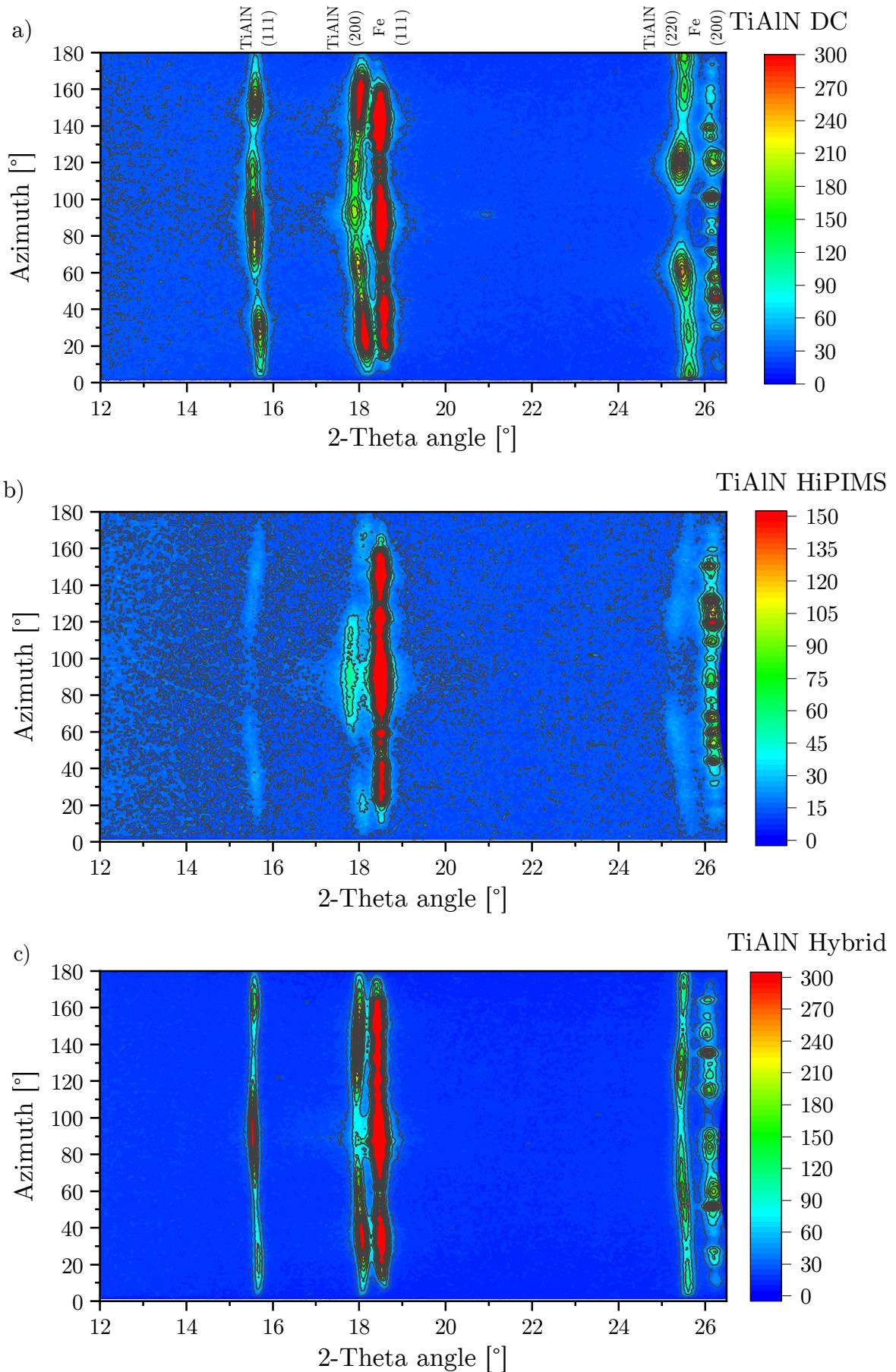


Figure 1: 2D-GIXRD measurements of TiAlN coatings ($\lambda = 0.619921 \text{ \AA}$) with an angle of incidence of $\omega = 1^\circ$, a) DC, b) HiPIMS and c) Hybrid (DC/HiPIMS)

The results of the XRD measurements of the three coating systems are summarized in Figure 1. The obtained patterns prove, that the TiAlN only differs in their crystalline orientation and not in their phase composition. The measured small process-related fluctuations on the stoichiometry of the thin films have therefore no influence on the phase formation. Furthermore, the presence of a crystalline hexagonal AlN phase can be excluded from the results, so that the thin films consist exclusively of the NaCl structure (fcc) of the TiN phase. Consequently, the maximum solubility limit of aluminum in the crystal lattice of TiN was not exceeded. The reflexes located at $2\Theta = 18.5^\circ$ and $2\Theta = 26.5^\circ$ can be ascribed to the α -Phase of iron (111) and (200), which is attributed to the tool steel substrate material in combination with the high energy of the x-rays. This explains why a similar characteristic of the reflex is observed for the three different PVD coating systems. However, within the TiAlN thin films differences in the orientation and texture are clearly visible. Cubic phases synthesized by DC sputtering grow in the thermodynamically favored (111) growth direction ($2\Theta = 15.5^\circ$) [11], which is in good agreement with the TiAlN layers synthesized in the investigations. Additionally, a highly textured (200) and (220) orientation ($2\Theta = 18.0^\circ$ and $2\Theta = 25.5^\circ$) for the coating can be observed as well. Comparing these findings to the results of the HiPIMS coating it becomes obvious, that with an increasing kinetic energy as it is provided by the higher ionization of the HiPIMS process the crystalline orientation changes to the (200) direction. This can be explained by the higher adatom mobility during the film growth, which tries to reach a minimum of the free surface energy and therefore favorably stabilizes the (200) orientation [12],[13]. These findings are accompanied by a shift of the reflection position depending on the azimuth angle, which can be observed for the (111) and (220) growth direction. This effect is an indicator for the high residual stresses in HiPIMS coatings. With respect to the crystalline structure the results of the hybrid process show the combination of the before mentioned patterns. Similar observations were made by Luo et al for TiN coatings deposited by a DC/HiPIMS process, showing an increase in the (220) orientation [14], which is also observed for the TiAlN coatings within this study.

To gain a deeper understanding of the involved mechanisms of the occurring texture and thin film growth, the plasma properties during the deposition process must be taken under consideration and directly correlated with the results of x-ray diffraction. Furthermore, the resulting phase specific residual stresses as well as the integral stresses in the coating system should be examined to understand the performance of the TiAlN coating in real production processes and tribological applications.

Acknowledgements

The authors gratefully acknowledge the DELTA machine group for providing synchrotron radiation and their support at BL9.

References

- [1] A. Anders, *Surface & Coatings Technology* 257 (2014) 308–325.
- [2] W.-D. Münz, M. Schenkel, S. Kunkel, J. Paulitsch, K. Bewilogua, *Journal of Physics: Conference Series* 100 (2008) 82001, S. 1-6.

- [3] G. Skordaris, K.D. Bouzakis, T. Kotsanis, P. Charalampous, E. Bouzakis, B. Breidenstein, B. Bergmann, B. Denkena, *CIRP Journal of Manufacturing Science and Technology* 18 (2017) 145–151.
- [4] K. Ait Aissa, A. Achour, J. Camus, L. Le Brizoual, P.-Y. Jouan, M.-A. Djouadi, *Thin Solid Films* 550 (2014) 264–267.
- [5] G. Greczynski, J. Lu, M. Johansson, J. Jensen, I. Petrov, J.E. Greene, L. Hultman, *Vacuum* 86 (2012) 1036–1040.
- [6] A. Guillaumot, F. Lapostolle, C. Langlade, A. Billard, J.C. Oliveira, A. Cavaleiro, C. Dublanche-Tixier, *IEEE Transactions on Plasma Science* 38 (2010) 3040–3045.
- [7] B. Breidenstein, B. Denkena, *CIRP Annals - Manufacturing Technology* 62 (2013) 67–70.
- [8] G. Greczynski, J. Lu, M.P. Johansson, J. Jensen, I. Petrov, J.E. Greene, L. Hultman, *Surface & Coatings Technology* 206 (2012) 4202–4211.
- [9] S. Severin, M. Naveed, S. Weiß, *Advances in Materials Science and Engineering* 2017 (2017) 1–18.
- [10] W. Tillmann, D. Grisales, D. Stangier, I. Ben Jebara, H. Kang, *Surface and Coatings Technology* 378 (2019) 125075.
- [11] Q. Luo, D.B. Lewis, P.E. Hovsepian, W.-D. Münz, *Journal of Materials Research* 19 (2004) 1093–1104.
- [12] J. Paulitsch, P.H. Mayrhofer, W.-D. Münz, M. Schenkel, *Thin Solid Films* 517 (2008) 1239–1244.
- [13] H. Elmkhah, T.F. Zhang, A. Abdollah-zadeh, K.H. Kim, F. Mahboubi, *Journal of Alloys and Compounds* 688 (2016) 820–827.
- [14] Q. Luo, S. Yang, K.E. Cooke, *Surface & Coatings Technology* 236 (2013) 13–21.

X-ray diffraction study on cold sprayed Babbitt coatings

Wolfgang Tillmann¹, Michael Paulus², Leif Hagen^{1*}, David Kokalj¹,
Dominic Stangier¹, Mohamed Abdulgader¹

¹Institute of Materials Engineering, TU Dortmund University, Germany
44227 Dortmund, Leonhard-Euler-Straße 2

*corresponding author: leif.hagen@tu-dortmund.de

²Experimental Physics 1 / DELTA, TU Dortmund University, Germany
44227 Dortmund, Maria-Goeppert-Mayer-Straße 2

Babbitt, also called white metal, represents a group of alloys that contain different grades based on Sn or Pb, with the addition of Cu and Sb. The microstructure of Sn-Sb-Cu-based Babbitt alloys mainly consists of a soft solid solution matrix interstratified with intermetallic phases such as SbSn and Cu₆Sn₅ [1]. The formation of Cu₆Sn₅ results from the interaction of Cu with liquid Sn. Other structures like Cu₃Sn might arise from decomposition of Cu₆Sn₅ under high temperatures and Cu excess [2]. Reaching 186°C, Cu₆Sn₅ shows a phase transition from a monoclinic crystal structure to a hexagonal crystal structure [3]. However, this hexagonal phase can be stabilized also at room temperature by the addition of small amounts of Sb yielding the formation of Cu₆Sn_{5-x}Sb_x.

Babbitt coatings are widely used in industrial bearings; they serve as a sacrificial surface. In the event of unwanted contact between sliding surfaces, the softer Babbitt surface wears out to protect the more expensive counterpart from significant damage, or to permit deformation to accommodate some misalignment of the bearing surfaces. Babbitt coatings are commonly deposited by means of flame spraying, plasma spraying, high velocity oxy-fuel spraying or arc spraying. To date, only a very few studies have paid attention to Sn-Sb-Cu-based Babbitt coatings deposited by means of low pressure cold spraying (LPCS). Among thermal spraying, LPCS represents a cost-saving method without the usage of fuel gases or liquid fuels, with the ability to recondition or repair coatings of worn surfaces, even on site, directly on the customer's premises as the spray equipment is transportable. LPCS is characterized by low process temperatures with high spray particle velocities. The temperature of the propellant gas is typically below the melting point of the feedstock. Thus, the temperature of the propellant gas (e.g. air) is commonly up to 650 C, with the working temperature range for low-melting materials usually being in the range of 300 to 500 C. The propellant gas is accelerated to supersonic velocities in a de Laval-type nozzle. The feedstock is injected in the diverging part of the nozzle from where spray particles are accelerated towards the substrate. Here, the spray particle velocities are usually in the range of 350 to 700 m/s. The spray particles impinge on the substrate with high kinetic energy, deform and generate the coating.

In this study, Sn-Sb-Cu-based coatings produced by LPCS using different preheating gas temperatures (PGT, i.e. temperature of the propellant gas) and substrate preheating temperatures (ST) were investigated with respect to their microstructural characteristics. Coin-shaped (40 mm × 5 mm) AISI 1045 steel specimens served as substrates. Prior to the coating

deposition, the substrates were grit blasted using corundum with a grit size of F100. The coatings were produced with the use of oil-free compressed air and a DYMET 413 spraying system (Dycomet, The Netherlands). The PGT, as well as the ST, were varied between 300°C and 400°C as well as between 20°C and 260°C. The phase composition, mesoscopic structure such as the distribution of intermetallic compounds, as well as mechanical properties (i.e. microhardness, coating adhesion) were analysed depending on different PGT and ST. In the following, only the findings obtained from the X-ray diffraction analysis on the coating surfaces are presented. For full information including coating preparation and analytic methods, see [4]. The X-ray diffraction experiments were conducted at the beamline BL9 of DELTA. The energy of the photon beam was set to 15 keV (wavelength $\lambda=0.8265 \text{ \AA}$). A PILATUS100k detector system was used to measure the scattered intensity. The beam size was $1.5 \times 0.1 \text{ mm}^2$ (horizontal \times vertical) while the angle of the incidence was set to 5° . In order to analyze the phase composition, the software MATCH! in conjunction with a reference database (i.e. Crystallography Open Database) was used. Selected XRD patterns of the samples and feedstock are shown in Figure 1.

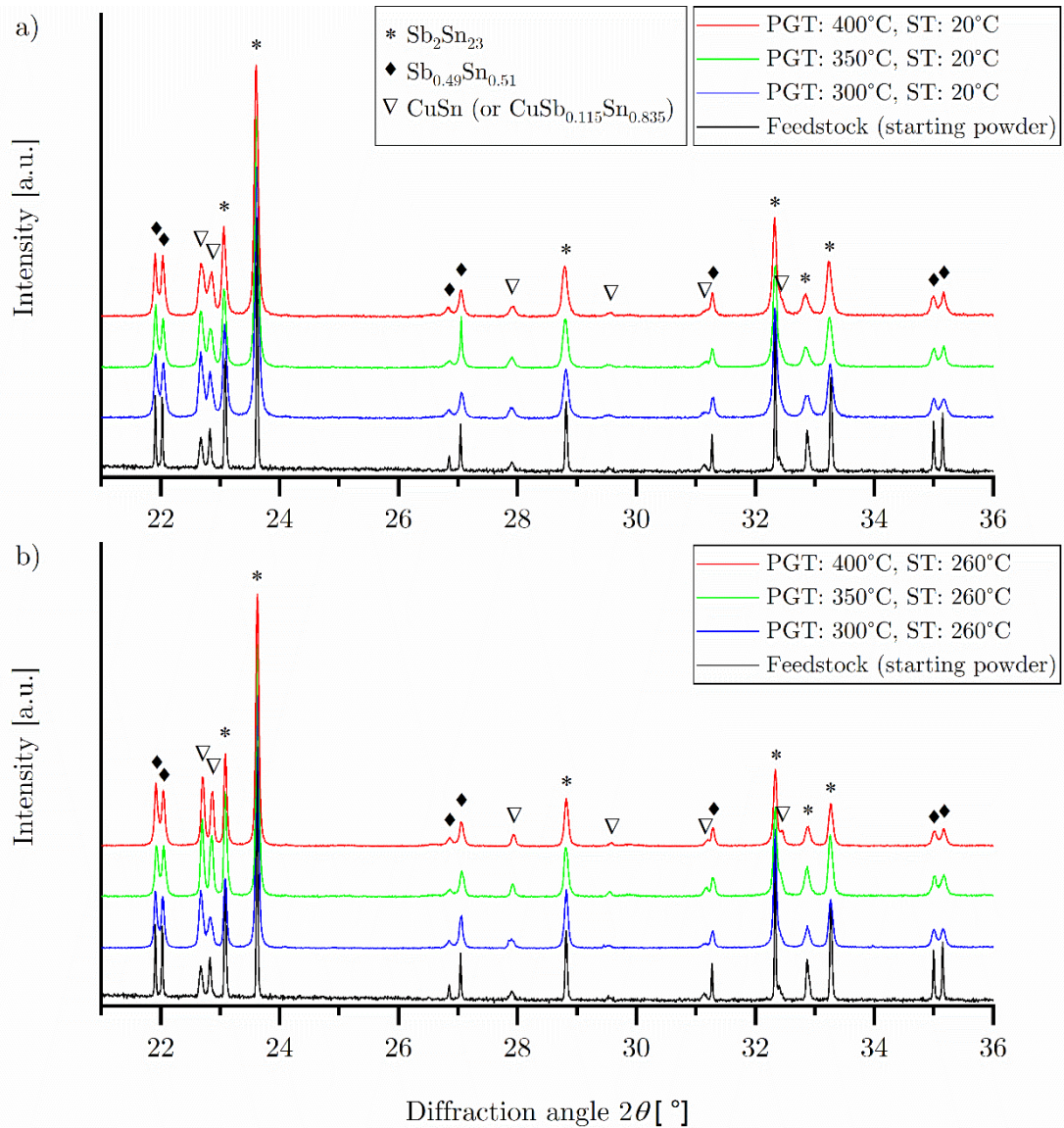


Figure 1: XRD patterns as obtained from coatings produced with the use of different PGT: (a) deposited on a ST of 20°C; and (b) deposited on a ST of 260°C.

The coatings either produced by using different PGT or ST and the feedstock consist of $\text{Sb}_2\text{Sn}_{23}$, $\text{Sb}_{0.49}\text{Sn}_{0.51}$ and Sorosite (CuSn or $\text{CuSb}_{0.115}\text{Sn}_{0.835}$). There was no evidence for the formation of Cu_3Sn and monoclinic Cu_6Sn_5 within the experimental resolution. In comparison with the feedstock, no phase transformation due to the coating deposition could be identified. Nevertheless, metallographical investigations indicated a more homogeneous distribution of $\text{Sb}_{0.49}\text{Sn}_{0.51}$ dispersed in a soft Sn-rich solid solution matrix for samples produced at elevated PGP, leading to an increase in microhardness. For further information, see [4].

Acknowledgements

The authors gratefully acknowledge the DELTA machine group for providing synchrotron radiation and their support at BL9.

References

- [1] M. Kamal, A. Abdel-Salam, J.C. Pieri, Modification in tin-antimony alloys, *J. Mater. Sci.* 19, (1984) 3880–3886.
<http://dx.doi.org/10.1007/BF00980751>
- [2] Q. Yin, F. Gao, Z. Gu, E.A. Stach, G. Zhou, In situ visualization of metallurgical reactions in nanoscaleCu/Sn diffusion couples, *Nanoscale* 7, (2015) 4984–4994.
<http://dx.doi.org/10.1039/C4NR06757F>
- [3] C.Y. Yu, J.G. Duh, Stabilization of hexagonal $\text{Cu}_6(\text{Sn,Zn})_5$ by minor Zn doping of Sn-based solder joints, *Scr. Mater.* 65, (2011) 783–786.
<http://dx.doi.org/10.1016/j.scriptamat.2011.07.029>
- [4] W. Tillmann, L. Hagen, M. Abdulgader, M. D. Kesy, M. Paulus, Microstructural Characteristics in Babbitt Coatings Deposited by LPCS, *Coatings* 10, (2020) 689.
<http://dx.doi.org/10.3390/coatings10070689>

Structural analysis of LBM 316L substrate PVD CrAlN coating composites

Wolfgang Tillmann, Leif Hagen^{*}, Dominic Stangier, David Kokalj, Nelson Filipe
Lopes Dias, Dennis Kensy

Institute of Materials Engineering, TU Dortmund University, Germany

44227 Dortmund, Leonhard-Euler-Straße 2

^{*} corresponding author: leif.hagen@tu-dortmund.de

Laser beam melting (LBM) evolved into a common process in the field of additive manufacturing such as rapid prototyping, rapid manufacturing, or rapid tooling [1]. Due to the inherent process characteristics, the produced samples still exhibit a residual porosity and high surface roughness [2]. The microstructural characteristics (e.g. grain orientation), among others, depend on the thermal history during processing, which in turn is associated with the building strategy [3]. 316L stainless steel provides outstanding mechanical properties as well as good corrosion resistance [4]. Accordingly, the material is mainly used in the oil and gas industry, chemical industry, the aerospace and automotive industries, as well as for surgical instruments. Additionally, 316L has a good weldability and therefore ideally suited for additive manufacturing [5]. The microstructural characteristics of 316L parts, produced by LBM, differs from those obtained from bulk materials [6]. 316L parts processed by LBM are commonly characterized by a fine-grained, irregular microstructure with grains arranged along the building direction. Most steel components for industrial applications produced by LBM are intended for the usage under high mechanical, thermal, or corrosive loads. Physical vapor deposition (PVD) hard coatings such as ternary nitride coatings (e.g. TiAlN [7], ZrAlN [8] or CrAlN [9]) already demonstrated great potential to protect tribologically stressed steel surfaces against wear. Due to their high oxidation resistance and high hardness, CrAlN coatings permit use at high temperatures with outstanding resistance against abrasion [10]. The increased hardness can be attributed to solid solution hardening effects as a result of Al incorporation. For depositing thin films such as PVD hard coatings, a smooth substrate surface finishing is among others required in order to enable an appropriate coating growth and a reduced risk of coating defects [11, 12]. As mentioned previously, the initial surface of LBM samples (i.e. as-built state) does not provide the required specifications, due to their existing roughness and pores. To reduce surface asperities and surface defects, different pre-treatment procedures such as polishing or lapping must be therefore applied.

Although 316L stainless steel is among the most investigated material for LBM, the deposition of PVD hard coatings such as ternary nitride coatings onto 316L substrates including their microstructural evolution has not been studied yet. This study aims at evaluating the effect of commonly used mechanical pre-treatments onto 316L stainless steel substrates processed by LBM and their effect on the microstructural evolution of PVD CrAlN coatings. Therefore, a 316L austenitic stainless-steel (1.4404) additive manufactured sample (AM) served as substrate. The additive manufactured sample was produced by LBM and provided by the Chair of Materials Science (Paderborn University, Germany). The LBM process parameter can be found elsewhere [13]. A 316L austenitic stainless-steel bulk material (BM) served as reference

substrate. Prior to the coating deposition, the different substrates were subjected to two different mechanical pre-treatments (Table 1): (i) grinding and polishing, and (ii) grinding and lapping.

Table 1: Summary of the different pre-treatment procedures

| | Grit size [μm] | Revolutions [1/min] | Force [N] | Duration [min] |
|------------------|-----------------------------|---------------------|-----------|----------------|
| Grinding | F1200* | 300 | 20 | 3 |
| | F2500* | 300 | 20 | 1 |
| Polishing | 3 | 150 | 15 | 3 |
| | 1 | 150 | 5 | 5 |
| Lapping | 9 | 150 | 20 | 6 |

*according to the Federation of European Producers of Abrasives (FEPA)

As verified by confocal 3D microscopy, the lapped LBM 316L substrate (AM_lap) shows an arithmetical mean height Sa of the surface of $0.065 \pm 0.021 \mu\text{m}$ (with a maximum height Sz of the surface of $1.410 \pm 0.010 \mu\text{m}$), whereas the polished LBM 316L substrate (AM_pol) exhibits a Sa of $0.306 \pm 0.110 \mu\text{m}$ ($Sz = 1.570 \pm 0.020 \mu\text{m}$). In contrast, the polished 316L bulk material substrate (BM_pol) demonstrates a Sa of $0.017 \pm 0.001 \mu\text{m}$, as well as a Sz of $1.305 \pm 0.005 \mu\text{m}$. The lapped 316L bulk material substrate (BM_lap) features a Sa of $0.038 \pm 0.002 \mu\text{m}$, and Sz of $3.975 \pm 0.050 \mu\text{m}$, respectively.

The deposition of the CrAlN coating was carried out by means of a reactive sputtering process using an industrial magnetron sputtering device CC800/9 Custom (CemeCon AG, Germany). The sequence of the pre-treatments as well as the deposition parameters are given elsewhere [14]. The phase composition was investigated by means of 2D grazing incidence X-ray diffraction at the beamline BL9 of the synchrotron light source DELTA (TU Dortmund University, Germany) using an image plate detector MAR345 (marXperts GmbH, Germany). The photon energy was set to 20 keV (wavelength of $\lambda = 0.6199 \text{ \AA}$). To investigate the different regions of interest, the CrAlN coating and stainless steel substrate, two different angles of incidence were used. To analyse the coating, the angle of incidence was set to 1° , whereas for a more detailed investigation of the substrate the angle of incidence was adjusted to 3° .

As shown by XRD analyses (Figure 1), both the 316L bulk material substrate and the LBM substrate are mainly composed of a face-centered cubic, austenitic phase (γ -phase) as indicated by the Debye-Scherrer rings Scherrer rings at $\theta = 17.19^\circ$ (111), $\theta = 19.84^\circ$ (200), $\theta = 28.22^\circ$ (220), $\theta = 33.20^\circ$ (311) and $\theta = 34.74^\circ$ (222). Additionally, the BM samples exhibit traces of a ferritic phase (α -Fe).

The two-dimensional diffraction patterns of the CrAlN coatings show the presence of Debye-Scherrer rings at $\theta = 14.95^\circ$ (111), $\theta = 17.27^\circ$ (200) $\theta = 24.59^\circ$ (220), $\theta = 28,76^\circ$ (311), $\theta = 30.06^\circ$ (222) and $\theta = 34.89^\circ$ (400), which can be assigned to a face-centered cubic structure (Figure 2). Analysing the two-dimensional diffraction pattern of sample AM_lap and BM_pol, indicates a small amount of hexagonal AlN at $\theta = 13.20^\circ$ and $\theta = 22.97^\circ$. The presence of hexagonal close packed CrAlN indicates the exceeding of the solid solution limits of Al in the face-centered cubic CrN phase. This effect can be caused by spinodal decomposition induced by residual stresses in the coating as it was observed by Zauner et al. [15]. The absence of texture for hexagonal CrAlN is an additional indicator that the phase is not formed within

PVD coating growth. Moreover, the CrAlN coatings deposited on AM_lap, AM_pol as well as BM_lap show a symmetric grain orientation in (220) direction; to be precise at an azimuth of $\Phi = 45^\circ$, $\Phi = 90^\circ$ and $\Phi = 135^\circ$. In addition, all samples demonstrate a symmetric grain orientation in (200) direction at an azimuth of $\Phi = 45^\circ$ and $\Phi = 135^\circ$. In this regards, all samples were manufactured during the same process, indicating to the fact that the texture must be related to the substrate condition.

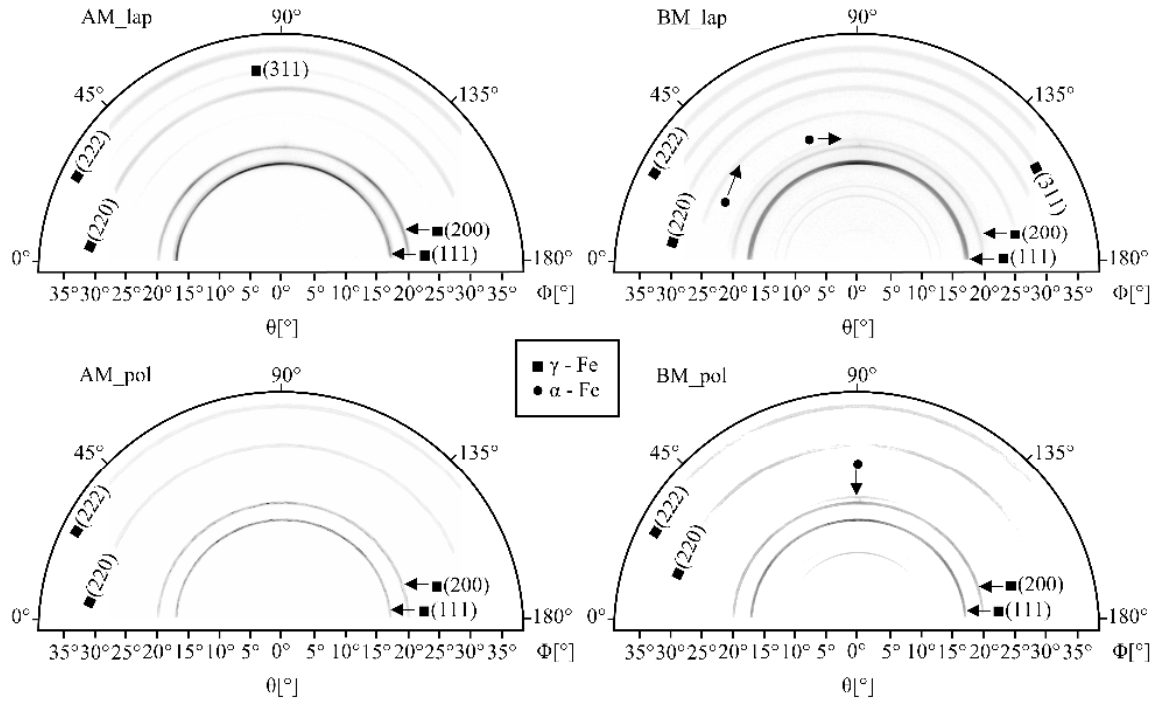


Figure 1: Two-dimensional XRD patterns of the different 316L substrates

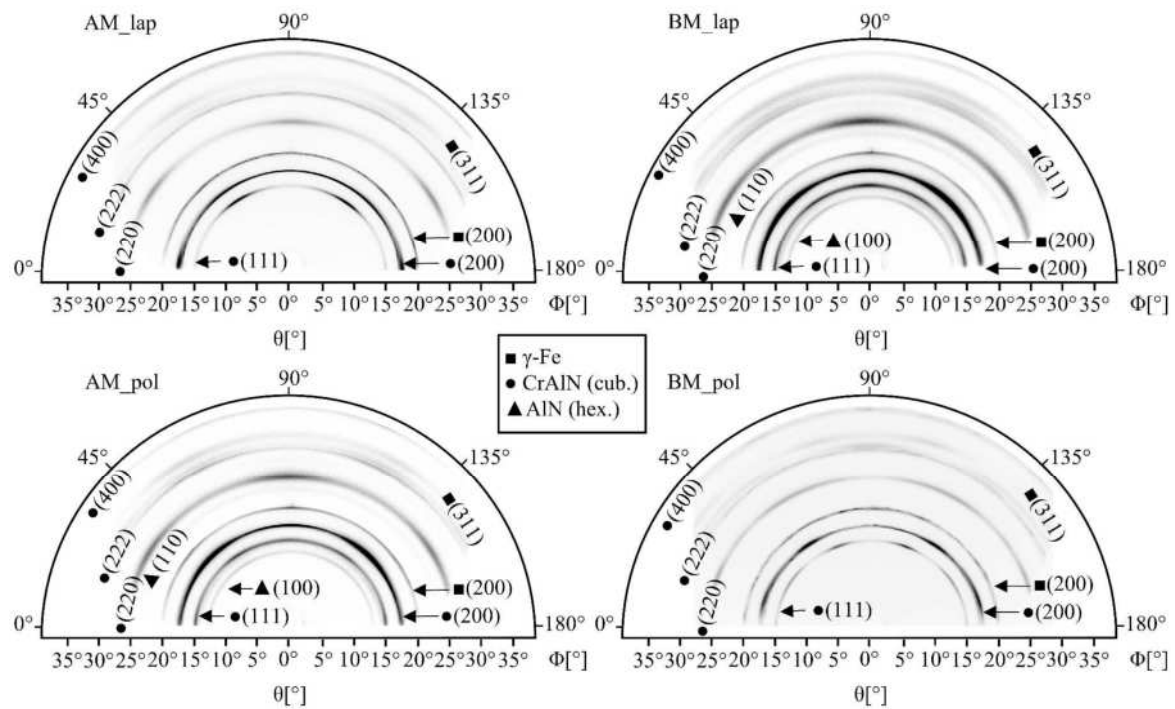


Figure 2: Two-dimensional XRD patterns of the CrAlN coating deposited on the different 316L substrates

Acknowledgements

The authors gratefully acknowledge the DELTA machine group for providing synchrotron radiation and their support at BL9. In addition, the authors gratefully thank the German Research Foundation (DFG) for the financial support. This work results from the project (TI343/130-1). The Chair of Materials Science at the Paderborn University is acknowledged for providing the additive manufactured substrates.

References

- [1] I. Gibson, D. Rosen, and B. Stucker, *Additive Manufacturing Technologies: 3D Printing, Rapid Prototyping and Direct Digital Manufacturing*. Springer, Berlin, 2015
- [2] J.-P. Kruth, M. Badrossamay, E.Yasa, J. Deckers, L. Thijs, J. Van Humbeeck, *Part and Material Properties in Selective Laser Melting of Metals*, Proceedings of the 16th International Symposium on Electromachining, Shanghai, China, 2010, p 1–12
- [3] Y. Liu, Y. Yang, and D. Wang, *A Study on the Residual Stress During Selective Laser Melting (SLM) of Metallic Powder*, *Int. J. Adv. Manuf. Technol.*, 2016, 87(1–4), p 647-656
- [4] J. Sander, *Selektives Laserschmelzen hochfester Werkzeugstähle*, Saechsische Landesbibliothek-Staats- und Universitaetsbibliothek Dresden, Technische Universität, Dresden, 2018
- [5] B. Kocabekir, R. Kacar, S. Guñduñz, and F. Hayat, *An Effect of Heat Input, Weld Atmosphere and Weld Cooling Conditions on the Resistance Spot Weldability of 316L Austenitic Stainless Steel*, *J. Mater. Process. Technol.*, 2008, 195(1–3), p 327-335
- [6] J. Suryawanshi, K.G. Prashanth, and U. Ramamurty, *Mechanical Behavior of Selective Laser Melted 316L Stainless Steel*, *Mater. Sci. Eng. A*, 2017, 696, p 113-121
- [7] J.V. Ramana, S. Kumar, C. David, V.S. Raju, *Structure, composition and microhardness of (Ti,Zr)N and (Ti,Al)N coatings prepared by DC magnetron sputtering*, *Mater. Lett.*, 2004, 58, p 2553-2558
- [8] R. Lamni, R. Sanjinés, F. Lévy, *Electrical and optical properties of Zr1–xAlxN thin films*, *Thin Solid Films*, 2005, 478, p 170-175
- [9] P. Sieczkarek, S. Wernicke, S. Gies, A.E. Tekkaya, E. Krebs, P. Wiederkehr, D. Biermann, W. Tillmann, D. Stangier, *Wear behavior of tribologically optimized tool surfaces for incremental forming processes*, *Tribol. Int.*, 2016, 104, p 64-72
- [10] P.E. Gannon, C.T. Tripp, A.K. Knospe, C.V. Ramana, M. Deibert, R.J. Smith, V.I. Gorokhovskiy, V. Shutthanandan, D. Gelles, *High-temperature oxidation resistance and surface electrical conductivity of stainless steels with filtered arc Cr–Al–N multilayer and/or superlattice coatings*, *Surf. Coat. Technol.*, 2004, 188-189, p 55-61
- [11] M. Schmid, G.N. Levy, *Finishing and coating von SLS-Teilen für Additive Manufacturing (AM)* (in de), *RTEjournal – Forum für Rapid Technologie*, 2010, 7
- [12] W. Tillmann, C. Schaak, J. Nellesen, M. Schaper, M.E. Aydinöz, T. Niendorf, *Functional Encapsulation of Laser Melted Inconel 718 By Arc-PVD and HVOF for Post Compacting by Hot Isostatic Pressing*, *Powder Metall.*, 2015, 58(4), p 259-264
- [13] W. Tillmann, L. Hagen, C. Schaak, J. Liß, M. Schaper, K.-P. Hoyer, M. E. Aydinöz, K.-U. Garthe, *Adhesion of HVOF-Sprayed WC-Co Coatings on 316L Substrates Processed by SLM*, *J. Therm. Spray Technol.*, 2020, 29(6), p 1396-1409
- [14] W. Tillmann, D. Stangier, L. Hagen, P. Schröder, M. Krabiell, *Influence of the WC grain size on the properties of PVD/HVOF duplex coatings*, *Surf. Coat. Technol.*, 2017, 328, p 326–334
- [15] L. Zauner, P. Ertelthaler, T. Wojcik, H. Bolvardi, S. Kolozsvári, P. H. Mayrhofer, H. Riedl, *Reactive HiPIMS deposition of Ti-Al-N: Influence of the deposition parameters on the cubic to hexagonal phase transition*, *Surf. Coat. Technol.*, 2020, 382, p 125007

Temperature stability and decomposition of the hydrogen storage material NaBH₄

Robin Sakrowski¹, Maik Szafarska², Mirko Elbers¹, Georgia Sourkouni², Christian Sternemann¹, Lienhard Wegewitz³, Metin Tolan¹, and Wolfgang Maus-Friedrichs³

¹ Fakultät Physik/DELTA, TU Dortmund, 44221 Dortmund, Germany

² Clausthaler Zentrum für Materialtechnik, TU Clausthal, 38678 Clausthal-Zellerfeld, Germany

³ Institut für Energieforschung und Physikalische Technologien, TU Clausthal, 38678 Clausthal-Zellerfeld, Germany

Hydrogen storage is a key technology for an upcoming hydrogen economy. In this study, native sodium borohydride (NaBH₄) is studied as a candidate hydrogen storage material [1]. The aim of this experiment was the investigation of a temperature range of stability of NaBH₄ under vacuum conditions and Ar inert gas atmosphere for further experiments concerning the rehydrogenation in a non-thermal plasma. Native NaBH₄ forms H₂ and stable NaBO₂ for temperatures above 300°C [2,3] hence the influence of the environmental conditions is the key part of this study.

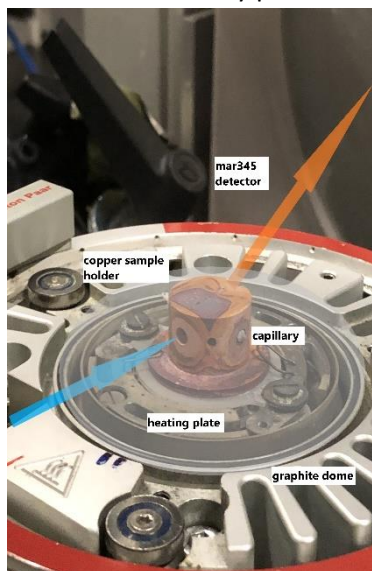


Fig. 1 Experimental set-up

In this experiment, we used a 20 keV x-ray diffraction setup of BL9 with a MAR345 image plate detector at 350 mm sample-detector distance. Heating the sample under either vacuum (about 0.1mbar), Ar atmosphere or air was realised with the domed hot stage DHS 1100 by Anton Paar. The powder samples were placed in the centre of rotation within capillaries placed in a copper holder (Fig.1). They were heated from 25°C to 550°C. All samples of NaBH₄ were bought from Sigma-Aldrich and used without further treatment. Five different runs, as well as melting point measurements for temperature calibration were performed (solid Zn+Al foil). LaB₆ was used as a standard for x-ray diffraction calibration and the diffraction images were analysed via the Fit2D software package. A higher order polynomial function was fitted to subtract air scattering contribution for all patterns. In a second step a scaled background from the graphite dome was subtracted. The patterns are normalised to their previous maximum intensity of the first graphite signal after the polynomial subtraction for a better comparison.

The results of a temperature run with a NaBH₄ sample are shown in Fig. 2. The stabilizing effect of Ar and vacuum atmosphere could be demonstrated.

The diffraction data suggest working at a maximum H₂ release temperature below 325°C, respective 495°C, depending on the heating atmosphere of to allow for isostructural H₂ removal at these conditions. Using ultra-high vacuum or inert atmosphere is expected to shift the isostructural H₂ release regime to temperatures close to its melting temperature of about 500 °C, i.e. optimized for reversible isostructural hydrogen release and non-thermal plasma-based rehydrogenation.

These results will be combined with H₂ plasma re-loaded data with additional methods like mass spectroscopy and a quantitative phase analysis will be performed with Rietveld refinement using MAUD© software by L. Lutterotti.

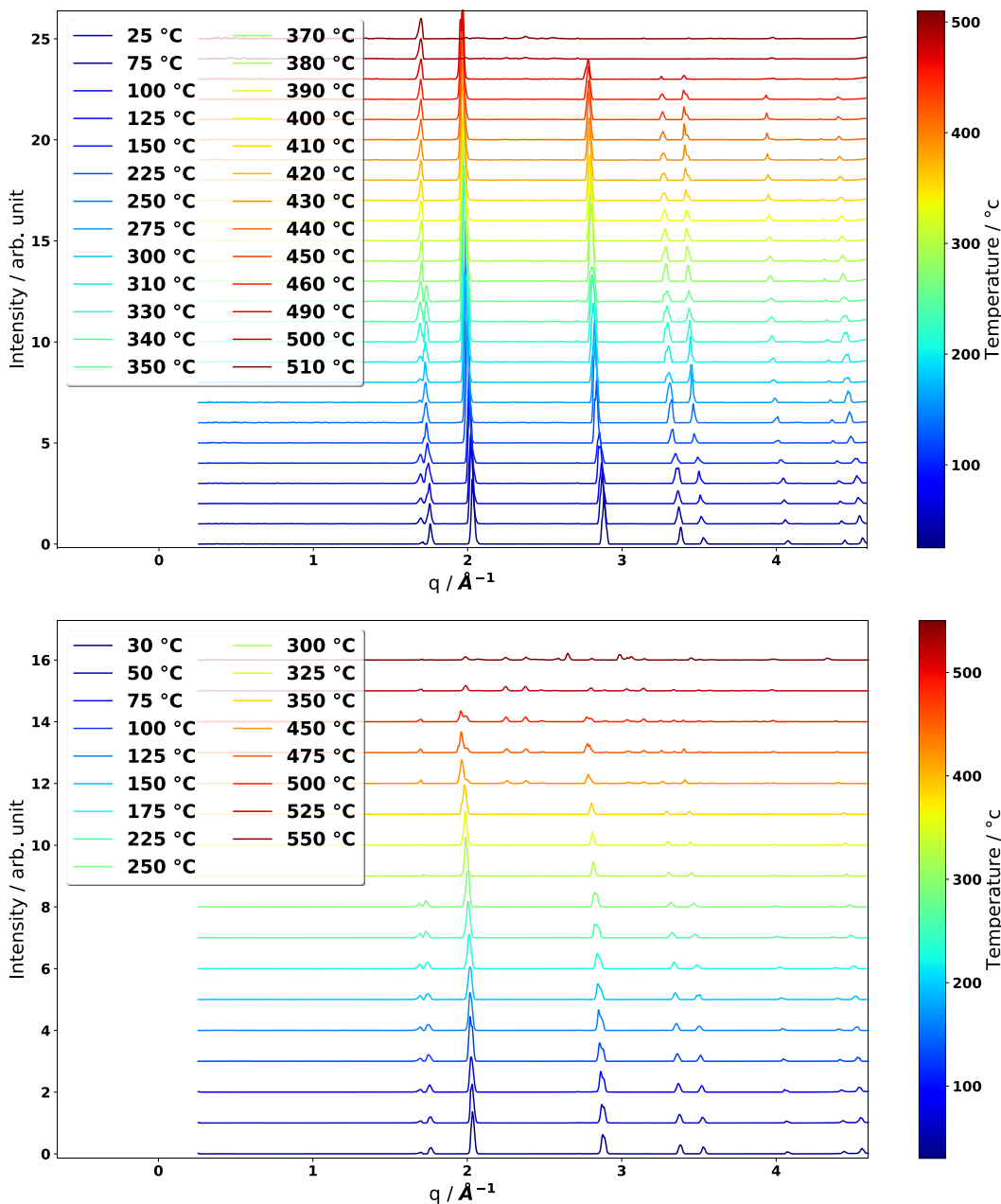


Fig.2 Top: X-ray diffraction patterns of native NaBH₄ measured in Ar atmosphere. The patterns are shifted vertically by arbitrary factors for clarity. The sample shows no signs of oxidation to NaBO₂ over a wide temperature range up to total decomposition above 500 °C. Bottom: Same experiment but performed with air atmosphere shows oxidation above 325°C.

Reference:

- [1] J. Mao and D. Gregory, *Recent Advances in the Use of Sodium Borohydride as a Solid State Hydrogen Store*, *Energies* 8.1, S.430-453 (2015).
- [2] G. Sourkouni, F. Voigts, J.C. Namyslo, S. Dahle, W. Maus-Friedrichs, C. Argiris, *Interaction mechanism of hydrogen storage materials with layer-by-layer applied protective polyelectrolyte coatings*, *International Journal of Hydrogen Energy* 39.27, S. 14834-14842 (2014).
- [3] S. Dahle, J. Meuthen, M. Marschewski, A. Schmidt, W. Maus-Friedrichs, G. Sourkouni, Chr. Argiris, *The influence of protecting polyelectrolyte layers on the temperature behaviour of NaBD₄*, *RSC Adv.* 4, S.2628-2633 (2014).

Acknowledgement

We would like to thank the DELTA machine group for providing synchrotron radiation and technical support.

Using reflectivity data to gain insights into microbiologically influenced corrosion of metal reducing bacteria (MRB) on stainless steel surfaces

Nina Wurzler ^a, Jan David Schütter ^a, Ralph Wagner ^b,
Dirk Lützenkirchen-Hecht ^b, Ozlem Ozcan ^a

^a Federal Institute for Materials Research and Testing, Berlin, Germany

^b Bergische Universität Wuppertal, Wuppertal, Germany

Stainless steel is forming a stable surface oxide layer composed of iron and chromium oxides as a protective effect against corrosion [1]. In microbiologically influenced corrosion (MIC), metal reducing bacteria are known to play a major role in the onset of pitting corrosion due to the ability to use various metallic compounds as electron acceptors. The stable metal oxides in the protective film are reduced to more soluble species during the bacterial metabolism, which can lead to an alteration and weakening of the corrosion resistance of stainless steels [2,3,4,5]. To understand the processes of bacterial metal reduction the bacteria *Shewanella putrefaciens* CN32 have been grown with and without the presence of Fe³⁺ species to examine the adaptability of the bacteria to iron usage.

Therefore, ex situ experiments at the Fe K-edge and the Cr K-edge have been performed to elucidate the changes in oxide chemistry after incubation with the bacterial cultures. In a three-electrode set-up stainless steel 304 (grinded to P1200) was connected as working electrode. A 60min. mild polarization to +50mV vs. Ag/AgCl in 20mM NaClO₄ with a gold counter electrode was performed. The steel coupons were then incubated with different solutions. The bacterial cultures regularly grown, in the following named CN32, and grown with iron (Fe(III)-citrate, 16g/l), named FeCi, as well as the filtered growth medium only with the secreted molecules and EPS (CN32.filtrate or FeCi-filtrate) were tested. After 20h of incubation, the coupons were placed on the sample holder and θ scans have been performed for optimal positioning of obtaining X-ray absorption spectra in grazing incidence.

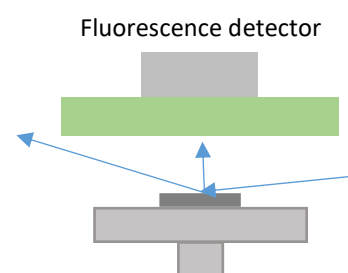


Figure 1: schematics of the ex situ experimental setup

All the XANES experiments have been performed at DELTA beamline 8 and the data was collected in total reflection mode using a channel cut Si(111) monochromator and gas-filled ionization chambers as detectors. The samples were placed parallel to the x-ray beam and positioned with a transmission detector. A rocking curve of the tilt angle θ was performed from 0° to 0.8° to define the exact angle of grazing incidence for each sample. Fluorescence spectra in grazing incidence were analyzed at the Fe and Cr edges after pre-conditioning and after 20h incubation with different microbial electrolytes [6].

The reflection intensity is dependent on the materials density and carries information about the material's interfacial roughness and the film thickness. As the surface oxide of stainless steel has different characteristics as the bulk material and usually is in the range of below 6nm, it can be thought of as a thin film on. As can be seen in Figure 2 [6], the curve of freshly prepared surfaces is centered at 0.22-0.25° for Fe and Cr edge, respectively. In the reflection curve representing the incubated samples, a shoulder peak develops at lower angles. This can be explained by a thickening of the surface oxide layer due to bacterial activity [6].

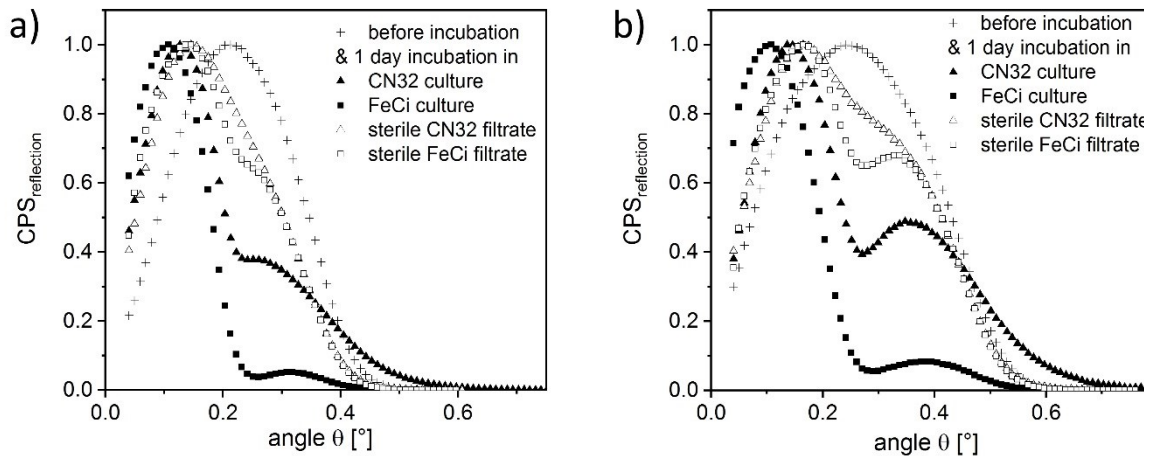


Figure 2: reflectivity data from θ -scans of steel coupons for *ex situ* XANES spectra positioned for grazing incidence conducted at DELTA beamline 8, fresh steel coupon as reference and 1d incubation in medium with and without bacteria; left: at energies just before the Fe K-edge, right: at energies just before the Cr K-edge [6]

A gaussian peak fitting on the data was performed and the data is presented from [6] in Table 1 and Table 2 for Fe and Cr edge energies, respectively. With respect of the incomplete information of the interfacial roughness and the film thicknesses for a dedicated fit applying the Fresnel theory and the Parratt-algorithm for multilayer sample systems [7], the simplified fit is an attempt to use the gained information. The double peak appearance results in a distinct ratio between the peak heights. The low θ and high θ peaks ($h_{\text{Peak2}} / h_{\text{Peak1}}$) increases significantly for the samples incubated in the FeCi culture. This indicates an extensive thickening of the oxidic/hydroxidic surface layer between the biofilm and the steel surface in presence of iron adapted bacteria compared to regular grown CN32. Furthermore, for FeCi incubated samples, the low θ peak assigned to the oxide/hydroxide film is shifted to lower angles with increasing $h_{\text{Peak2}} / h_{\text{Peak1}}$ ratio [6].

Table 1. Peak fitting results of the reflectivity data at Fe pre-edge (6900 eV) [6]

| Fe pre-edge | Peak # | Center [°] | FWHM | Height (h) | $h_{\text{Peak1}} / h_{\text{Peak2}}$ |
|---|--------|------------|------|------------|---------------------------------------|
| Before incubation | 1 | 0.27 | 0.17 | 0.59 | 1.2 |
| | 2 | 0.16 | 0.18 | 0.72 | |
| 1 d incubation in sterile CN32 filtrate | 1 | 0.27 | 0.16 | 0.49 | 1.9 |
| | 2 | 0.13 | 0.17 | 0.93 | |
| 1 d incubation in sterile FeCi filtrate | 1 | 0.29 | 0.14 | 0.44 | 2.3 |
| | 2 | 0.13 | 0.18 | 1 | |
| 1 d incubation CN32 culture | 1 | 0.3 | 0.2 | 0.32 | 3.1 |
| | 2 | 0.12 | 0.14 | 0.98 | |
| 1 d incubation in FeCi culture | 1 | 0.33 | 0.08 | 0.05 | 20.0 |
| | 2 | 0.10 | 0.14 | 1 | |

Table 2. Peak fitting results of the reflectivity data at Cr pre-edge (5800 eV) [6]

| Cr pre-edge | Peak # | Center [°] | FWHM | Height (h) | h _{Peak2} / h _{Peak1} |
|---|--------|------------|------|------------|---|
| Before incubation | 1 | 0.35 | 0.22 | 0.65 | 1.2 |
| | 2 | 0.17 | 0.28 | 0.81 | |
| 1 d incubation in sterile CN32 filtrate | 1 | 0.35 | 0.21 | 0.62 | 1.5 |
| | 2 | 0.15 | 0.21 | 0.94 | |
| 1 d incubation in sterile FeCi filtrate | 1 | 0.36 | 0.19 | 0.61 | 1.6 |
| | 2 | 0.15 | 0.30 | 0.99 | |
| 1 d incubation CN32 culture | 1 | 0.37 | 0.25 | 0.47 | 2.1 |
| | 2 | 0.14 | 0.16 | 0.98 | |
| 1 d incubation in FeCi culture | 1 | 0.40 | 0.14 | 0.09 | 11.1 |
| | 2 | 0.10 | 0.18 | 1.0 | |

Shewanella putrefaciens are reducing the Fe(III) compounds in the oxide surface to Fe²⁺ species. The dissolved or re-passivated Fe²⁺ accumulates in the interface after becoming soluble. This transformation appears as an additional peak at lower θ angles with lower density and higher interfacial roughness. The extent of the changed peak ratios was much more pronounced for the FeCi incubated samples. Interestingly, the peak ratio variations were smaller for the reflectivity data at the lower Cr pre-edge energy [6]. An explanation can be the higher affinity to iron utilization of the FeCi culture to transform it into lower density species which accumulate at the interface forming a interims layer of dissolved or re-oxidized, porous compounds.

These findings provide a useful tool for further insights into the corrosion behavior of materials in biological environment. With further analysis, the peak height ratios or even the appearance of a second peak representing a film formation of lower density and higher interface roughness, can be applied as an additional aspect to MIC studies.

Acknowledgement

We gratefully acknowledge the DELTA machine group for providing synchrotron radiation reliably.

References:

- [1] H. A. Videla, L. K. Herrera, *International Microbiology* **2005**, *8*, 169-180.
- [2] P. Jogdeo, R. Chai, S. Shuyang, M. Saballus, F. Constancias, S. L. Wijesinghe, D. Thierry, D. J. Blackwood, D. McDougald, S. A. Rice, E. Marsili, *Journal of The Electrochemical Society* **2017**, *164*, C532-C538;
- [3] E. Marsili, D. B. Baron, I. D. Shikhare, D. Coursolle, J. A. Gralnick, D. R. Bond, *PNAS, Proceedings of the National Academy of Sciences* **2008**, *105*, 3968-3973.
- [4] J. K. Fredrickson, J. M. Zachara, D. K. Kennedy, M. C. Duff, Y. A. Gorby, S.-M. Li, K. M. Krupka, *Geochimica et Cosmochimica Acta* **2000**, *64*, 3085-3098.
- [5] A. A. Carmona-Martínez, F. Harnisch, U. Kuhlicke, T. R. Neu, U. Schröder, *Bioelectrochemistry* **2013**, *93*, 23-29.
- [6] N. Wurzler, J. D. Schutter, R. Wagner, M. Dimper, D. Lützenkirchen-Hecht, O. Ozcan, *Corrosion Science* **2020**, *174*, 108855.
- [7] L.G. Parratt, *Phys. Rev.* **1954**, *95*, 359-369.

The surface structure of medical implants

Eric Schneider, Michael Paulus, Dominic Stangier, Karl-Heinz Bauer and Metin Tolan

Fakultät Physik/DELTA, Technische Universität Dortmund, 44221 Dortmund, Germany

Osteosynthesis describes the surgical connection of broken or splintered bones to enable them to grow together. The healing of the bones is influenced by various properties of the connecting implant. For example, mechanical properties such as Young's modulus must be considered to avoid stress shielding or a reduction in bone density due to lack of stress. In addition to the mechanical properties of an implant, high corrosion resistance of the material and good biocompatibility is important. Usually implants made of titanium or the alloys TiAl6V4 and TiAl6Nb7 are used because they fulfil these conditions in an acceptable degree. Often the implants are additionally coated to further increase biocompatibility.

Although titanium generally has a good immunological compatibility, titanium implants may in some cases yield undesirable inflammatory symptoms based on the release of corroded titanium particles. In addition, implant surfaces contaminated by foreign atoms can cause incompatibilities. For this reason, the surface of titanium implants was examined for various external parameters using X-rays. It was found that the implants of certain manufacturers are mixed with zirconium oxide and corundum residues. Which can probably be traced back to the blasting process [1].

Further implants of the type "Proximal Humerus Plate" were examined by means of X-ray diffraction in order to increase the statistical significance. The diffraction experiments were

performed at the beamline BL9 using a photon energy of 27 keV.

The scattered radiation was detected by a MAR345 image plate detector. Different spots on the sample were tested in order to prove the surface homogeneity. In addition, a used implant of this type was examined, which allowed first comparisons between used and unused samples. In figure 1 the Bragg reflections of corundum (Al_2O_3) and zirconiumdioxide (ZrO_2) of four samples are shown. Thus all investigated implants show beside the desired zirconiumdioxide surface layer remnants of corundum. The quantitative analysis is still in progress.

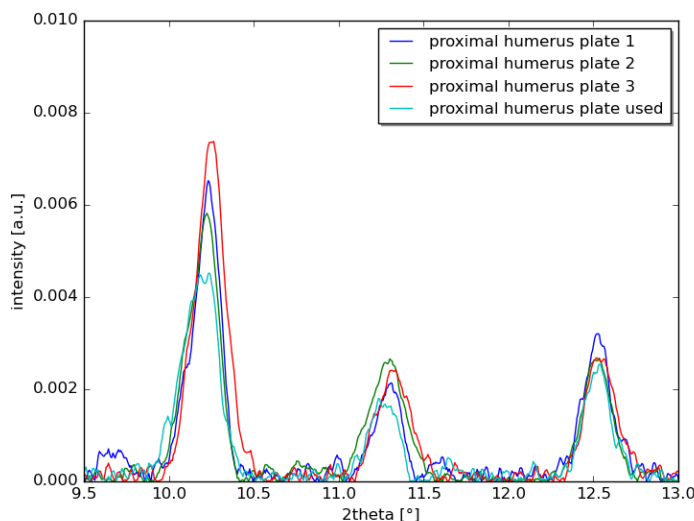


Figure 1: Diffractogram of four different titanium implants showing the corundum (10.25°) and zirconium oxide ($11.3^\circ; 12.55^\circ$) Bragg reflections.

Acknowledgments: We acknowledge the DELTA machine group for providing synchrotron radiation and technical support.

[1] Berger, K: Untersuchung der Oberflächenstruktur von Titanimplantaten zur Osteosynthese mittels Röntgendiffraktion. Masterarbeit (2019) TU Dortmund.

Ions at hydrophobic interfaces - the effect of pH

Elena Darscht, Michael Paulus, Susanne Dogan, Göran Surmeier, Mike Moron, Christian Sternemann, and Metin Tolan

Fakultät Physik/DELTA, TU Dortmund, 44221 Dortmund, Germany

Interfaces between solids and aqueous solutions are important systems where many biological and technical processes take place. These processes depend, among other things, on the surface properties of the solid and the chemical composition of the aqueous solution. Particularly noteworthy are the hydrophobic surfaces, which can have a strongly denaturing effect on proteins by interacting with the hydrophobic side chains of the proteins. Furthermore, it was observed that the structure of the aqueous phase near the hydrophobic interface can also deviate significantly from the structure in volume. By means of X-ray reflectometry a region of reduced water density was found directly above the hydrophobic interface, whose structural properties are still being discussed [1]. The structure of this depletion zone or hydrophobic gap has been investigated in dependence of different thermodynamic parameters like pressure and temperature as well as in the presence of proteins and ions [2,3].

A frequently used sample system to study the depletion region is a silicon wafer coated with octadecyltrichlorosilane (OTS) [4]. OTS consists of a reactive polar head group and a hydrophobic hydrocarbon chain as tail group. Since a natural silicon dioxide layer is formed on a silicon wafer, it is possible that the OTS binds to the SiO_2 in the presence of small amounts of water and under formation of HCl to form a monomolecular highly hydrophobic layer with the tail group pointing vertically away from the surface. Such a system has an extremely hydrophobic surface and was in the past considered rather impenetrable to substances dissolved within an aqueous phase stored above the OTS film.

However, first measurements at the interface between OTS and aqueous salt solutions at pH 7 have shown that ions may be deposited in the OTS films (see figure 1). Since the penetration of the salt ions in the hydrophobic regions of the OTS film is energetically disadvantageous, it is suggested that the ions interact with the SiO_2 layer below the OTS. If the wafer

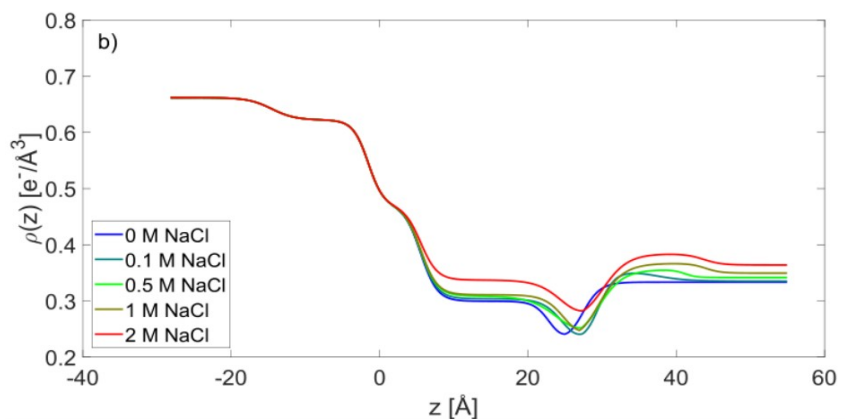


Figure 1: Electron density profiles of the OTS - aqueous solution interface at pH 7 [5].

is not completely covered with OTS, the SiO_2 layer has contact with the aqueous phase building up a strongly negative potential at pH 7. To confirm this assumption, additional reflectivity measurements were performed at low pH, where for this system the SiO_2 layer is almost uncharged.

The X-ray reflectivities were recorded at the beamline BL9 of the Dortmund synchrotron radiation source DELTA using a photon energy of 27 keV. First, the measurement was performed in air in order to obtain a reference layer model of the sample. In a second step the reflectivity of the OTS-water interface was recorded. For this purpose the wafer was covered with 2 ml water. For the measurements with the salt solutions under low pH, the corresponding substances, i.e. hydrochloric acid and sodium chloride, were added to the water. The sodium chloride was taken from a 5

molar NaCl stock solution. The salt concentration was slowly increased after each measurement.

The recorded reflectivities were analyzed using the Parratt algorithm in combination with the Effective Density Model. Different slice models were tested to check different adsorption scenarios. Figure 2 shows the resulting electron density profiles. The electron density profiles of the reflectivities of the NaCl solutions differ fundamentally in comparison with figure 1.

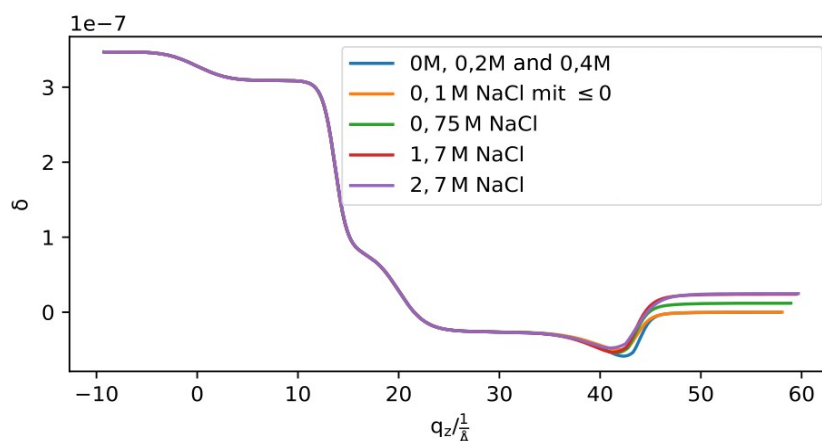


Figure 2: Dispersion profiles of the OTS - aqueous solution interface at pH 3. The dispersion of the water phase was subtracted.

While the measurements at pH 7 show significant changes in the tail group electron density, this region does not change at all for the reflectivities of NaCl-HCl solution. Furthermore, the pH 7 curves show the formation of a fifth layer above the depletion layer, which is also not the case for the electron density profiles of this study. Here, only the density of the aqueous solution increased by the addition of ions. Slight changes of the depletion layer are also visible in the electron density profiles. In conclusion, the charge of the SiO₂ layer has an enormous influence on the ion adsorption. A negatively charged SiO₂ layer activates the ions to penetrate partially into the tail group of the OTS. At low pH, the ions only affect the salt solutions' dispersion and to a small extent the depletion layer.

The authors thank the DELTA machine group for providing synchrotron radiation. The authors thank the DFG (FOR 1979) for financial support.

References:

- [1] M. Mezger, H. Reichert, S. Schöder, J. Okasinski, H. Schröder, H. Dosch, D. Palms, J. Ralston, and V. Honkimäki, High-resolution in situ x-ray study of the hydrophobic gap at the water-octadecyl-trichlorosilane interface, *PNAS* **103**, 18401-18404 (2006).
- [2] F.J. Wirkert, C. Hölzl, M. Paulus, P. Salmen, M. Tolan, D. Horinek, and J. Nase, The hydrophobic gap at High hydrostatic pressures, *Angewandte Chemie International Edition* **56**, 12958 (2017).
- [3] H. Hähl, F. Evers, S. Grandthyll, M. Paulus, C. Sternemann, P. Loskill, M. Lessel, A.K. Hüsecken, T. Brenner, M. Tolan, and K. Jacobs, Subsurface influence on the structure of protein adsorbates revealed by in-situ x-ray reflectivity, *Langmuir* **28**, 7747 (2012)
- [4] M. Lessel, O. Bäumchen, M. Klos, H. Hähl, R. Fetzer, M. Paulus, R. Seemann and K. Jacobs, Self-assembled silane monolayers: an efficient step-by-step recipe for high-quality, low energy surfaces, *Surface and Interface Analysis* **47**, 557 (2015).
- [5] Y. Forov, X-ray studies on adsorption processes at solid-liquid interfaces and ultrafast dynamics in water, Dissertation, Dortmund (2019).

Gas adsorption on hydrophobic surfaces near the critical point

Mike Moron, Nicola Thiering, Julia Nase, Michael Paulus, and Metin Tolan
 Fakultät Physik/DELTA, TU Dortmund, 44221 Dortmund, Germany

We investigated the pressure-dependent adsorption of sub- and supercritical fluids on hydrophobic surfaces. Silicon wafers were hydrophobized by coating them with a self-assembled octadecyltrichlorosilane (OTS) monolayer. OTS molecules bind covalently with their polar head group to the wafer surface. Thus, the nonpolar alkyl chains form a stable, hydrophobic surface. The gases under investigation were hexafluoroethane (C_2F_6 , $p_{crit}^{C_2F_6} = 30.48 \text{ bar}$, $T_{crit}^{C_2F_6} = 19.88 \text{ }^\circ\text{C}$) and carbon dioxide (CO_2 , $p_{crit}^{CO_2} = 73.75 \text{ bar}$). Exemplary, the C_2F_6 measurements will be discussed. Since the thickness of gas adsorption layers are on the atomic scale, we performed x-ray-reflectivity (XRR) experiments with a photon energy of 27 keV at the beamline BL9 at DELTA. With the XRR technique we obtain direct insight into the vertical electron density profile of the substrate and the adsorbed gas layers. The recorded reflectivity curves for C_2F_6 at different pressures are shown in Fig. 1. The measurements were performed at $T = 13 \text{ }^\circ\text{C}$, thus below T_{crit} . With increasing pressure, the reflectivities show a shift of the first minimum in the direction of smaller wave vector transfers q_z , which indicates an increased adsorption of C_2F_6 molecules on the surface. In Fig. 2 the corresponding electron density profiles are shown. The electron density profiles were obtained by fitting a model system to the data using the Parratt algorithm in combination with the Effective Density model [1]. The first layer that is visible in Fig. 2 represents the silicon substrate. The second layer corresponds to a SiO_2 layer that is formed when the wafer is exposed to air. The next two layers represent the head group and the tail group of the OTS molecules.

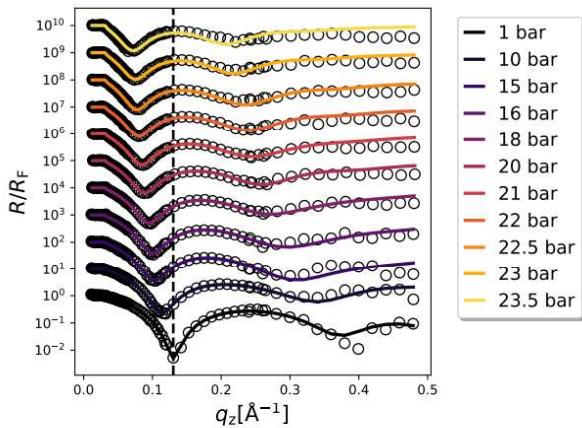


Fig. 1: Reflectivities of the C_2F_6 measurements

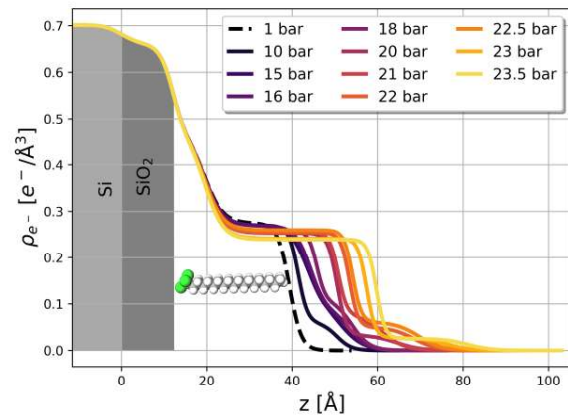


Fig. 2: Electron density profiles of C_2F_6 measurements



The top layers in the electron density profiles describe the adsorbed C_2F_6 . An increase of the thickness of the OTS tail group with rising pressure was found, which can be attributed to an intrusion of the C_2F_6 molecules into this layer. In addition, an adsorption of C_2F_6 on top of the OTS tail group can be observed. Fig. 3 shows the layer thicknesses of the OTS tail group and of the C_2F_6 layer as a function of the pressure normalized to the saturation vapor pressure. The data analysis especially of the supercritical systems is still in progress.

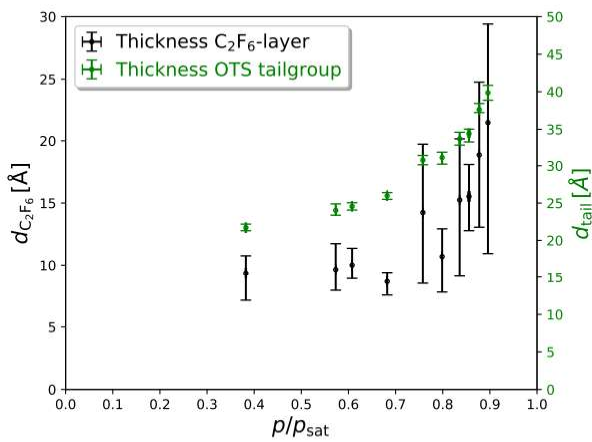


Fig. 3: Thickness of OTS tailgroup and C_2F_6 layer

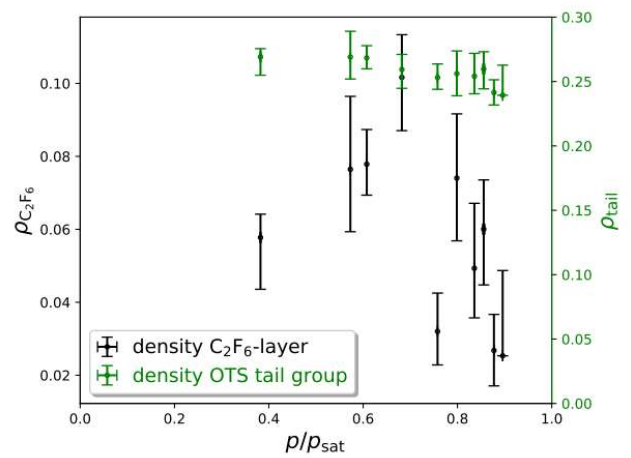


Fig. 4: Density of OTS tailgroup and C_2F_6 layer

Acknowledgements: This work is supported by the Federal Ministry of Education and Research (BMBF project number: 05K19PEA). We also acknowledge the DELTA machine group for providing synchrotron radiation and technical support.

References:

- [1] M. Tolan. X-Ray Scattering from Soft-Matter Thin Films: Materials Science and Basic Research. Springer Tracts in Modern Physics. Springer Berlin Heidelberg, 1998.

DELTA EXPERIMENTAL REPORT

Proposal Number: ID 77

Title: Vapor phase deposition of metal-organic frameworks thin films

Proposer: Alexander John CRUZ, Rob AMELOOT

Beamline users: Alexander John CRUZ, Victor RUBIO-GIMENEZ, Nathalie WAUTERAERTS

Beamline(s): X-RAY DIFFRACTION (BL 9), Delta Synchrotron, TU Dortmund, Germany

Shifts: 11.8

Summary

Various metal-organic framework (MOF) thin film samples were investigated in terms of phase analysis and crystal (preferential) orientation. The following MOFs were measured in the BL9 beamline: zinc-2-methylimidazolate (ZIF-8), zinc-4,5-dichloromidazolate (ZIF-71/ZIF-72), and copper benzenethiol (Cu-BHT). A preferred orientation can be observed in all of the MOF samples. Furthermore, we were able to successfully perform an *in situ* annealing experiments from room temperature up to 350 °C for ZIF-8. The impact of the different synthesis and deposition parameters are elucidated from the results of the experiments at BL 9. Moreover, the determination of the underlying crystallographic unit cell can be performed and the crystal structure can be resolved.

Experimental Performance and Preliminary Results

Grazing Incidence X-ray Diffraction Experiments were performed at various angles of incidence. This variation of the angle of incidence to the larger angles reduces the beam footprint at the sample surface which can lead to diffraction patterns with higher resolution, especially for ultrathin films. At BL 9, *ex situ* measurements were also performed to determine the crystallinity of samples for the MOF thin films (~30-200 nm).

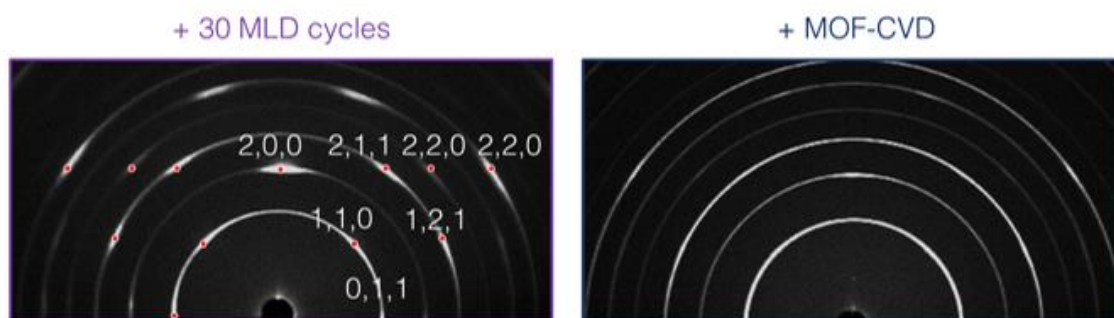


Figure 1: *Ex situ* measurement of an oriented ZIF-8 layer after the deposition of another ZIF-8 film by molecular layer deposition (MLD) and chemical vapor deposition (CVD).

Oriented MOF-CVD and MOF-MLD ZIF-8 films. Oriented samples of ZIF-8 were measured and evaluated after employing various processes like molecular layer deposition (MLD, *unreported work, manuscript in preparation*) and chemical vapor deposition (CVD)¹ on both Si substrates and porous alumina support. The simulated Bragg peaks positions expected for a (100) oriented film (CCDC: VELVOY).

A 2× volume increase after 20 cycles of MLD ZIF-8 coating, estimated by calculating the surface area of the crystallite and the thickness of the MLD coating, resulted in insignificant changes in the relative intensities of the diffraction peaks of the ZIF-8 supercrystals with a (100)-preferred orientation while preserving the morphology (when validated by SEM). With MOF-CVD, GI-XRD patterns instead resulted in a less preferentially oriented pattern, potentially induced by local recrystallization evidenced by the change in morphology. The preserved diffraction pattern of (100)-oriented ZIF-8 supercrystals, *i.e.*, pronounced [200] peak after 30 MLD cycles suggest that the orientation is preserved, *i.e.*, *quasi-epitaxial growth*.²

MOF-CVD ZIF-71 and ZIF-72 mixed polymorphs

Using the same optimized conditions as with ZIF-8, the 4,5-dichloroimidazole (HdCIM) linker was used instead of 2-methylimidazole (HmIM). By varying the deposition conditions, up to 4 types of ZIF-71 or Zn(dCIM)₂ were deposited with different crystalline phases (**Figure 2**). It is practically impossible to resolve the crystal structure with the GI-XRD data alone given the wide-range of possible polymorphs of this particular ZIF family. Nevertheless, the diffraction pattern of **B** matches ZIF-72, a dense polymorph of ZIF-71 with *lcs* topology.

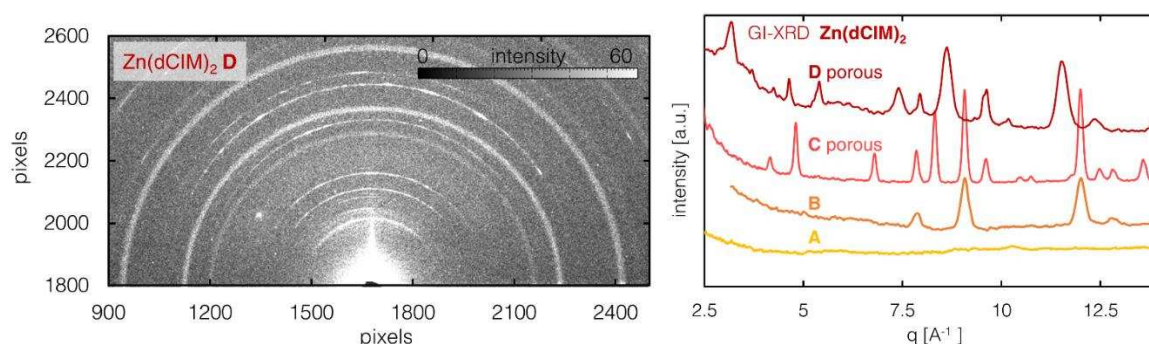
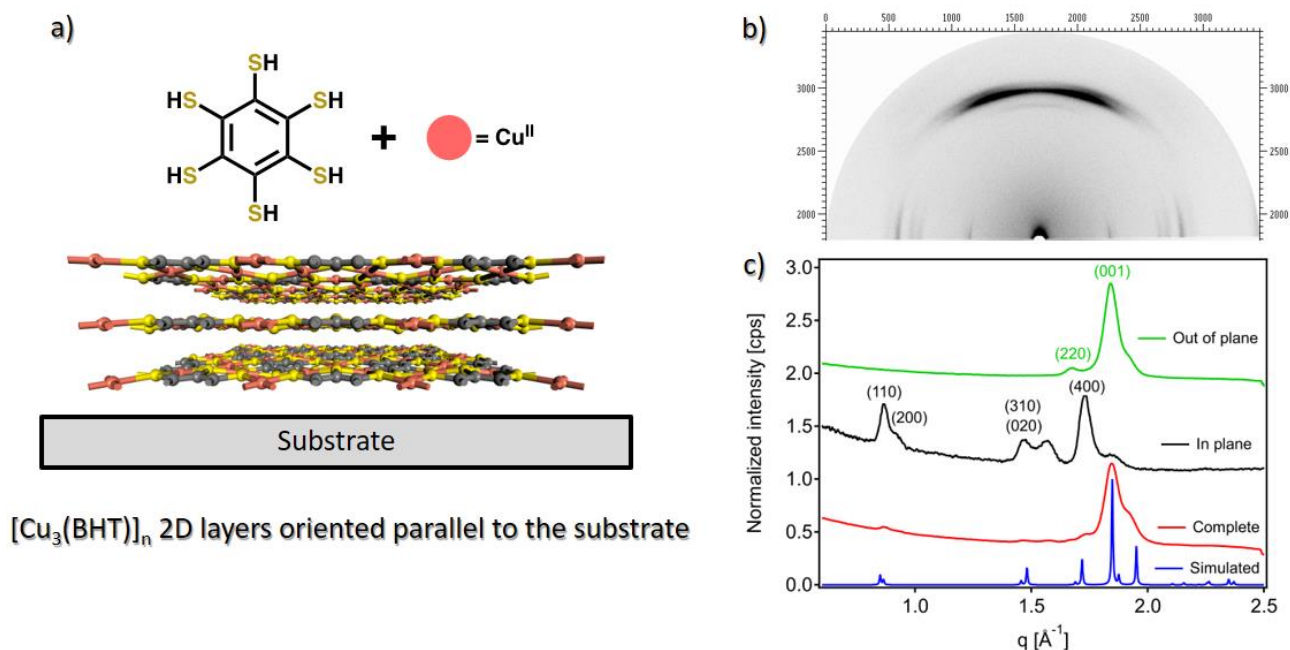


Figure S25 | Synchrotron GI-XRD pixel image of Zn(dCIM)₂-D (left) and the integrated patterns from the 2D data (right)

CVD of 2D MOFs: copper benzenehexanethiol (Cu-BHT)

The same strategies were implemented for another type of MOF, Cu-BHT. The results corroborate that the film is preferentially oriented with the 2D layers standing parallel to the substrate (Figure 3)



$[\text{Cu}_3(\text{BHT})]_n$ 2D layers oriented parallel to the substrate

Figure 3. a) Schematic representation of the components of Cu-BHT, benzenehexanethiol (BHT) ligand, and Cu^{II} ions, along with the disposition of the 2D layers onto the substrate according to the GIXRD data obtained at DELTA. b) 2D-GIXRD image of a Cu-BHT film. c) Out-of-plane, in-plane and complete integration XRD patterns as extracted from the 2D-GIXRD image along with a simulated diffractogram for a Cu-BHT.

References

- (1) Cruz, A. J.; Stassen, I.; Krishtab, M.; Marcoen, K.; Stassin, T.; Rodríguez-Hermida, S.; Teyssandier, J.; Pletincx, S.; Verbeke, R.; Rubio-Giménez, V.; Tatay, S.; Martí-Gastaldo, C.; Meersschaut, J.; Vereecken, P. M.; De Feyter, S.; Hauffman, T.; Ameloot, R. Integrated Cleanroom Process for the Vapor-Phase Deposition of Large-Area Zeolitic Imidazolate Framework Thin Films. *Chem. Mater.* **2019**, *31* (22), 9462–9471.
- (2) Hashem, T.; Valadez Sánchez, E. P.; Weidler, P. G.; Gliemann, H.; Alkordi, M. H.; Wöll, C. Liquid-Phase Quasi-Epitaxial Growth of Highly Stable, Monolithic UiO-66-NH₂ MOF Thin Films on Solid Substrates. *ChemistryOpen* **2020**, *9* (5), 524–527.

Phase transition of cobalt valence tautomers tracked via X-ray powder diffraction at beamline BL9

Florian Otte^{1,2}, Kevin Lehninger¹, Christian Albers¹, Robin Sakrowski¹, Sergio Jannuzzi³, Frederico Alves Lima², Christian Sternemann¹ and Metin Tolan¹

¹ Fakultät Physik/DELTA, TU Dortmund, 44221 Dortmund, Germany

² FXE Instrument, European XFEL GmbH, 22869 Schenefeld, Germany

³ MPI for Chemical Energy Conversion, Mülheim, Germany

A set of polycrystalline cobalt samples was investigated with X-ray powder diffraction during temperature-induced valence tautomeric transition. Valence tautomeric (VT) transitions are characterized by stimulated intramolecular charge transfer and single-site spincrossover.^{1,2} The goal of this experiment was to explore the potential to pinpoint structural changes during VT transition in powder diffraction data and, as a second step, the verification of transition temperatures and behavior of the synthesized samples.

To record powder diffraction data, a standardized diffraction setup was used at BL9. The sample was positioned inside a horizontally mounted borosilicate glass capillary with 2 mm diameter at 1015 mm distance from a Pilatus 100K-S area detector. The detector was fixed at the end of a goniometer arm, which allowed the acquisition of scattering angles 2θ in the range of ca. $2 - 17^\circ$ by scanning the arm along its elevation angle. This technique essentially samples a vertical slice of the scattering cone, where the width of the slice is given by the horizontal chip size of the detector. The beam size was set to be ca. $1.5 \text{ mm} \times 0.6 \text{ mm}$ (H x V) with the use of slits. The incoming photon energy was monochromatized to 15 keV with a Si(3,1,1) double crystal monochromator. The samples were grinded and filled into the glass capillaries shortly before the measurement. The sample capillary was mounted onto a pressured-air driven rotation stage which spun the capillary during the measurement along its central axis for a powder average. VT transitions were induced by cooling with an LN₂-operated cryojet, which was mounted at a nozzle-distance of approximately 5 mm above the sample. In this configuration, typical integration times to collect a powder diffraction dataset were around 900 s per sample per temperature point.

A pixel-based approach to the reduction and assembly of diffraction data collected at BL9

A full dataset was recorded as a series of detector images at different goniometer angles. The diffraction pattern was then obtained by calculating geometrically, for each scan step,

- (i) the detector chip surface normal based on the goniometer angle,
- (ii) the resulting true scattering angle $2\theta_{\text{pix}}$ of each pixel position on the detector.

Resulting data pairs $\{2\theta_{\text{pix}}, \text{pixel intensity}\}$ were then binned along values for $2\theta_{\text{pix}}$, i.e. intensities for similar $2\theta_{\text{pix}}$ values were added up. This approach allowed for full exploitation of the 2D data with minimal losses in resolution or counting statistics. The final result is a distribution of intensities over 2θ .

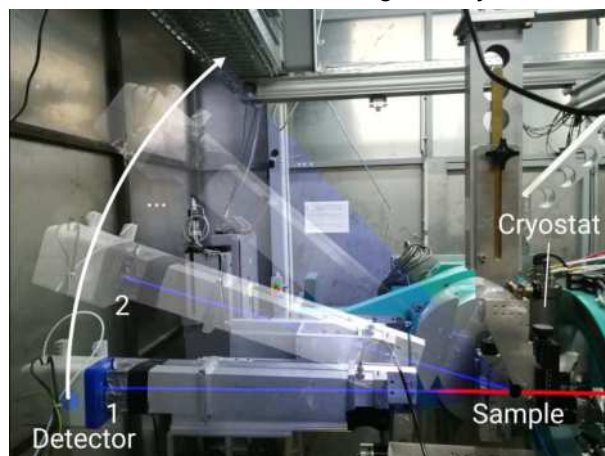


Fig. 1. Standard goniometer setup at BL9 with LN₂ cryojet installed from the top above the sample.



Fig. 2. Sample inside borosilicate capillary spun via pressured air during measurement to reduce anisotropy effects.

Diffraction data on cobalt valence tautomers

A set of four cobalt-based samples was investigated. The samples are of general form $[\text{Co}(\text{DTB})_2 \text{X}]$, where the central Co atom is coordinated to three ligands, one ancillary (non-innocent) ligand (denoted by X) and two dioxolene ligands. For the investigated samples, the ancillary ligand was either 1,10-phenanthroline (phen), 2,2'-bipyridine (bpy), N,N,N',N'-tetramethylethylenediamin (tmeda) or 4,4'-diphenyl-2,2'-bipyridine (dpbpy).

Preliminary analysis unveils significant shifts in the position of diffraction peaks of all investigated compounds when temperature is varied (Fig. 3 and Fig. 4). The intensities of diffraction peaks are influenced as well during VT transitions. As can be observed, peak positions during VT transition do not change monotonically along the 2θ -axis, as would be expected for a bare increase of lattice constant, giving indication for the hypothesis that VT transitions can indeed be monitored via XRPD, and furthermore, might even be susceptible to modeling via theoretical calculations. Transition temperatures show good agreement with values in literature, with a broader transition in the range of 200K to 270K for the (phen) complex as reported by Adams et al.³ and a sharp transition at 200K as reported by Sato et al.⁴ for the (tmeda) compound.

Conclusion and Outlook

Upcoming modelling and calculations have to be based on reliable crystal structures of these compounds. These structures do not yet exist for all compounds. The collected data on its own provides a useful and complementary view on the transitions temperatures and the crystalline phases of cobalt tautomers during transition. The temperature control via the cryojet proved challenging. An improvement here would be to use a different type of cryostat or use secondary precise thermometers at the sample position to monitor true sample temperature. As the sample capillary is quickly spinning, a first measure might be to optimize the dry air flow around the sample environment to inhibit the buildup of ice. The mount of the capillaries inside the goniometer head might be improved in the future by pre-mounting the capillaries onto an adapter piece. A proper way to ensure homogeneity of the (bpy) sample has to be found. Even though the sample was grinded, artefacts in the data due to small crystallites are suspected.

References:

1. Shultz, D. A. in *Magnetism: Molecules to Materials II* 281–306 (Wiley-VCH Verlag GmbH & Co. KGaA, (2003).
2. Hendrickson, D. N. & Pierpont, C. G. in 1, 63–95 (2004).
3. Adams, D. M., Dei, A., Rheingold, A. L., & Hendrickson, D. N. *Journal of the American Chemical Society*, 115(18), 8221–8229 (1993).
4. Sato, O., Hayami, S., Gu, Z. Z., Takahashi, K., Nakajima, R., Seki, K., & Fujishima, J. *Photochem. Photobiol. A*, 149(1–3), 111–114. (2002).

Acknowledgment

We would like to thank the DELTA machine group for providing synchrotron radiation and technical support. FO acknowledges funding via BMBF (05K16PE1) and RS via DFG (STE 1079/2-1).

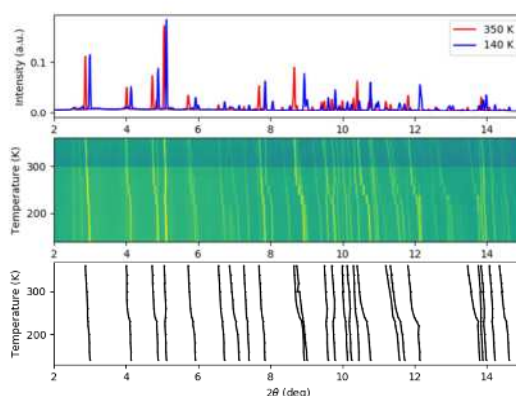


Fig. 3. Powder diffraction data on $\text{Co}(\text{phen})(3,5\text{-DTB})_2$. Top: Diffraction patterns recorded at highest and lowest temperature. Center: Diffraction spectra show as map for all temperatures. Bottom: Extracted diffraction peak positions, indicating a transition between 200K and 270K.

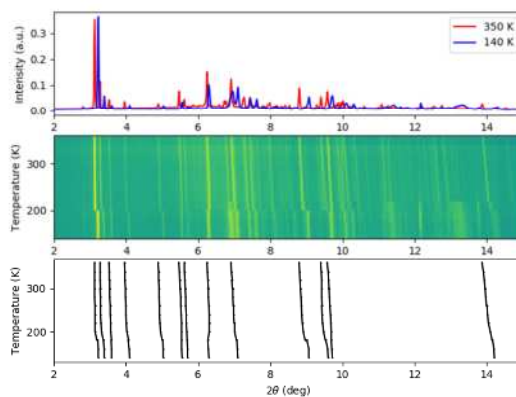


Fig. 4. Powder diffraction data on $\text{Co}(\text{tmeda})(3,5\text{-DTB})_2$. Top: Diffraction patterns recorded at highest and lowest temperature. Center: Diffraction spectra show as map for all temperatures. Bottom: Extracted diffraction peak positions, indicating a transition around 200K.

Studying the mechanics of metal-organic frameworks with high-pressure powder X-ray diffraction

Pascal Kolodzeiski, Louis Frenzel-Beyme, Roman Pallach, Jianbo Song, Sebastian Henke*

Anorganische Chemie – TU Dortmund, Otto-Hahn-Str. 6, 44227 Dortmund

Scientific Context

Metal-organic frameworks (MOFs) are an emerging class of porous solid state materials.^[1,2] Due to their porous nature and structural versatility several applications, ranging from gas storage and separation to catalysis, have been proposed for these materials. So far, investigations have been predominantly focussed on the synthesis of new materials with novel or optimized properties.^[3,4] Less research has been performed to investigate their fundamental properties regarding the materials' structural behaviour towards temperature or mechanical pressure. Nevertheless, especially those properties are highly important when it comes to industrial applications. In this regard a series of isorecticular MOF-74(M) materials (chemical composition = $M_2\text{dobdc}$, dobdc^{4-} = 2,5-dioxido-1,4-benzenedicarboxylate, M^{2+} = Zn^{2+} , Co^{2+} , Ni^{2+} , Cu^{2+} , Mg^{2+}) is of special interest (Fig. 1, top).^[5] Due to the presence of unsaturated binding sites on the incorporated square pyramidally coordinated metal ions, these compounds feature outstanding properties in gas separation and catalysis.^[6-8] Here, we access the mechanical stability of different MOF-74(M) derivatives with various metal ions, via high-pressure powder X-ray diffraction (HP-PXRD) in the range from ambient pressure up to 4000 bar.

We established and optimized an experimental setup for *in situ* HP-PXRD measurements at Beamline 9 (BL9) via modification of a previously developed high-pressure X-ray reflectivity cell (Fig. 1, bottom).^[9] This setup utilizes water as pressure transmitting medium (PTM) with an estimated precision of ca. 10 bar in the range from ambient pressure to 4000 bar. These pressures are relatively low, when compared to the pressures achieved in diamond anvil cells (DACs), the standard sample environment for HP-PXRD. Importantly, for the relatively soft and flexible MOF materials of interest here, this lower pressure range is perfectly suited.

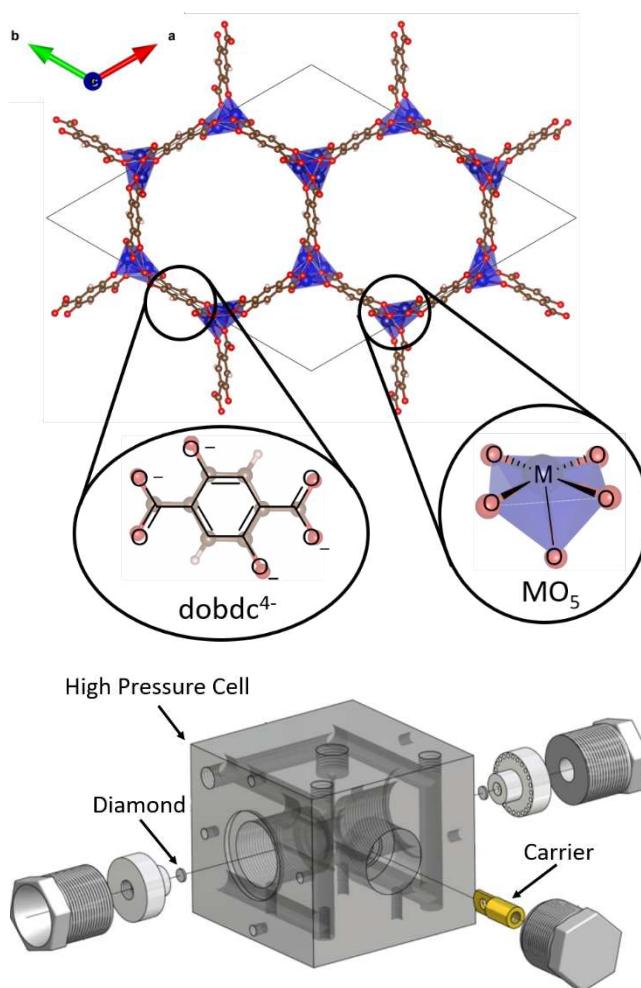


Figure 1: Top: Representation of the structure of MOF-74(M) with a zoom into the organic and inorganic building units. Colour code: M (blue), C (brown), O (red), H (white). Coordination environments are represented as blue polyhedra. Bottom: Schematic representation of the modified high-pressure X-ray reflectivity cell used for HP-PXRD measurements.

Experimental procedure

A powdered sample was filled into a Kapton capillary (1.0 mm diameter Kapton tube, bottom sealed with superglue) and silicone oil was added to the capillary as a non-penetrating PTM. This non-penetrating PTM ensures the complete transmission of the hydrostatic pressure to the powdered sample. In the case of MOF-74(M) the sample preparation was performed in a glovebox under Ar atmosphere to prevent any contact of the materials to moisture or air, so that the open metal sites remained unsaturated during sample preparation. Finally, the capillary was sealed with a metal sleeve to prevent water from entering. The thus prepared sample was introduced to the sample carrier (Fig. 1 bottom), which was transferred into the high-pressure cell at BL9. The cell was tightly sealed and the pressure was increased stepwise up to 4000 bar, whilst PXRD patterns were recorded at each pressure interval. A monochromatic X-ray beam of an energy of 27 keV was used. After integration of the MAR345 detector image, the change in the unit cell parameters of the crystalline materials was extracted from the PXRD patterns by sequential profile fitting (Pawley method)^[10].

Results

In a first step, we aimed on verifying the transmission of the water pressure to the powdered sample. Therefore, PXRD data of a sample containing LaB₆ and KBr ($m/m = 1:1$) and silicone oil (used as PTM) was collected in the full pressure range from ambient pressure up to 4000 bar. Due to the relatively low bulk modulus of KBr (14.2 GPa)^[11] and the pressure induced contraction of the unit cell, a shift in the reflection positions that are ascribed to KBr can be observed (Fig 2, left). Fitting the 2nd order Birch-Murnaghan equation of state (BMEOS)^[12] to the pressure dependent unit cell volume data provides a bulk modulus of 15.0 ± 0.3 GPa, which is in very good agreement with the literature value (Fig. 2, right). Hence, a calibration of the transmitted pressure was considered to be unnecessary.

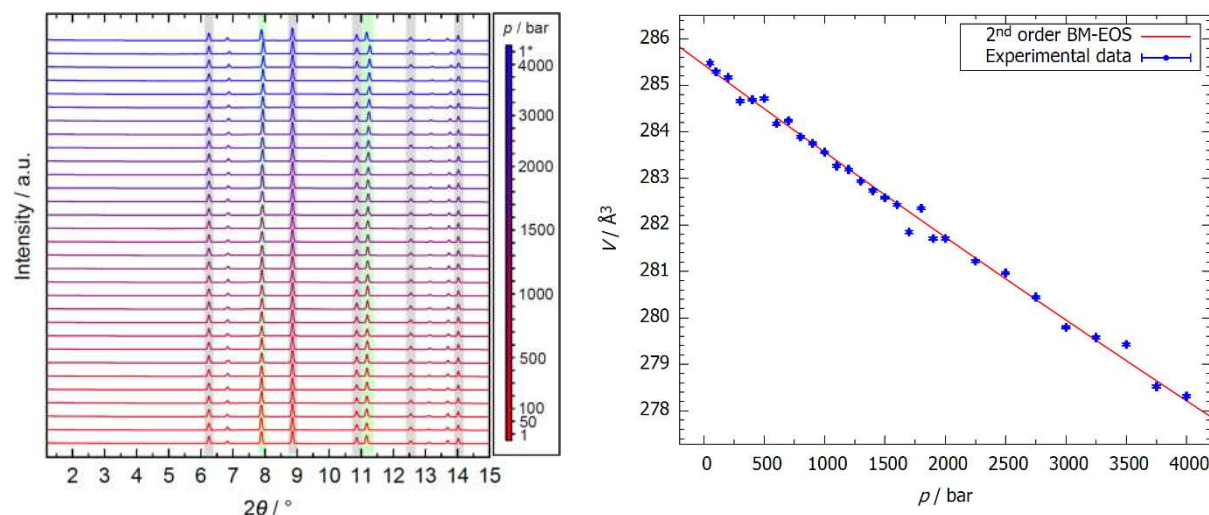


Figure 2: Left: Stacked plot of the powder diffraction patterns of KBr and LaB₆ ($m/m = 1:1$) in a pressure range from ambient pressure to 4000 bar. The star (*) marks the pattern recorded after returning to 1 bar. The green regions highlight the shift of two Bragg peak assigned to KBr. Right: Fit of the 2nd order BMEOS to the pressure dependent unit cell volume data of KBr extracted from the diffraction patterns by sequential profile fitting (Pawley method) providing a bulk modulus of $K_{\text{KBr}} = 15.0 \pm 0.3$ GPa.

Following this, various MOF-74(M) materials (with and without guest molecules) were investigated analogously. Again, as pressure increases the reflections shift to higher angles due to the contraction of the unit cell (see Fig. 3 for the diffraction patterns of MOF-74(Zn) as an

example). After the pressure reached 4000 bar an additional diffraction pattern was recorded after returning to ambient pressure. With this additional measurement it is possible to prove the reversibility of the volume contraction. The progression of the cell parameters obtained by sequential profile fitting (Pawley method) reveals that most MOF-74(M) derivatives preferentially contract along the crystallographic c axis presumably leading to a significant deformation of the metal ions' coordination environment. Preliminary data analysis demonstrates (i) that the bulk moduli of all investigated MOF-74(M) derivatives vary by more than a factor of 3 depending on the kind of M^{2+} ion in the structure, (ii) that K also largely depends on the amount of guest molecules present in the pores, and (iii) the emergence of irreversible pressure-induced strain in some MOF-74(M) materials as visualized by significant peak broadening in PXRD patterns recorded before and after pressure treatment (see Fig. 3 right). Further data collection and in-depth data analyses will be performed in the near future in order to get a full understanding of the supramolecular mechanics of MOF-74(M) crystals.

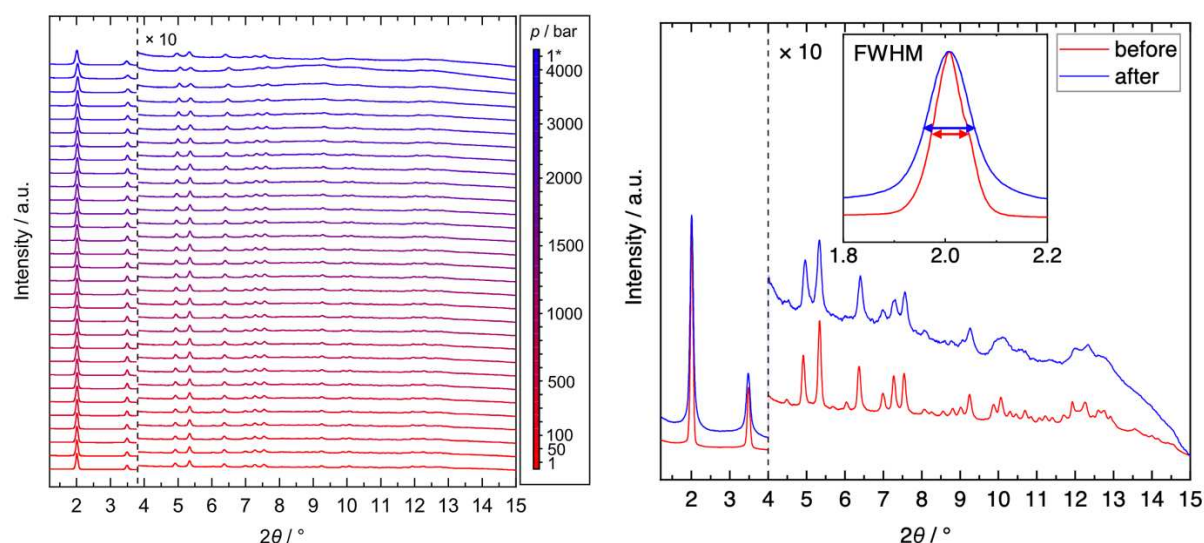


Figure 3: Left: Stacked powder diffraction patterns of MOF-74(Zn) in the range from ambient pressure to 4000 bar ($\lambda = 0.4537 \text{ \AA}$). The asterisk (*) marks the pattern recorded after returning to 1 bar. Right: Diffraction patterns of MOF-74(Zn) at ambient pressure before and after increasing the pressure to 4000 bar. The zoom into the first Bragg reflection demonstrates the increase of the FWHM.

In conclusion, we demonstrated the applicability of the available high-pressure X-ray reflectivity cell of BL9 for high-pressure PXRD in a pressure range up to 4000 bar. With a high energy monochromatic X-ray beam (27 keV), PXRD patterns with a quality sufficient for subsequent structural analysis by profile fitting can be routinely recorded even for weakly scattering samples, such as MOFs. In this first proof of concept study, we gained first insights into the structural evolution of an important series of MOF materials (i.e. MOF-74) under mechanical pressure. In future studies, we will focus on further improving the data quality by small changes in the sample preparation procedure as well as the setup itself.

The authors gratefully thank the DELTA team for their cooperation in modifying their high-pressure reflectivity setup and the beamline scientists at BL9, Dr. C. Sternemann and Dr. M. Paulus, for their outstanding support during the experiments.

References

- [1] B. Li, H. M. Wen, Y. Cui, W. Zhou, G. Qian, B. Chen, *Adv. Mater.* **2016**, *28*, 8819–8860.

- [2] S. Yuan, L. Feng, K. Wang, J. Pang, M. Bosch, C. Lollar, Y. Sun, J. Qin, X. Yang, P. Zhang, Q. Wang, L. Zou, Y. Zhang, L. Zhang, Y. Fang, J. Li, H. C. Zhou, *Adv. Mater.* **2018**, *30*, 1–35.
- [3] O. M. Yaghi, M. O’Keeffe, N. W. Ockwig, H. K. Chae, M. Eddaoudi, J. Kim, *Nature* **2003**, *423*, 705–714.
- [4] U. Mueller, M. Schubert, F. Teich, H. Puetter, K. Schierle-Arndt, J. Pastré, *J. Mater. Chem.* **2006**, *16*, 626–636.
- [5] P. D. C. Dietzel, R. Blom, H. Fjellvåg, *Eur. J. Inorg. Chem.* **2008**, 3624–3632.
- [6] H. Montes-Andrés, G. Orcajo, C. Mellot-Draznieks, C. Martos, J. A. Botas, G. Calleja, *J. Phys. Chem. C* **2018**, *122*, 28123–28132.
- [7] G. Calleja, R. Sanz, G. Orcajo, D. Briones, P. Leo, F. Martínez, *Catal. Today* **2014**, *227*, 130–137.
- [8] T. M. McDonald, W. R. Lee, J. A. Mason, B. M. Wiers, C. S. Hong, J. R. Long, *J. Am. Chem. Soc.* **2012**, *134*, 7056–7065.
- [9] F. J. Wirkert, M. Paulus, J. Nase, J. Möller, S. Kujawski, C. Sternemann, M. Tolan, *J. Synchrotron Radiat.* **2014**, *21*, 76–81.
- [10] G. S. Pawley, *J. Appl. Crystallogr.* **1981**, *14*, 357–361.
- [11] A. Dewaele, A. B. Belonoshko, G. Garbarino, F. Occelli, P. Bouvier, M. Hanfland, M. Mezouar, *Phys. Rev. B - Condens. Matter Mater. Phys.* **2012**, *85*, 1–7.
- [12] F. D. Stacey, B. J. Brennan, R. D. Irvine, *Geophys. Surv.* **1981**, *4*, 189–232.

Experimental report regarding proposal "Microfluidic-SAXS study on kinetics and mechanism of Aescin induced DMPC vesicle decomposition into nano-disks"

Proposal ID: 67

Beamline: BL9

Beamtime: 04.11.2019 – 06.11.2019

Principal investigator: Tim Julian Stank

Our experiment aimed at the aescin-induced conversion of small unilamellar 1,2-ditetradecanoyl-sn-glycero-3-phosphocholine (DMPC) vesicles into nanodisks. To investigate the structural conversion as a function of time, a special microfluidic chip was developed as a sample environment.

This microfluidic chip can be roughly divided into two parts. In the front section, the DMPC vesicle solution and the respective Aescin solution are fed into the chip via syringe pumps and mixed there by so-called TESLA mixing elements¹. The mixed sample then flows through the second section of the chip, which consists of a Kapton capillary. The capillary has an internal diameter of 166 μm and serves as a detection site for SAXS measurements. Since the age of the sample increases with the distance travelled in the microfluidic chip, it is possible to obtain time-resolved scattering curves of the sample by measuring at different positions along the capillary. In our experiments at BL9 two positions of the capillary were chosen as detection points. The first was about 3 mm behind the beginning of the so-called detection window, the second about 3 mm before the end of the detection window (see figure 1c). The respective positions were determined by x- and z-scans over the chip at channel height. In all measurements the beam size at the sample location was about 0.5 mm · 0.1 mm and the samples were examined at a wavelength of 0.9537 \AA (energy 13 keV). The sample-to-detector distance was 1066 mm, which was determined by a SAXS measurement of a silver behenate sample placed on the chip holder. This results in a q -range from 0.04 to 0.76 \AA^{-1} .

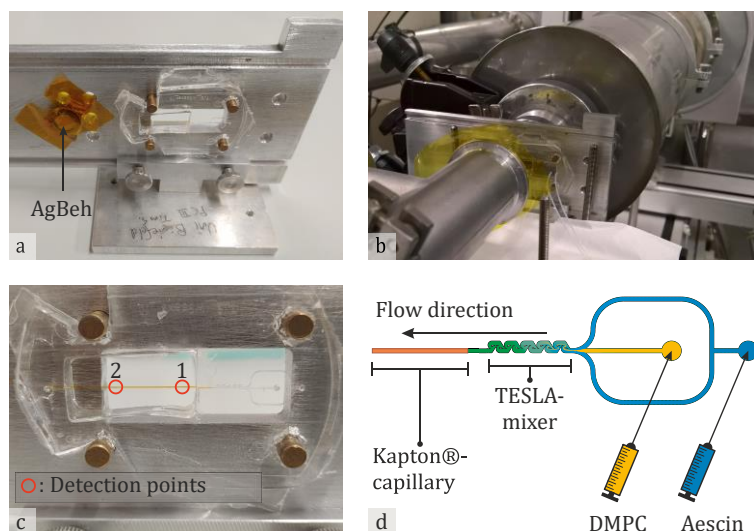


Figure 1: a) On the left side of the sample holder, the silver behenate is placed, on the right side the microfluidic chip is attached. b) The sample holder with our microfluidic chip is mounted on the stage of the beamline. The roughly marked detection points along the Kapton capillary are shown in c). The chip layout is illustrated in d).

fully developed at the time of the experiment. Therefore, it was not possible to perform measurements in the gel phase of the lipid.

As the scattering intensity of the sample hardly differed from the scattering intensity of the background, the first on-site evaluations of the data did not yield any meaningful scattering curves. This problem could be attributed to the small sample volume in the beam. Therefore, to record reference curves of our samples at 24.9°C we repeated the measurements with our Linkam stage as sample environment. Although the sample could only be examined in a static state without time resolution, the Linkam stage has a Kapton capillary with a diameter of 1 mm, which significantly improves the quality of the scattering data.

The samples were prepared freshly before the measurements by adding the respective aescin-containing buffer solution with a 1:1 volume ratio to the extruded lipid vesicles. Aescin contents of 0, 4, 5, 7, 12.5, 15, 20, 25 and 30 mol% (with

Both the freshly extruded 30 mg/mL DMPC vesicle solution and the respective aescin-containing buffer solution were pumped through the chip at 5000 $\mu\text{L/h}$ during the microfluidic SAXS measurements. Aescin solutions with aescin contents of 4 and 30 mol% (with respect to the total amount of DMPC and aescin of the mixed sample) were used.

At both detection positions, 3 scattering images were taken for each sample with an exposure time of 10 min for the mar345 image plate detector. For background determination, the solvent, 50 mM phosphate buffer (pH 7.4) was pumped through the chip and measured in the same way. As the chip could not be tempered, the measurements were carried out at room temperature of the hutch (24.9°C). This temperature is not ideal for the lipid used, as DMPC has the main phase transition from its gel to the liquid crystalline phase at about 23.6°C². An originally planned temperature control option for our microfluidic chip was unfortunately not yet

respect to the total amount of DMPC and aescin of the mixed sample) were used. Analogous to the microfluidic SAXS measurements, 3 scattering images were taken per sample with an exposure time of 10 min each.

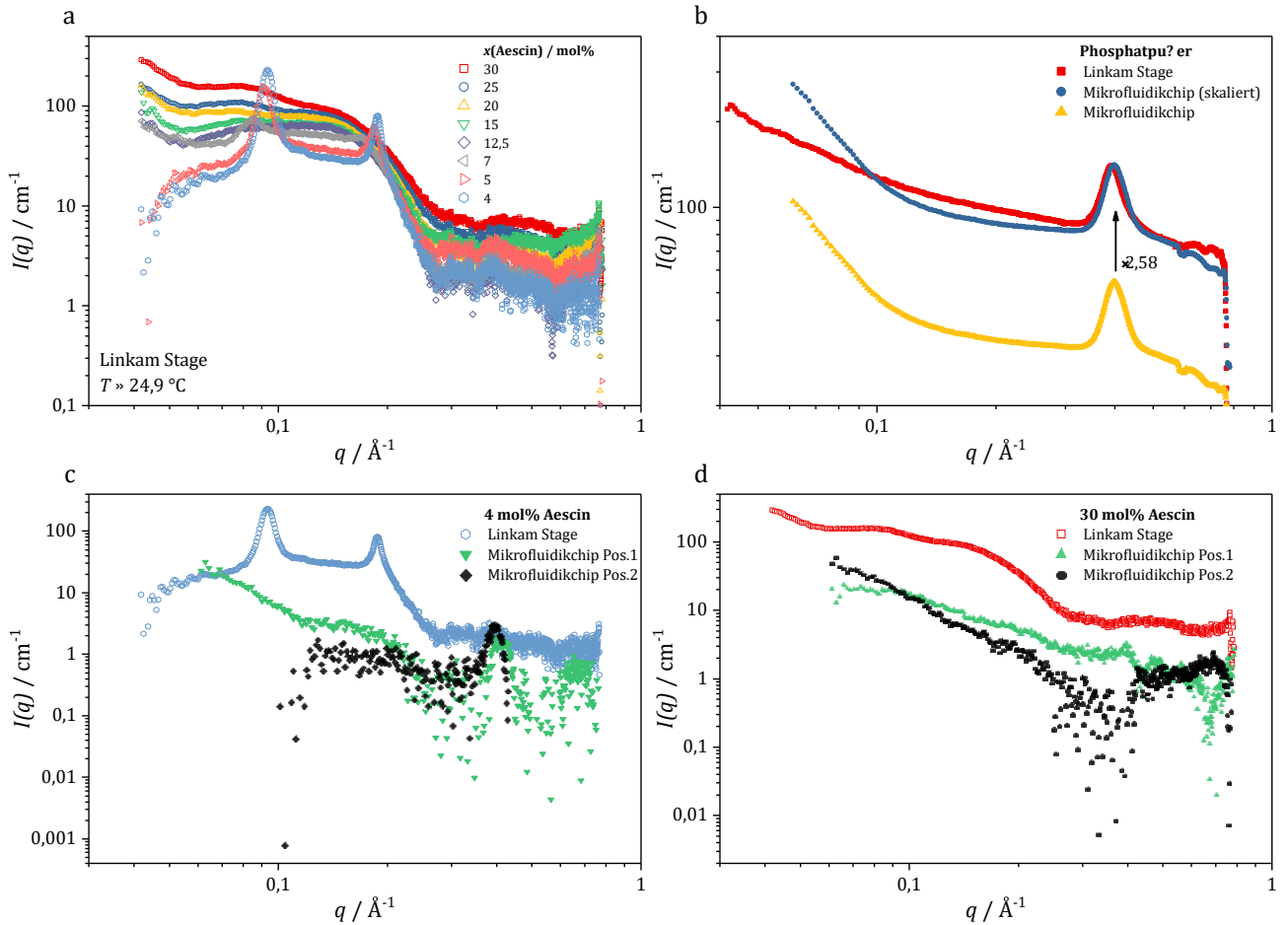


Figure 2: In a) individual scattering curves of the samples examined in the Linkam stage are plotted. b) shows the characteristic Kapton peak of the capillaries to which the scattering curves were scaled. In c) the scattering curves of the 4 mol% aescin containing sample recorded by a microfluidic chip are plotted against the reference measurement in the Linkam stage. The corresponding scattering curves of the 30 mol% aescin containing sample are shown in d).

Figure 2a shows the scattering curves of the samples measured in the Linkam stage. The scattering curves obtained from the microfluidic SAXS experiments are shown in Figure 2b-d. The scattering curves were each scaled to the Kapton peak of the background measurement of the Linkam stage (Figure 2b) since we had no other possibility for an absolute transmission normalisation. This Kapton peak occurs both in the Linkam stage Kapton capillary and in the microfluidic chip. Despite the normalisation, it was unfortunately not possible to compensate for the fluctuation in beam intensity of the synchrotron. The resulting difference in scattering intensity between the individual scattering images of a sample was so large, that it was not possible to determine the mean values of the scattering curves of the individual samples. The data shown in figure 2 are therefore not averaged curves, but rather one measured scattering curve of the respective sample.

The shape of the scattering curves of the measurements carried out with the Linkam stage (see figure 2a) closely match the curves of the same samples measured on our *inhouse* facility. Especially, the scattering curves of the samples with 4 and 5 mol% Aescin content show the characteristic Bragg peaks of those samples. Due to the limited q range, only the structure factor of the lipid membranes could be recorded, but the global size information could not be obtained from the scattering curves.

Similar scattering curves were expected for the samples investigated by microfluidic SAXS. However, as shown in Figure 2c and d, these scattering curves differ significantly from the reference measurements in the Linkam stage. This is mainly due to the small difference in the scattering density of sample and background, combined with the difference in the investigated volume. It should be emphasized that the beam size was smaller than the capillary of the Linkam stage but significantly larger than the Kapton capillary of the microfluidic chip. This had a major influence on the background reduction of those microfluidic SAXS measurements. Since an exact transmission normalisation of the data was not possible, the scattering intensity of the background was above that of the sample in some places, which resulted in partially “incomplete” scattering curves. Therefore, the data could unfortunately not be evaluated meaningfully. Based on the knowledge gained from the experiments, however, the sample holder and microfluidic chip could be optimised

with regards to the microfluidic SAXS measurements. The problems identified here during the measurements with our system could thus be avoided and/or corrected during recent microfluidic SAXS experiments on the microfocus beamline P03 at PETRA III (DESY, Hamburg).

We would like to thank DETA for the opportunity to perform these first microfluidic SAXS experiments. Special thanks to Dr. Michael Paulus and Dr. Christian Sternemann for the excellent support and help on-site.

References:

- (1) Hong, C.-C., Choi, J.-W., Ahn, C. H. A novel in-plane passive microfluidic mixer with modified Tesla structures. *Lab on a chip* **2004**, 4, 109–113.
- (2) Koynova, R., Caffrey, M. Phases and phase transitions of the phosphatidylcholines. *Biochimica et Biophysica Acta (BBA) - Reviews on Biomembranes* **1998**, 1376, 91–145.

Quaternary solid solutions of type $A'_x A''_{2-x} PdC_2$ (A', A'' : Na-Cs)

M. Krüger and U. Ruschewitz*

Department für Chemie, Universität zu Köln, 50939 Köln, Germany

*email: uwe.ruschewitz@uni-koeln.de

One of our long-term research interest focuses on the synthesis and characterization of ternary acetylides.^[1] Numerous ternary alkali metal transition metal acetylides have been reported by our group for d^{10} configured metals like Pd(0)^[2,3,4], Pt(0)^[2,3,4], Cu^{+[5]}, Ag^{+[6]} and Au^{+[7]}. Compounds of type A_2PdC_2 are semiconductors with very small indirect and larger direct bandgaps.^[8] Depending on the alkali metal A the size of the direct bandgap can be increased from 2.09 eV (A = Na) to 2.77 eV (A = Rb).^[8] To fine-tune these bandgaps we have now attempted to synthesize quaternary acetylides with the general composition $A'_x A''_{2-x} PdC_2$ (A', A'' : Na-Cs).^[9]

According to the Hume-Rothery rules substitutional solid solutions should be accessible, if both constituents have the same (or similar) crystal structures and valencies as well as similar electronegativities. All these requirements are fulfilled for acetylides of composition $A'_x A''_{2-x} PdC_2$, but the fourth rule requires that the unit cell volumes of both constituents should not differ by more than 15%. In Table 1 the respective values are summarized.

Table 1. Relative differences (%) of unit cell volumes of ternary acetylides of type A_2PdC_2 (A: Na-Cs).

| | | Na | K | Rb | Cs |
|-----------|-------------------------------|-----------|----------|-----------|-----------|
| | $V_{\text{cell}}(\text{Å}^3)$ | 90,87 | 119,25 | 131,50 | 145,09 |
| Na | 90,87 | 0,0 | | | |
| K | 119,25 | 23,8 | 0,0 | | |
| Rb | 131,50 | 30,9 | 9,3 | 0,0 | |
| Cs | 145,09 | 37,4 | 17,8 | 9,4 | 0,0 |

According to this table a complete solid solution series should be accessible for $K_x Rb_{2-x} PdC_2$ ($\Delta V = 9.3\%$) and $Rb_x Cs_{2-x} PdC_2$ ($\Delta V = 9.4\%$). Preliminary investigations on a 1:1 mixture of K_2PdC_2 and Rb_2PdC_2 confirmed that $KRbPdC_2$ is formed upon heating (SNBL/ESRF).^[9] At 250 °C the reaction starts, as indicated by broad and smeared-out reflections. Remarkably, 00l reflections remain almost unaffected and are still sharp. They coincide due to similar c lattice parameters in both acetylides. Obviously, the Pd–C and C–C bonds of the ${}^1_{\infty}[Pd^0(C_2)_{2/2}^-]$ chains do not break during the formation of quaternary $KRbPdC_2$ and the K^+ and Rb^+ cations move (by diffusion) between these chains. At 300 °C the formation of the quaternary acetylide was finished so that this temperature was chosen for all further experiments.

A more detailed analysis on different compositions $K_x Rb_{2-x} PdC_2$ ($x = 0-2$) was performed at BL9/DELTA and revealed an ideal Vegard behaviour for this solid solution (Figure 1), as expected from the values given in Table 1.

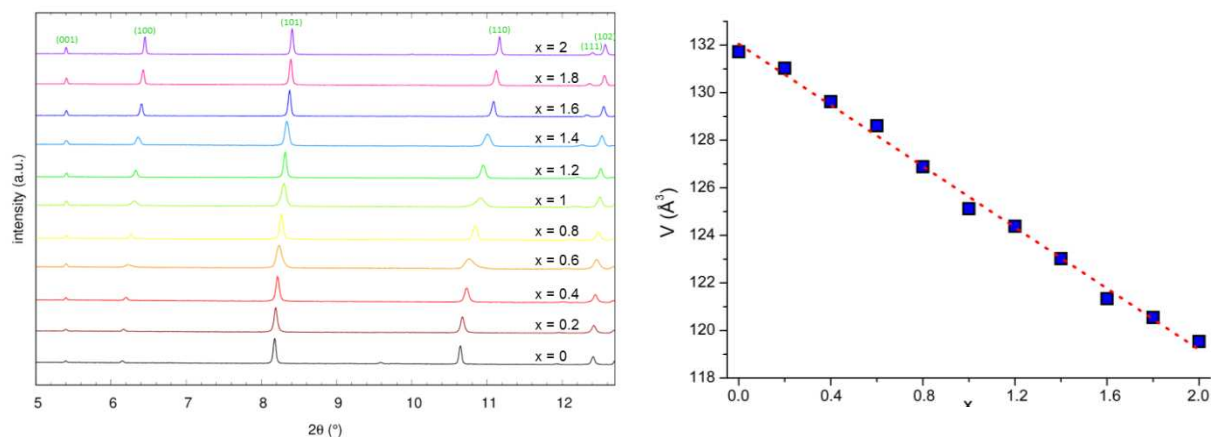


Figure 1. *Left:* Synchrotron powder diffraction patterns of $K_xRb_{2-x}PdC_2$ in dependence of x . *Right:* Unit cell volumes of $K_xRb_{2-x}PdC_2$ as obtained from Le Bail fits of synchrotron powder diffraction data (beamline BL9, DELTA; $\lambda = 0.49594 \text{ \AA}$) in dependence of the nominal composition x . The red dotted line is the result of a linear regression.

In ongoing investigations on $Na_xK_{2-x}PdC_2$ ($\Delta V = 23.8\%$) we found an only small solubility of little Na_2PdC_2 in K_2PdC_2 and vice versa. For $Na_xRb_{2-x}PdC_2$ ($\Delta V = 30.9\%$) we observed additional reflections after reacting Na_2PdC_2 and Rb_2PdC_2 at $300 \text{ }^\circ\text{C}$, which might be an indicator for cation ordering in this solid solution. Further investigations are under way.

- [1] U. Ruschewitz, *Z. Anorg. Allg. Chem.* **2006**, 632, 705.
- [2] M. Weiß, U. Ruschewitz, *Z. Anorg. Allg. Chem.* **1997**, 623, 1208.
- [3] S. Hemmersbach, B. Zibrowius, W. Kockelmann, U. Ruschewitz, *Chem. Eur. J.* **2001**, 7, 1952.
- [4] U. Ruschewitz, *Z. Anorg. Allg. Chem.* **2001**, 627, 1231.
- [5] U. Cremer, U. Ruschewitz, *Solid State Sci.* **2002**, 4, 247.
- [6] W. Kockelmann, U. Ruschewitz, *Angew. Chem.* **1999**, 111, 3697.
- [7] J. Offermanns, U. Ruschewitz, *Z. Anorg. Allg. Chem.* **2000**, 626, 649.
- [8] H. Billetter, T. Wallraff, U. Schwarz, R. I. Smith, U. Ruschewitz, *Z. Anorg. Allg. Chem.* **2010**, 636, 1834.
- [9] M. Krüger, S. Liebig, U. Ruschewitz, *Z. Anorg. Allg. Chem.* **2020**, 646, 570.

Temperature dependent x-ray diffraction study of ionic liquids and their polymerized counterparts

Mirko Elbers¹, Christian Sternemann¹, Philipp Münzner¹, Lena Friedrich¹, Michael Paulus¹, Jennifer Bolle¹, Metin Tolan¹ and Catalin Gainaru¹

¹Fakultät Physik/DELTA, TU Dortmund, 44221 Dortmund, Germany

Understanding the structural foundation governing the charge transport is the key for any rational design of electrochemical materials. In this respect, amorphous conductors such as ionic liquids (ILs) and polymer electrolytes are well investigated [1,2], at variance with the situation for the so-called polymerized ionic liquids (PolyILs). These electrolytes are prepared through direct covalent bonding of functional monomers containing IL fragments, hence combining the benefits of ILs in terms of high charge density with those of polymers in terms of mechanical stability.

In two recent works we analyzed the ionic diffusivity in several PolyILs by employing dielectric spectroscopy combined with nuclear magnetic resonance and differential scanning calorimetry [3,4]. Based on the results, we propose a new approach to estimate single-ion diffusivity from the conductivity relaxation by connecting the elementary diffusion step of the ions with structural details.

In order to check our estimates, we performed temperature dependent extended x-ray absorption fine structure experiments at BL10 of DELTA and P64 of PETRA III to probe the system on short length scales. These highly sensitive tests uncovered rather small temperature induced changes but an overall difference in the local environment surrounding the bromine anions in a polymer and monomer compound, respectively. To extend the framework of our findings to larger length scale, we investigated several ionic liquids and PolyILs with different chain lengths in a temperature range from 160 K to 400 K by x-ray diffraction (XRD) measurements. We performed the XRD experiments at beamline BL2 of DELTA with a wavelength of the incident x-ray beam of $\lambda = 1.14 \text{ \AA}$ and at a distance of 351 mm between sample and the MAR345 detector, leading to an accessible wave vector transfer of $0.2 \text{ \AA}^{-1} < q < 2.3 \text{ \AA}^{-1}$. The PolyILs and the monomer ionic liquids were measured in a custom-made sample holder and 0.7 mm thick capillaries, respectively. A beam size of $0.6 \times 0.6 \text{ (H x V) mm}^2$ was used for both sample holders. The samples were heated or cooled using a cryo jet setup. With an acquisition time of 10 minutes for each spectrum, we measured at least 14 different temperatures. The raw 2D detector images were azimuthally integrated and converted to the wave vector transfer scale q with DIOPTAS v.0.4.1 after using Lanthanum hexaboride for calibration. The average beam current during a measurement was used to normalize each diffraction pattern before subtracting the signal from an empty sample holder as background signal after further taken the absorption of the sample into account. A depiction of two of the four investigated samples is given in Fig.1.

The corresponding data obtained for Mono and Poly ImiBr are shown in Figure 1 on the left side. As observed here, the IL exhibit a strong peak between 1.5 \AA^{-1} and 1.75 \AA^{-1} as well as a distinct peak at lower q values between 0.25 \AA^{-1} and 0.5 \AA^{-1} , which is significantly more distinctive and narrower for the polymerized ionic liquid. The structural origins of the different

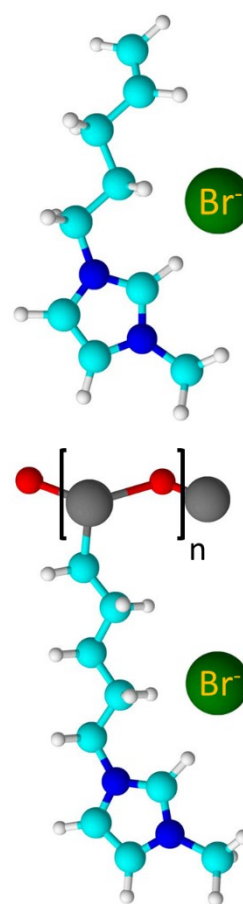


Figure 1: Two of the four investigated samples: the so-called ImiBr (1-Pentyl-3-methylimidazolium) monomer (upper image) and the corresponding polymer (lower image) as

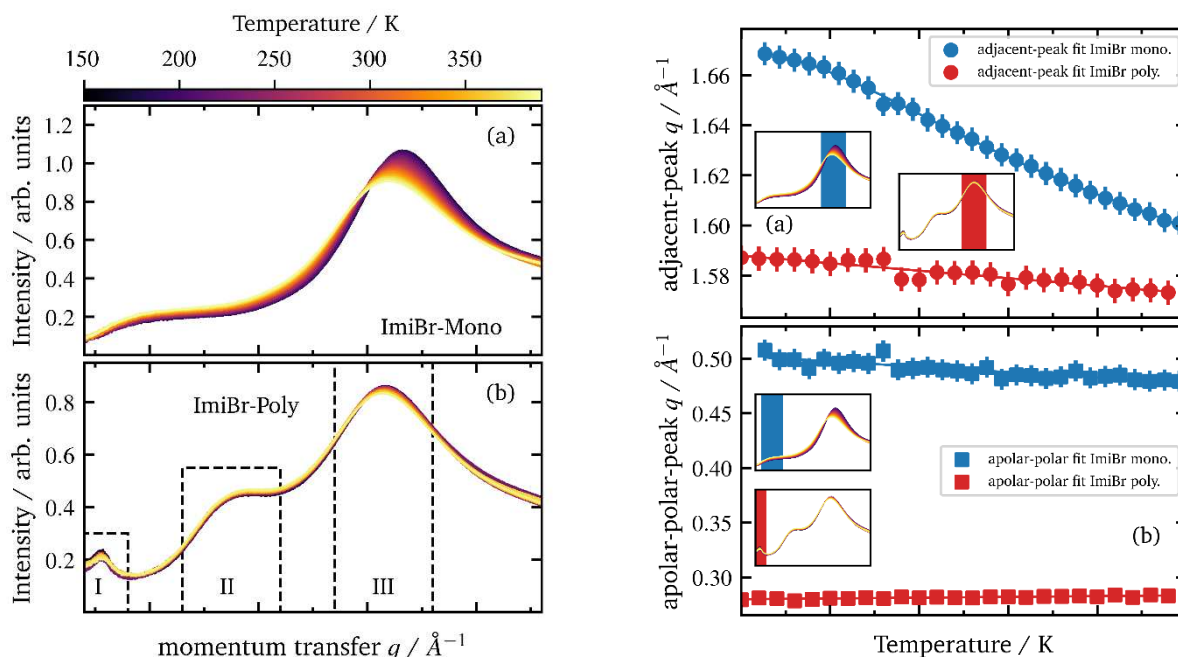


Figure 2: (left side) Normalized diffraction patterns of one of the investigated monomer (upper panes) and one of the polymerized (lower tow panels) ILs in a temperature range from 160K to 400K. The position of the three observable features are indicated in (b) by I:apolar-polar peak, II:charge-peak and III:adjacent-peak. (right side) Position of the adjacent peak (upper panel) and apolar-polar peak (lower panel) as a function of temperature, determined with a gaussian fit.

peaks are elaborate in Ref. [5]. In short, the low q -peak originates in a apolar-polar alternation and indicates a structural heterogeneity. The intermediate peak in Fig.2(left side,b) is the charge peak, which indicates charge alternation, but a missing charge peak is likely due to constructive interference between sub-components of the structure factor, since charge alternation is always present at room temperature. The high- q adjacent peak is not due to the ionic liquid nature of the sample but also occurs in molecules and monoatomic liquid. The polymerization of the sample causes a strong shift of the apolar-polar peak component in the diffraction pattern to lower values pointing towards a change in the structural arrangement of the apolar side chain. The monomer diffractograms exhibit a smaller polarity peak component, which might indicates a larger freedom of movement in the case of monomer IL and a lack of heterogeneity of the cation landscape. In order to quantify the changes with increasing temperature, we fitted a Gaussian function to the adjacent peak and, after subtracting a linear background, to the apolar-polar peak. The results of the fitting procedure are depicted in Fig.2 (right side) The increase in disorder with rising temperature can be observed in all systems as the intensity of the main peak decreases accompanied by a shift to lower q values. However, this effect is considerably weakened by the polymerization of the IL systems. The present results are currently considered in an extended analysis together with the dynamical aspects revealed by the conductivity investigations of these materials.

References: [1] Ratner, M., Johansson, P., & Shriver, D., Polymer Electrolytes: Ionic Transport Mechanisms and Relaxation Coupling, MRS Bulletin, 25(3), 31-37. (2000) [2] A. Rivera, T. Blochowicz, C. Gainaru, E. A. Rössler, Spectral response from modulus time domain data of disordered materials, J. Appl. Phys. 96, 5607 (2004) [3] C. Gainaru, E.W. Stacy, V. Bocharova, M. Gobet, A.P. Holt, T. Saito, S. Greenbaum and A.P. Sokolov, Mechanism of Conductivity Relaxation in Liquid and Polymeric Electrolytes: Direct Link between Conductivity and Diffusivity, J. Phys. Chem. B 120, 11074-11083 (2016) [4] Wieland F., Bocharova V., Münzner P., Hiller W., Sakrowski R., Sternemann C., Böhmer, R., Sokolov A., Gainaru C. "Structure and dynamics of short-chain polymerized ionic liquids" J. Chem. Phys. 151, 034903 (2019) [5] Juan C. Araque, Jeevapani J. Hettige, and Claudio J. Margulis J. Phys. Chem. B 119 (40), 12727-12740 (2015)

The effect of osmolytes and polymers on the lamellar to cubic transition dynamics of monoolein in excess water

Göran Surmeier, Michael Paulus, Eric Schneider, Marvin Kowalski, Metin Tolan and Julia Nase

Fakultät Physik/DELTA, TU Dortmund, 44221 Dortmund, Germany

Email: goeran.surmeier@tu-dortmund.de

The cells of living organisms are organized by membrane structures that are formed by amphiphilic lipids. They provide separation of the intra- and extracellular space and divide the cell interior into compartments and organelles. They do not act as static barriers but regulate the mass transfer via dynamic processes like budding and fusion, e.g., in endo- and exocytosis. The cellular environment is packed with various molecules like osmolytes, proteins, lipids, ribosomes, biopolymers, nucleic acids or carbohydrates. It is known that some of these substances can have considerable effects on the structure of lipid membranes [1] and that molecular crowding can induce membrane fusion and fission due to the excluded volume effect [2].

In this study, we examined the influence of urea, trimethylamine-*N*-oxide (TMAO), sucrose, and polyethylene glycol (PEG) on the dynamic behavior of monoolein after pressure-induced phase transitions. Monoolein is a lipid that forms inverse bicontinuous cubic phases in excess water at ambient conditions [3]. The structure of cubic phases resembles intermediates of membrane fusion and fission processes. Therefore, it is a valuable model system to study the effects of cellular solutes on membrane remodeling. Urea and TMAO are cellular solutes that are often found in a characteristic ratio of 2:1 in organisms that are exposed to high hydrostatic and high osmotic pressures. At this ratio, the denaturation effect of urea and the stabilizing effect of TMAO on protein structures compensate each other. Their different interactions with proteins translate into different effects on lipid structures. For example, the water content of cubic monoolein structures increases in presence of urea and reduces in presence of TMAO. Sucrose is an osmolyte that has weaker protein stabilizing properties than TMAO but can also decrease the hydration of lipid structures considerably. PEG is a polymer that is commonly used to simulate crowded environments [4]. Here, PEGs with molecular weights between 200 and 35000 g/mol were applied.

In this experiment, we induced the lamellar crystalline L_c to cubic $Pn3m$ phase transition of monoolein in excess water by an abrupt reduction of pressure. After the pressure jump, we monitored the sample structure with SAXS every four minutes for several hours. The phase and the corresponding lattice constant a can be determined from the scattering angles of diffraction fringes that occur in the SAXS patterns. The scattering angle α is connected to a momentum transfer $= \frac{4\pi}{\lambda} \sin \frac{\alpha}{2}$, with the wavelength λ of the used radiation. The fringes occur at specific multiples of the reciprocal lattice constant $\frac{2\pi}{a}$ that are characteristic for every given phase, e.g., $\sqrt{2}$, $\sqrt{3}$, $\sqrt{4}$, $\sqrt{6}$... for the cubic $Pn3m$ phase, and 1, 2, 3, 4 ... for lamellar phases. Based on the lattice constant, also the radius of the water channels r_w of cubic phases can be determined.

The experiment was performed at beamline BL2 at a photon energy of 12 keV applying the high hydrostatic pressure cell introduced by Wirkert et al. [5]. The incoming radiation was monochromatized by a multilayer monochromator. The beams size was set to 0.5 x

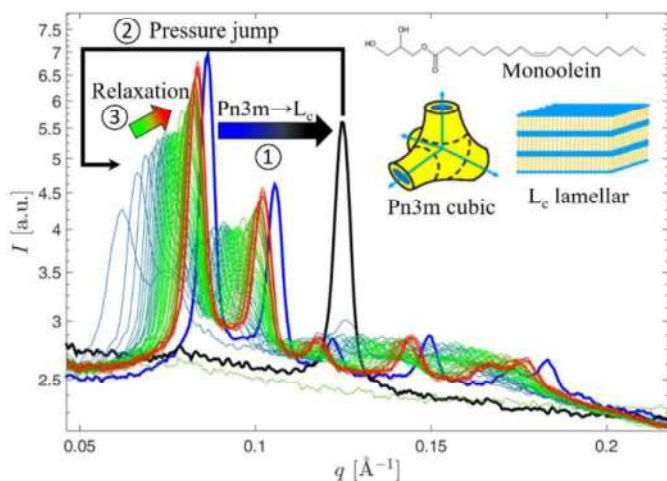


Figure 1: Integrated SAXS patterns of monoolein in the Pn3m phase at 50 bar at equilibrium (*blue curve*), in the lamellar phase at 1000 bar just before the pressure jump (*black curve*), and after the pressure jump down to 50 bar slowly approaching the initial state again (*green to red*).

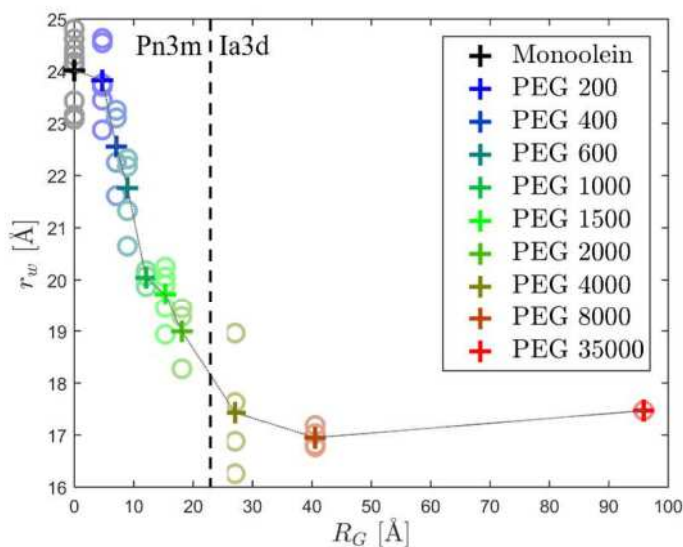


Figure 2: Radius of the Pn3m water channels r_w of monoolein as a function of the radius of gyration R_G of the added PEGs at 50 bar at equilibrium.

0.5 mm² by a slit system. A MAR345 image plate system was used for the detection of the scattered radiation.

Figure 1 illustrates the measuring procedure. To determine the equilibrium lattice constant, we recorded a SAXS image at 50 bar before we induced the cubic to lamellar phase transition by increasing the pressure. Then, we conducted a pressure jump from 1 kbar down to 50 bar. The Pn3m phase forms with a much higher lattice constant compared to equilibrium after a pressure jump-induced lamellar to cubic transition and decreases slowly over time.

Figure 2 shows how PEGs of different molecular weight at concentrations of 150 g/L modulate the Pn3m phase at equilibrium. The radius of the water channels decreases with increasing size of the polymers. At a certain point, a transition into the cubic Ia3d phase is induced. This phase is usually not observed at excess water conditions. It is known that the osmotic pressure exerted by PEGs at a given weight concentration reduces with increasing size of the polymers. Therefore, the increasing compression of the monoolein structures with increasing molecular weight indicates that the concentration gradient

between excess and hydration water changes. As the radius of the water channels of cubic monoolein phases is in the same order of magnitude like the radii of gyration of the examined PEGs, the ability of the polymers to insert into the cubic structures reduces strongly with the molecular weight and, thus, the osmotic pressure increases. In the Ia3d regime, the radii of gyration exceed the observed radii of the water channels. The pressure jump experiments showed that the dynamics after a lamellar to cubic transition are faster in presence of PEGs. The speed of the equilibration process increased with the molecular weight.

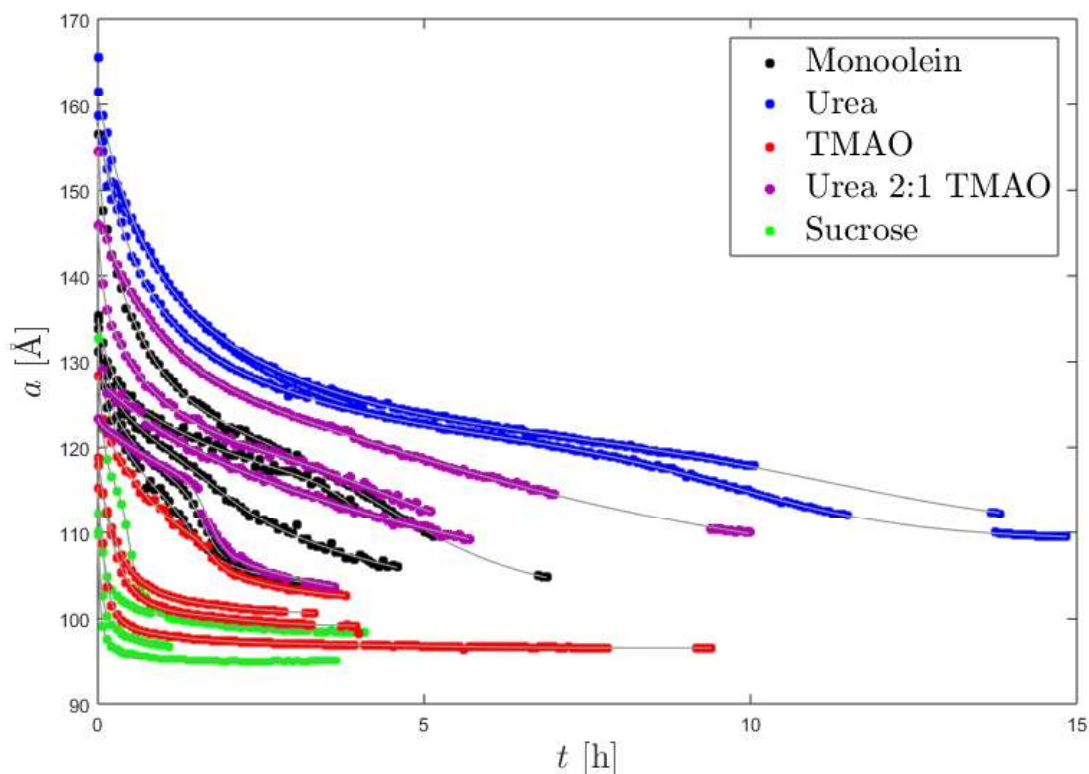


Figure 3: Relaxation of the Pn3m lattice constant a after a pressure jump from 1000 to 50 bar in absence (*black*) and presence (*coloured*) of different osmolytes.

The behavior of monoolein samples containing 1 M urea, TMAO or sucrose after a pressure jump is shown in figure 3. The dehydrating effect of TMAO and sucrose translates into faster dynamics while urea stabilizes swollen states. This can be explained by the affinity of urea to interact with lipid headgroups that promotes structures with large lipid-water interfaces and low negative curvature. In contrast, TMAO strongly interacts with water and is thereby displaced from membrane surfaces and from the interior of cubic phases. The resulting concentration gradient causes a pronounced osmotic pressure on cubic lipid structures.

Acknowledgments: This work is supported by the Forschergruppe 1979 (DFG-FOR1979). We also acknowledge the Delta machine group for providing synchrotron radiation and technical support.

References:

- [1] Sukenik, S., et al., *Physical Chemistry Chemical Physics* **19.44** (2017) 29862-29871.
- [2] Terasawa, H., et al., *Proceedings of the National Academy of Sciences* **109.16** (2012) 5942-5947.
- [3] Kulkarni, C.V., et al., *Physical Chemistry Chemical Physics* **13.8** (2011) 3004-3021.
- [4] Julius, Karin, et al., *Macromolecules* **52.4** (2019) 1772-1784.
- [5] Wirkert, F.J., et al., *Journal of Synchrotron Radiation* **21** (2014) 76.

Analysis of linear alcohols from methanol to 1-nonanol

Jennifer Bolle¹, Martina Požar², Christian Sternemann¹ and Aurélien Perera³

¹Fakultät Physik/DELTA, Technische Universität Dortmund, 44221 Dortmund, Germany

²University of Split, Faculty of Sciences, Ruđera Boškovića 33, 21000, Split, Croatia,

³Sorbonne Université, Laboratoire de Physique Théorique de la Matière Condensée (UMR CNRS 7600), 4 Place Jussieu, F75252, Pariscedex 05, France.

The microstructure of monohydroxy alcohols (MA) is largely dependent on the formation of hydrogen bonds and the spatial restrictions imposed by the flexible carbon chains. In order to study the microscopic structure of alcohols we used a combination of X-ray diffraction (XRD) and molecular dynamics simulations to investigate linear alcohols with increasing chain length from methanol to 1-nonanol. We compared the measured scattering intensities with those calculated from structures obtained by molecular dynamics simulations using different force fields. Special attention is paid to the origin of the known pre-peak observed in the low momentum transfer range of the scattering pattern.

The XRD measurements were performed at the beamline BL2 of the synchrotron light source DELTA (TU Dortmund, Dortmund, Germany). The MAs were used without further treatment and were filled in borosilicate capillaries with 3.5 mm diameter. The measurements were performed at an incident photon energy of 11 keV and the diffraction data were recorded using a MAR345 image plate detector. The 2D diffraction images were integrated with the program package Fit2D [1] and converted to wave-vector transfer q scale. All diffraction patterns were normalized to the mean integral of the calculated diffraction patterns in the q -range of 0.2 to 2.3 \AA^{-1} . The experimental X-ray scattering intensities $I(q)$ are presented in Fig.1 as dashed lines showing two characteristic scattering maxima. The main peak occurs at higher momentum transfer ($1.4 \text{\AA}^{-1} < q < 1.75 \text{\AA}^{-1}$) and the so-called pre-peak at lower q ($0.3 \text{\AA}^{-1} < q < 1 \text{\AA}^{-1}$). Both diffraction maxima exhibit distinct dependency on chain length. While the main peak shifts to lower q with increasing chain length up to 1-propanol and then hardly changes position, the pre-peak's position decreases for the entire series of linear alcohols. Interestingly, the pre-peak's intensity increases with smaller alcohols, up to a maximum for 1-butanol and then decreases systematically. While the main peak is commonly related to atom-atom correlations the pre-peak contains information on the larger-scale microstructure of the liquids.

To extract information on the structure formation from the scattering intensities, they are compared with $I(q)$ calculated from structures obtained with different force fields, i.e. OPLS (Optimized Potentials for Liquid Simulations), TraPPE (Transferable Potentials for Phase Equilibria), CHARMM (Chemistry at Harvard Macromolecular Mechanics), and to

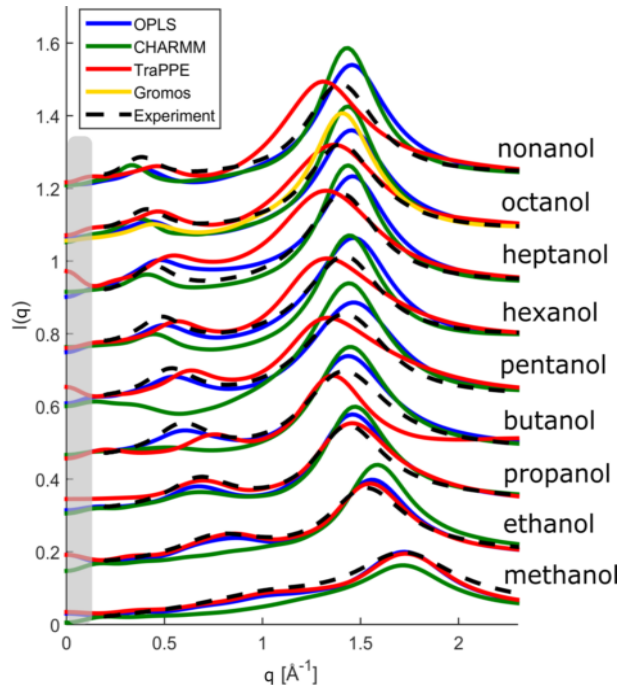


Figure 1: Experimental and calculated X-ray scattered intensities for alcohols from methanol to 1-nonanol with the the experimental diffraction patterns (black dashed lines), OPLS (blue), TraPPE (red), CHARMM (green), GROMOS (gold) [2].

some extent the GROMOS. The results are compared to the experiment in Fig.1. The grey area represents the small q -area, where the errors from the simulations influence the calculated $I(q)$. Although the main peak is well reproduced by all models the pre-peak shows a strong dependence on the kind of model used. Overall by comparing experiment and theory, the OPLS-UA model has the best agreement with the experimental data. Analysis of the model structures reveal various types of supramolecular arrangements for alcohols with $n>2$, where n is the length of the carbon chain. Most prominent are transient clusters made of 4 to 5 molecules besides monomers.

The position of the pre-peak is indicative for the size of these meta-objects which strongly depends on the alky tails. The intensity behavior of the pre-peak can be understood in terms of cancellations of atom-atom structure factor contributions. Here the interplay between correlation of charged head groups and crosscorrelations of head and uncharged tail groups give rise to intensity variation of the pre-peak which is then strongly affected by domain ordering and the flexibility of the alkyl chains. Details of this analysis can be found in Ref. [2].

Reference

- [1] Hammersley, A., Svensson, S., Hanfland, M., Fitch, A. & Hausermann, D. (1996). International Journal of High Pressure Research, 14, 235–248.
- [2] Pozar, M., Bolle, J., Sternemann, C., & Perera, A. (2020). On the X-ray Scattering Pre-peak of Linear Mono-ols and the Related Microstructure from Computer Simulations. The Journal of Physical Chemistry B, 124(38), 8358-8371.

Acknowledgement

We would like to thank the DELTA machine group for providing synchrotron radiation and technical support, Michael Paulus for helping with the X-ray diffraction experiments at beamlines BL2. We would also like to thank Lena Friedrich and Pia-Victoria Pottkämper for their assistance with the measurements.

Charge carrier transport induced by x-ray radiation - role of the semiconductor (part 2)

Hanna Makowska¹, Okan Yildiz², Wojciech Pisula^{1,2} and Tomasz Marszalek^{1,2,*}

¹ Department of Molecular Physics, Faculty of Chemistry Lodz University of Technology, Zeromskiego 116, 90-924 Lodz (Poland)

² Max Planck Institute for Polymer Research, Ackermannweg 10, 55128 Mainz, Germany

* Email: marszalek @mpip-mainz.mpg.de

Organic electronics have become attractive for practical applications in complementary logic circuits due to unique features of organic semiconductors such as solution-processability and large-area manufacturing. Bulk heterojunctions (BHJ), consisting of a blend of two organic semiconductors of different electronic affinities, allow the fabrication of a broad range of devices such as light-emitting transistors, light-emitting diodes, photovoltaics, photodetectors, ambipolar transistors and sensors.

During our beam time at the BL9 of the DELTA electron storage ring in Dortmund in 2019-2020 we performed an investigation: a) to switched charge carrier transport from electron to hole domination [1] and b) of photovoltaic and charge transport parameters in the ambipolar semiconductors on the specific molecular structure [2], upon various processing and post-treatment. In both described projects a role of the inner nano-morphology on charge carrier transport were analysed with grazing-incidence wide-angle X-ray scattering (GIWAXS). Application of the GIWAXS data (Figure 1), combined with complementary technics (atomic force microscopy, transmission electron microscopy and theoretical calculation) allow to significantly improve and control uni- and ambipolar charge carrier transport in BHJ structures.

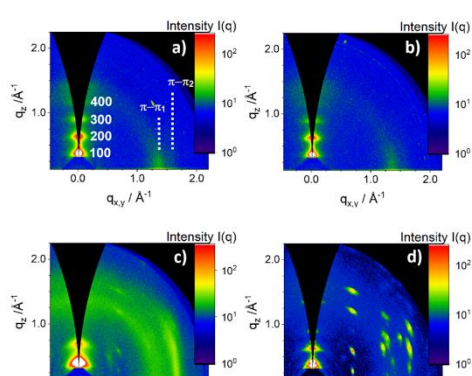


Figure 1. GIWAXS patterns of PBTTC-C₁₄ spin coated at 3000 rpm from a 100 °C hot solution a) before and b) after annealing at 200 °C and PBTTC-C₁₄:PD18-CN₂ spin coated at 3000 rpm from solution at 100 °C c) before and d) after annealing at 200 °C. Numbers in the pattern (a) denote the peaks corresponding to h00 Bragg series of PBTTC-C₁₄.

Acknowledgement

This work was partially prepared as part of the „Self-standing, flexible and solution processable organic field effect transistors for complementary inverter applications” project that is carried out within the First Team programme of the Foundation for Polish Science co-financed by the European Union under the European Regional Development Fund (POIR.04.04.00-00-3ED8/17-01). W.P. acknowledges the National Science Centre, Poland, through the grant UMO-2015/18/E/ST3/00322. The researchers involved in these projects express their gratitude to Dr. Christian Sternemann and Dr. Michael Paulus for their help in the experiments.

References

- 1) Sebastian Lucas, Jochen Kammerer, Martin Pfanmüller, Rasmus R. Schröder, Yakun He, Ning Li, Christoph J. Brabec, Tim Leydecker, Paolo Samorì, **Tomasz Marszalek**, Wojciech Pisula, Elena Mena-Osteritz, Peter Bäuerle, „Molecular Donor-Acceptor Dyads for Efficient Single Material Organic Solar Cells”, *RRL Solar*, **2020**, <https://doi.org/10.1002/solr.202000653>.
- 2) Julia Fidyk, Witold Waliszewski, Piotr Sleczkowski, Adam Kiersnowski, Wojciech Pisula and **Tomasz Marszalek**, „Switching from Electron to Hole Transport in Solution-Processed Organic Blend Field-Effect Transistors”, *Polymers*, **2020**, *12*, 2662.

Hard X-ray spectroscopy

EXAFS investigations of nitrogen-treated niobium foils

P. Rothweiler, R. Wagner, J. Klaes, B. Bornmann, D. Lützenkirchen-Hecht

Fakultät 4-Physik, Bergische Universität Wuppertal, Gaußstr. 20, 42097 Wuppertal, Germany

The exposure of Nb-materials to dilute N₂-atmospheres at temperatures around 800 °C has been proven to be profitable for the superconducting properties of Nb in accelerating structures. Such a nitrogen-doping results in a substantial lowering of the surface resistance and an improvement of the quality factor of the cavities (see e.g. ref. [1-4]). In general, those heat-treatments have to be performed in a clean environment, because Nb, as a valve-metal, has a high affinity towards oxidation in particular at elevated temperatures. From literature, it is well-known that oxygen occupies octahedral interstitial positions within the bcc-host lattice of niobium [5-7]. In contrast, however, there is an ongoing discussion about the position of nitrogen dissolved within the Nb-lattice. Similar as for oxygen, the octahedral interstitial site appears to be favourable [4, 8-10]. We have therefore initiated ongoing activities using in-situ and ex-situ EXAFS experiments in order to understand the processes of nitrogen-doping at high temperatures in more detail [11-13]. EXAFS may provide details of the short range order structure such as coordination distances, coordination numbers and the local disorder, and it also allows to determine the chemical valence of the X-ray absorbing atoms [14], making this technique ideal for studies of N₂-doping processes as well.

In-situ sample preparation was performed in a dedicated, remote controlled vacuum chamber with a base pressure of about 10⁻⁶ mbar, employing a ceramic heating plate suited for temperatures of up to 1200 °C and heating rates of more than 500 °C/minute [15]. Sample preparation included a vacuum annealing for 1 h at 900 °C, and the subsequent exposure to 6.0 N₂-gas with a pressure in the range from approximately 1 mbar to 30 mbar, under a variation of the exposure time. EXAFS data at the Nb K-edge (18986 eV) were collected in transmission mode prior to any heat treatment, during the different process steps at elevated temperatures as well as after cooling to room temperature. In order to improve the accessible data quality, the samples were also measured after cooling down to liquid nitrogen temperatures, thereby reducing the thermal disorder within the samples, leading to substantially increased amplitudes of the EXAFS oscillations [14]. All the experiments presented here were performed at the wiggler beamline 8 of the DELTA storage ring (Dortmund, Germany) [15].

For the data analysis, the EXAFS oscillations $\chi(k)$ were extracted from the experimental data employing standard routines available in the Athena/Artemis software package [16]. In a second step, the data in the radial range of the first two coordination shells between 1.5 Å ≤ R ≤ 3.5 Å in the Fourier-transform was transformed back into k-space, and fitted with phases and amplitudes calculated by FEFF [17] assuming the presence of a body-centered-cubic lattice with a lattice parameter of 3.30 Å as a starting parameter. The distances R₁ and R₂ of the first two Nb-Nb shells as well as the related mean squared displacements σ_1^2 and σ_2^2 were then treated as free fit parameters, along with inner potential shift ΔE_0 and the amplitude reduction factor S₀² as global parameters. More details of the fit procedures will be given in a forthcoming publication [18].

The Nb-Nb bond distances obtained for R₁ and R₂ are slightly increasing with an increasing nitrogen expose, measured as the product of the applied nitrogen pressure and the exposure time at 900 °C, as can be seen in Fig. 1. Furthermore the disorder parameters (σ_1^2 and σ_2^2) seem to increase with N₂-exposure also, however with a larger scatter of the data points. The continuous increase of both Nb-Nb bond lengths with increasing N₂-exposure can be explained by an increasing occupation of octahedral vacancy sites by N-atoms, leading to a slight expansion of the host lattice with N₂-exposure. In particular, as this octahedral vacancy is located directly between the second nearest Nb-neighbours in a distance R₂, the increase of R₂ with N₂-exposure, i.e. the slope in Fig. 1, is larger than that of R₁, in close agreement with the fit results. Furthermore, the increasing uptake of nitrogen in the Nb-lattice should also lead to a substantial increase of the (static) disorder (σ_1^2 and σ_2^2), in accordance with the fit results. The presented data validate the results of previous measurements that have been carried out at room temperature [11]. In conclusion, the location of nitrogen on octahedral lattice sites within the Nb-lattice is very likely.

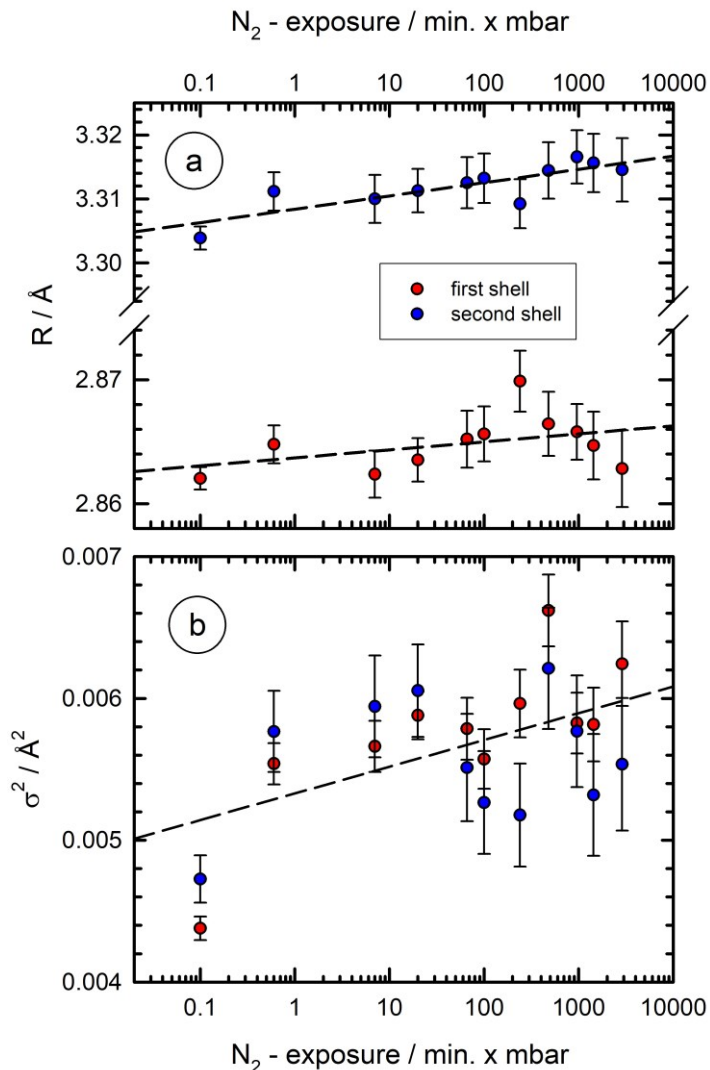


Fig. 1: Results of EXAFS data fitting procedures of Nb-foils heat-treated in N_2 atmospheres at 900 °C for different pressures and times as a function of the N_2 -exposure, i.e. the product of the N_2 -pressure and the time of the treatment in N_2 at 900 °C. After the preparation at elevated temperatures, the samples were cooled to room temperature under vacuum, and then to liquid nitrogen temperature (ca. 80 K) in a cryostat. These efforts were made to reduce thermal lattice vibrations and to thereby increase the accuracy of the fit results. (a) Plot of the distances of the first two Nb-Nb coordination shells (R_1 , R_2). The dashed trend lines show the increase of the determined bond distances with N_2 -exposure. Note that the slope of the regression line is larger for R_2 in comparison to that for R_1 . (b) Mean squared displacements (σ_1^2 , σ_2^2) with a common trend line for both shells. See text for more details.

Acknowledgement

We gratefully acknowledge the DELTA machine group for providing synchrotron radiation reliably. The study was financially supported by the BMBF under projects No. 05H15PXR1 and 05H18PXR1.

References

- [1] A. Grassellino, et al., *Supercond. Sci. Technol.*, 26 (2013) 102001.
- [2] D. Gonnella & M. Liepe, *Proc. IPAC 14 (JACoW, Dresden, Germany, 2014)*, pp. 2634. <https://doi.org/10.18429/JACoW-IPAC2014-WEPR1064>.
- [3] D. Gonnella, et al., *J. Appl. Phys.* 117 (2015) 023908.
- [4] A. Dangwal Pandey, et al., *J. Mater. Sci.* 53 (2018) 10411.
- [5] P. Kofstad. *High temperature oxidation of metals*. John Wiley & Sons, New York, 1966.
- [6] M.S. Blanter & A.G. Khachatryan, *Metal. Trans. A* 9 (1978) 753.
- [7] H. Dosch, et al., *Phys. Rev. B* 34 (1986) 1654.
- [8] J.T. Clenny & C.J. Rosa, *Metal. Trans. A* 11 (1980) 1575.
- [9] U. Schubert, et al., *J. Phys. F: Metal Phys.* 14 (1984) 2457.
- [10] T.H. Metzger, et al., *J. Phys. F: Metal Phys.* 15 (1985) 779.
- [11] J. Kläs, et al., *DELTA annual report (2018)* 131.
- [12] P. Rothweiler, et al., *DELTA annual report (2019)* 91.
- [13] P. Rothweiler, *Master-thesis*. Bergische Universität Wuppertal (2020).
- [14] D. Koningsberger & R. Prins, *X-ray absorption: principles, applications, techniques of EXAFS, SEXAFS, and XANES*. John Wiley and Sons; New York, 1988.
- [15] D. Lützenkirchen-Hecht, et al., *J. Synchrotron Rad.* 16 (2009) 264.
- [16] B. Ravel & M. Newville, *J. Synchrotron Radiat.* 12 (2005) 537.
- [17] A.L. Ankudinov, et al., *Phys. Rev. B* 58 (1998) 7565.
- [18] J. Klaes, et al., *J. Synchrotron Rad.* 21 (2021), in print.

EXAFS investigations of ZnO nanoparticles

A. Šarić^a, F. Eckelt^b, M. Vrankić^a, D. Lützenkirchen-Hecht^b, R. Wagner^b

a) Division of Materials Physics, Centre of Excellence for Advanced Materials and Sensing Devices, Ruđer Bošković Institute, Bijenička 54, 10000 Zagreb, Croatia.

b) Bergische Universität Wuppertal – Fakultät für Mathematik und Naturwissenschaften, Gauß-Str. 20, 42097 Wuppertal, Germany.

Due to their interesting physico-chemical properties, ZnO nanoparticles are of potential interest for many applications in various fields. Just to mention a few, ZnO is well-suited for applications in lasers, solar cells [1], field emitter arrays [2], capacitors, anti-bacterial coatings [3], mechanical actuators and piezoelectric sensors [4], etc. The chemical stability and high photostability are useful prerequisites for the use of ZnO as a (photo-) catalyst [5, 6]. Here we want to investigate the structure of zinc oxide nanoparticles prepared by a simple hydrolysis of zinc acetylacetonate monohydrate ($\text{Zn}(\text{acac})_2 \cdot \text{H}_2\text{O}$). A typical synthesis comprised the dissolution of a well-defined amount of zinc acetylacetonate monohydrate ($\text{Zn}(\text{acac})_2 \cdot \text{H}_2\text{O}$) in aqueous NaOH solution [7]. The transparent precursor solutions were autoclaved at 90 °C for 24 h, the obtained precipitates were subsequently separated from supernatants by centrifugation, washed several times with ethanol, and finally dried for the X-ray investigations. The powders were thoroughly mixed with suited amounts of boron nitride and dispersed on self-adhesive paper. Several ZnO-covered tapes were stacked and measured in transmission mode in the vicinity of the Zn K-edge (9659 eV). The EXAFS experiments have been performed at DELTA beamline 10, using a Si (111) channel-cut monochromator [8], employing N_2 -filled ionization chambers for the incident, and Ar-filled ionization chambers for the transmitted beam, respectively. Repeated scans each of typically 30 minutes acquisition time were performed and averaged. An exemplary data file suited for a detailed EXAFS analysis is presented in Fig. 1, together with the morphology of the samples as measured using scanning electron microscopy. Here, small needle-like features with a diameter in the range of ca. 100 nm and an average length of several μm are detectable.

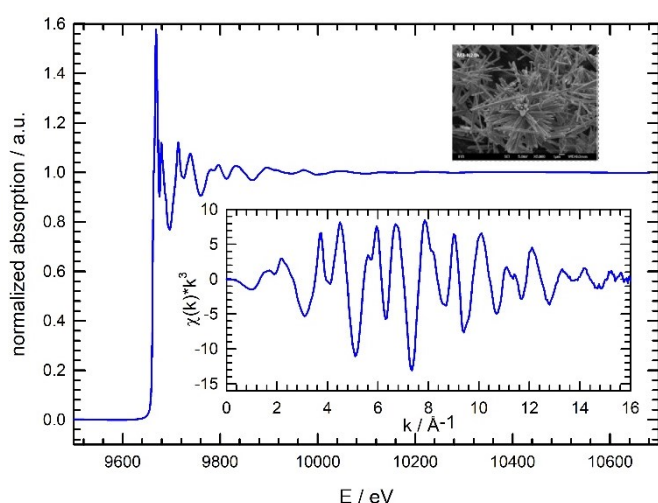


Fig. 1: Zn K-edge X-ray absorption data of a nanosized ZnO material. In the lower insert, the extracted and k^3 -weighted EXAFS fine structures $\chi(k) \cdot k^3$ are shown. In the upper insert, a scanning electron microscopy (SEM) image of the sample is given.

First of all it should be noted that the measured edge position is well in agreement with Zn^{2+} for all investigated samples, and no distinct differences of the XANES were detected, which is well in agreement with X-ray diffraction results, which clearly indicate the presence of wurtzite-type ZnO [7]. However the Fourier-transforms of the samples show subtle differences, with different

contributions from the first Zn-O shell at about 1.6 Å and Zn-Zn at ca. 2.9 Å (see Fig. 2). For the EXAFS data evaluation, we have performed fits assuming the hexagonal (wurtzite) space group No. 186 (P63mc) with $a = b = 3.289\text{Å}$, $c = 5.307\text{Å}$ and $\alpha = \beta = 90^\circ$, and $\gamma = 120^\circ$, respectively [9]. All atoms up to a radius of 4.7 Å were considered for the fit here, resulting in a cluster of 39 atoms in total.

In principle, each of the resulting coordination shells (i) is characterized by its distance R_i , the number of atoms in the shell (N_i), the amplitude reduction factor ($S_{0,i}^2$), the inner potential shift (ΔE_{0i}) and the mean square displacement (σ_i^2), so that, if all these shells were considered individually, a huge and statistically insignificant number of fit variables would result. From the energy range covered by the experiment and the R-range in the FT, the limit for the number of fit variables (N_{idp}) can be estimated, giving a maximum of 25 statistically justifiable fit variables here. Thus, for the modelling, we have developed a model with a substantially smaller number of fit variables, i.e. we have varied the distances R_1 (i.e. Zn-O) and R_2 (i.e. Zn-Zn) individually in order to detect small change of the first and second neighbor bonds more sensitively, while all other distances were fitted with a single scaling factor α , so that the fitted distance is $R_{\text{eff}} \cdot \alpha$, R_{eff} being the distance calculated from the original crystal structure (see above). All Zn-O coordinations were fitted using the same σ_{O}^2 and Zn-Zn with σ_{Zn}^2 . For multiple scattering pathways, the average values of the respective shells were used. The same approach was used for the amplitude reduction factors $S_{0,i}^2$, i.e. all Zn-O shells and Zn-Zn shells were weighted with the same values for $S_{0,i}^2$, respectively, and multiple scattering paths were again weighted according to the involved atoms, using the number of atoms N_i according to the hexagonal structure. In order to minimize the influence of the correlation of the inner potential shift (ΔE_{0i}) and all the distances, we have used the same value for ΔE_0 for all samples and all shells, using a value of $\Delta E_0 = 4.888 \pm 0.748$ eV. In total, only 7 variables are needed for the optimization of the EXAFS data for each sample. A typical fit result is shown in Fig. 2, proving the opportunity to model the data successfully. Ongoing work is related to the systematic fitting of several, differently prepared ZnO nanoparticles and a correlation of the derived structural details to physico-chemical properties, in particular the degradation of organic dyes.

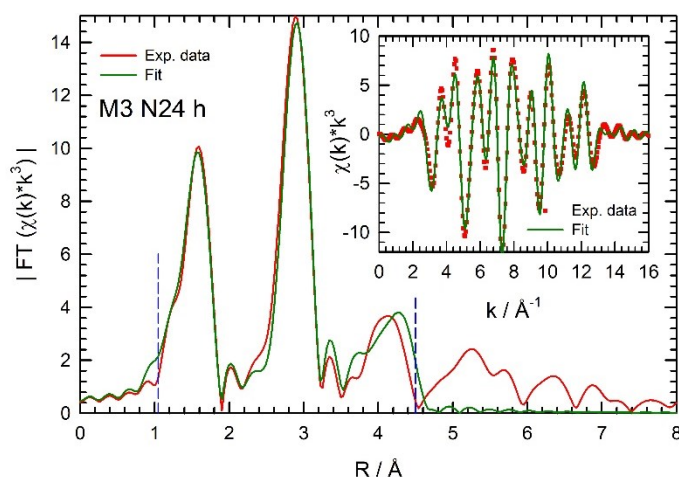


Fig. 2: Example of an EXAFS fit of a ZnO nanoparticle sample in R- and k-space. The k-range from $k_{\text{min}} = 2.540 \text{Å}^{-1}$ to $k_{\text{max}} = 14.342 \text{Å}^{-1}$ (see Fig. 1) was used for the Fourier-transform, and the R-range from $R_{\text{min}} = 1.1 \text{Å}$ to $R_{\text{max}} = 4.5 \text{Å}$ (vertical dashed lines) was optimized in the fitting procedure.

References:

- [1] W. Dongting, Z. Xuehong, F. Yuzhen, et al., Nano-Structures & Nano-Objects 10 (2017) 1.
- [2] X. Wang, L. Wang, X. Bai, et al., Proc. 33rd International Vacuum Nanoelectronics Conference 2020, DOI: 10.1109/IVNC49440.2020.9203549.
- [3] M. Shaban, F. Mohamed & S. Abdallah. Sci. Rep. 8 (2018) 3925.
- [4] A. Kumar, M. Prasad, V. Janyani, et al., Microsyst. Technol. 25 (2019) 4517.
- [5] G. Marč, V. Augugliaro, M.J. López-Muñoz, et al., J. Phys. Chem. B 105 (2001) 1033.
- [6] S. Singh, M. Joshi, P. Panthari, et al., Nano-Structures & Nano-Objects 11 (2017) 1.
- [7] S. Musić, A. Šarić, Ceram. Int. 38 (2012) 6047.
- [8] D. Lützenkirchen-Hecht, R. Wagner, S. Szillat, et al., J. Synchrotron Rad. 21 (2014) 819.
- [9] <https://materialsproject.org/materials/mp-2133/>

EXAFS investigations of electrodeposited Co-hydroxide layers

L. Voss, R. Wagner, R. Frahm, D. Lützenkirchen-Hecht

Fakultät 4-Physik, Bergische Universität Wuppertal, Gaußstr. 20, 42097 Wuppertal, Germany

Coatings of transition metal oxides have many applications in various technological fields, in particular Cobalt-oxides are of huge interest for solar energy conversion [1] and Li-ion batteries [2] due to their interesting physico-chemical properties. Due to the manifold opportunities to decisively influence the growth and the resulting properties of Co-oxide films, e.g. by changing the concentrations of all the anions and cations with the solution, its pH as well as the temperature of the deposition and the use of additives, electrodeposition has gained increasing attention for the preparation of metal oxide coatings in the past. For example, Brownson and Lévy-Clément has systematically changed the temperature of the substrate and the solution during deposition from Co-nitrate solutions, identifying an increased oxygen deficiency within the brucite lattice with decreasing temperature [3]. Hallaj and coworkers studied the variation of the samples morphology when the pH and the potential of the deposition was changed [4], and Rahimi et al. prepared a graphene-oxide Co-hydroxide (nano-) compound material for application in a supercapacitor [5].

In this contribution, we will consider the electrodeposition of Co-hydroxide on Gold-coated Kapton foils, employing different additives in the solution and studying the resulting film properties (structure, thickness, morphology) using a combination of electrochemical methods, ex-situ scanning electron microscopy (SEM) and EXAFS experiments at DELTA beamline 10 [6]. Co-hydroxide deposition took place in a standard three-electrode compartment with a gold-coated Kapton foil as a working electrode, a platinum plate as a counter electrode and an Ag/AgCl reference electrode ($E^0_h = 0.210$ V), against which all potentials are reported. The working electrodes were prepared by DC-sputtering in an Ar-atmosphere for typically 5 minutes, resulting in a gold film of about 200 nm thickness. Electrochemistry was performed in 0.1 M $\text{Co}(\text{NO}_3)_2$ solutions with different additives such as ethylenediaminetetraacetic acid ($\text{C}_{10}\text{H}_{16}\text{N}_2\text{O}_8$, EDTA), polyethylene glycol ($\text{C}_{2n}\text{H}_{4n}\text{O}_n$, PEG) and dodecyltrimethylammoniumbromide ($\text{C}_{15}\text{H}_{34}\text{BrN}$, DTAB) in 0.25 - 30 mM concentration. The samples were deposited at -1.1 V and usually for 5 minutes of deposition. After preparation, they were removed from the electrolyte, carefully rinsed with distilled water and dried using air. Ex-situ SEM investigations were performed using a JEOL JESM 6510 system. EXAFS experiments were performed at DELTA beamline 10 using a Si(111) channelcut monochromator [6], a N_2 -filled ionization chamber for the incident and Ar-filled ionization chamber for the transmitted X-ray intensities. A third ionization chamber was used to monitor a Co metal reference sample simultaneously with the actual samples under investigation. Some of the samples were heat-treated in air for different temperatures to study the conversion from a Co-hydroxide to a Co-oxide subsequently.

In Fig. 1, the cyclic voltammograms of several 0.1 M $\text{Co}(\text{NO}_3)_2$ solutions with different concentrations of additives are presented. As can be seen, even a 30 mM concentration of DTAB is not causing a substantial increase of the current density during deposition, thus enhanced and improved deposition cannot be realized using DTAB. In contrast, using 10 mM PEG, a substantial increase of the cathodic current density is observed, and an even larger current is measured for only 2mM EDTA.

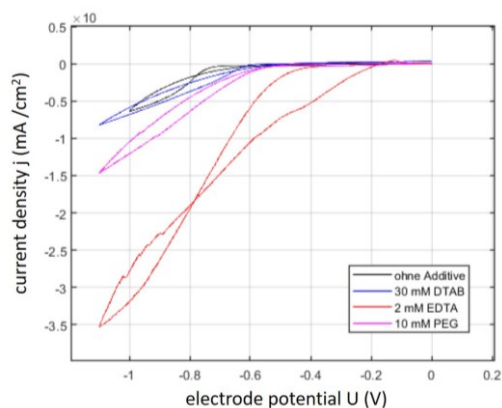


Fig. 1: Cyclic voltammetry (20 mV/s) of a pure 0.1 M $\text{Co}(\text{NO}_3)_2$ solution (—) in comparison to solutions with different additives as indicated: (—) 30 mM DTAB, (—) 10 mM PEG and (—) 2 mM EDTA.

However, inspection of the deposits revealed that no deposition has occurred in the EDTA solution, while for DTB and PEG, blue-green deposits typical for Co-hydroxides are visible (see e.g. [7]), a representative SEM-micrograph revealing the microstructure of the Co(OH)_2 -deposits is shown in the inset of Fig. 2. The Co-hydroxide deposits employing DTAB as additive reveal an improved adhesion on the gold-coated substrate, however, according to an EDX-analysis, are always accompanied by Br-incorporation within the films. Thus the deposits obtained from PEG containing solutions are investigated more closely with X-ray absorption experiments. In Fig. 2, a typical EXAFS spectrum measured at the Co K-edge (7709 eV) is shown. From the exact position of the edge, a Co^{2+} valence can be directly extracted, and the EXAFS closely resembles those of Co(OH)_2 (see e.g. [8]). Accordingly, the measured spectrum was fitted with a linear combination of EXAFS spectra of Co(OH)_2 and $\text{Co(NO}_3)_2$. As can be seen, the fit quality appears acceptable, providing a composition of $95.5 \pm 0.3 \%$ Co(OH)_2 and only $4.5 \pm 0.3 \%$ $\text{Co(NO}_3)_2$. It should be noted that similar results were also obtained if a linear combination fit was performed using the k^3 -weighted EXAFS fine structures $\chi(k) \cdot k^3$, with a slight decrease of Co(OH)_2 and an increase of $\text{Co(NO}_3)_2$ contributions, respectively [9]. Thus, the short range order structure of the nanostructured films appears to be quite similar to that of the polycrystalline brucite Co(OH)_2 reference material. Furthermore, the films seem to be almost free of contaminating species. Additional studies are related to in-situ EXAFS studies of the heat treatment [9], and will be subject of future publications.

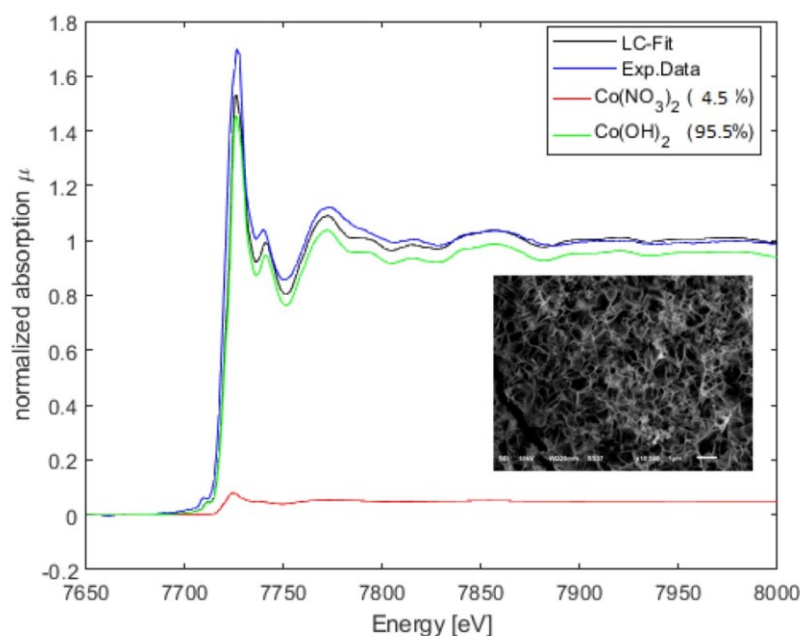


Fig. 2: EXAFS linear combination fit of a Co-material deposited in 0.1 M $\text{Co(NO}_3)_2$ solution with 20 mM PEG additive (exp. Data: —) employing $95.5 \pm 0.3 \%$ Co(OH)_2 (brucite, —) and $4.5 \pm 0.3 \%$ $\text{Co(NO}_3)_2$ (—) in comparison to the sum curve (—). In the insert, a representative SEM micrograph is shown.

Acknowledgement

We gratefully acknowledge the DELTA machine group for providing synchrotron radiation reliably.

References

- [1] E. Barrera, I. Gonzales, T. Viveros, *Solar Energy Mat. Solar Cells* 51 (1998) 69.
- [2] J.J. Auburn, Y.L. Barberio, *J. Electrochem. Soc.* 134 (1987) 638.
- [3] J.R.S. Brownson & C. Lévy-Clément, *Phys. Stat. Sol. B* 245 (2008) 1785.
- [4] R. Hallaj, et al., *Applied Surface Science* 276 (2013) 512.
- [5] S.A. Rahimi, et al., *RSC Adv.* 8 (2018) 26818.
- [6] D. Lützenkirchen-Hecht, et al., *J. Synchrotron Radiat.* 21 (2014) 819.
- [7] D. Hamulic & D. Lützenkirchen-Hecht, *DELTA annual report* (2015) 83.
- [8] D. Hamulic, I. Milosev & D. Lützenkirchen-Hecht, *Thin Solid Films* 667 (2018) 11.
- [9] L. Voss, Masters thesis, Universität Wuppertal (2020).

EXAFS experiments on cobalt-doped barium aluminate

M. Vrankić^a, A. Šarić^a, S. Bosnar^b, D. Lützenkirchen-Hecht^c, R. Wagner^c

a) Ruđer Bošković Institute, Division of Materials Physics, Bijenička 54, 10000 Zagreb, Croatia.

b) Ruđer Bošković Institute, Division of Materials Chemistry, Bijenička 54, 10000 Zagreb, Croatia

c) Bergische Universität Wuppertal – Fakultät für Mathematik und Naturwissenschaften, Gauß-Str. 20, 42097 Wuppertal, Germany.

Barium aluminate BaAl_2O_4 is an interesting host material for doping with foreign cations such as Ce, Cr, and Eu [1-6] and exhibits luminescent properties suited for applications in e.g. optoelectronic devices. At room temperature, pure BaAl_2O_4 features a hexagonal structure (space group $P6_3$), with two structurally inequivalent Ba^{2+} -sites and four different Al^{3+} -sites [7, 8]. While the Ba^{2+} are 9-fold coordinated with oxygen ions in a broad range of bond distances from 2.69-3.00 Å, the four non-equivalent Al^{3+} are 4-fold coordinated with Al–O distances spread in the range from 1.71 Å to 1.83 Å. Following up our EXAFS and XANES experiments on Eu- and Cr-doped BaAl_2O_4 , which indicate doping of the two ions result in tetrahedrally coordinated Cr^{3+} [5] and a substitution of the larger Eu^{3+} ion on regular Ba^{2+} lattice sites [6], respectively, we have recently started to investigate Co-doped BaAl_2O_4 by XANES experiments [9]. In this context, it appears interesting to identify the positions and the chemical valence of Co within the host lattice. According to our preliminary XANES results, doping results in the formation of Co^{3+} -ions [9], which may find various regular as well as interstitial sites in the host due to their small ionic radius of 60 pm only [10]. Here we present the first results of an EXAFS data analysis to get a deeper insight into the structure of the Co-doped BaAl_2O_4 material.

The Co-doped BaAl_2O_4 powder samples were prepared by a hydrothermal method and subsequent annealing in air at 1100 °C for 4 h. The Co K-edge (7709 eV) EXAFS experiments were performed at DELTA beamline 10, employing a Si(111) channel-cut monochromator [11]. An Ar-filled ionization chamber was used for the intensity measurement of the beam transmitted through the sample (I_2), a nitrogen-gas-filled ionization chamber measures the incident intensity (I_1), and the absorption was calculated as $\ln(I_1 / I_2)$. In order to reduce the noise and statistical errors, several scans each of typically 1 h acquisition time were measured and subsequently averaged. The magnitude of the Fourier-transform of the k^3 -weighted EXAFS data $\chi(k)*k^3$ obtained for the Ba-aluminate sample doped with ca. 1.6 at% Co is presented in Fig. 1. As can be seen, the $|\text{FT}(\chi(k)*k^3)|$ features a prominent peak at ~ 1.5 Å (uncorrected) radial distance, that can be related to Co–O bonds lengths, and a second distinct peak at ~ 3.0 Å distance, which probably originates from Co–Ba interactions. To get a first access to the structure of the Co-doped BaAl_2O_4 , the peak belonging to the first Co–O bond was isolated employing a filter function, transformed back into k -space, and fitted with simple Co–O coordination using phases and amplitude functions calculated by FEFF [12] and making use of the Artemis software package [13].

On a first guess, only the first peak belonging to the Co–O bonds was separated using a filter function and fitted to Co–O coordination. The fit results suggest 4 nearest neighbors at a distance of 1.92 ± 0.02 Å. The obtained disorder parameter (mean square relative displacement σ^2) is rather small, with a value of 0.00153 ± 0.0005 Å². The values for the inner potential shift (ΔE_0) and the amplitude reduction factor (S_0^2) are well in an accordance with the values obtained from the reference measurements for the CoO and Co₂O₃. According to the XANES measurements, Co is incorporated in the BaAl_2O_4 host lattice in the form of Co^{3+}

ions [9]. Such a conclusion coincides well with the values of the respective Co–O bond distances obtained for the Co-doped BaAl₂O₄ sample in comparison to CoO (six nearest oxygen neighbors in a distance $R_1 = 2.12 \pm 0.01 \text{ \AA}$) and Co₂O₃ (six nearest neighbors with $R_1 = 1.92 \pm 0.01 \text{ \AA}$) - i.e. the larger positive charge of the Co³⁺ leads to a shortening of the Co–O bond length, with a similar value compared to the Co³⁺-doped BaAl₂O₄. Therefore, it is rather likely that the Co³⁺ dopant (with its small ionic radius) is located on an Al-site of the BaAl₂O₄ host lattice, instead of a regular Ba²⁺-site, with much more oxygen nearest neighbors and substantially larger cation-oxygen bond distances of more than 2.69 Å. Due to the complexity of the BaAl₂O₄-structure containing four different Al-sites (Al1 – Al4), a much more detailed analysis is required to identify the exact position of Co³⁺ within the host. However, as the coordination environments of Al1–Al4 are quite different, in particular in terms of the bond distances towards Ba²⁺ with expected strong contributions in the EXAFS, it can be expected that such an analysis might however be successful, and thus, future work will deal with this challenges.

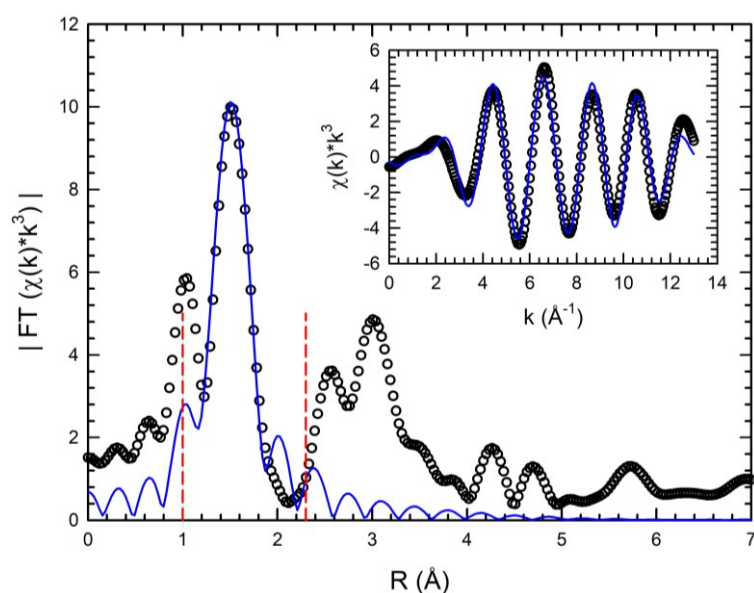


Fig. 1: Magnitude of the Fourier-transform of the k^3 -weighted Co K-edge EXAFS fine structures $\chi(k)*k^3$ for BaAl₂O₄ doped with 1.6 at.% Co. The experimental data (o) related to the first shell were fitted using single Co-O coordination. The inset displays the $\chi(k)*k^3$ for both experimental data and the fit, suggesting 4-coordinated Co in a distance of 1.92 Å (k -range for the FT: $3 \text{ \AA}^{-1} \leq k \leq 12 \text{ \AA}^{-1}$, R -range for the fit (red, vertical dashed lines): $1.0 \text{ \AA} \leq R \leq 2.3 \text{ \AA}$).

References

- [1] Z. Lou, J. Hao, M. Cocivera, J. Phys. D: Appl. Phys. **35** (2002) 2841.
- [2] V. Singh, V. Natarajan, J.-J. Zhu, Opt. Mater. **29** (2007) 1447.
- [3] T. Nakamura, K. Kaiya, N. Takahashi, et al., Phys. Chem. Chem. Phys. **1** (1999) 4011.
- [4] M. Peng, G. Hong, J. Lumin. **127** (2007) 735.
- [5] M. Vrankić, B. Gržeta, D. Lützenkirchen-Hecht, et al., Inorg. Chem. **54** (2015) 11127.
- [6] B. Gržeta, D. Lützenkirchen-Hecht, M. Vrankić, et al., Inorg. Chem. **57** (2018) 1744.
- [7] W. Hörkner, H.K. Müller-Buschbaum. Z. Anorg. Allg. Chem. **451** (1979) 40.
- [8] S.-Y. Huang, R. von der Mühl, J. Ravez, et al., J. Solid State Chem. **109** (1994) 97.
- [9] M. Vrankić, A. Šarić, S. Bosnar, et al., DELTA annual report (2019), p. 89.
- [10] <http://www.wiredchemist.com/chemistry/data/metallic-radii>
- [11] D. Lützenkirchen-Hecht, R. Wagner, S. Szillat, et al., J. Synchrotron Rad. **21** (2014) 819.
- [12] S.I. Zabinsky, J.J. Rehr, A. Ankudinov, et al., Phys. Rev. B **52** (1995) 2995.
- [13] B. Ravel, M. Newville, Phys. Scr. **115** (2005) 1007.

Notes

Notes